# InSAR Coherence Estimation and Applications to Earth Observation

JIANG MI

Ph.D

The Hong Kong Polytechnic University

2014

The Hong Kong Polytechnic University

Department of Land Surveying & Geo-Informatics

# InSAR Coherence Estimation and Applications to Earth Observation

JIANG MI

A thesis submitted in partial fulfillment of the requirements

for the degree of Doctor of Philosophy

January 2014

# Certificate of Originality

I hereby declare that this thesis is my own work and that, to the best of my knowledge and belief, it reproduces no material previously published or written, nor material that has been accepted for the award of any other degree or diploma, except where due acknowledgement has been made in the text.

_____(Signed)

___JIANG Mi_____(Name of student)

To the memory of my grandparents

# Abstract

Coherence of radar echoes is a fundamental observable in interferometric SAR (InSAR) measurements. It provides a quantitative measure of the scattering properties of imaged surfaces and therefore is widely used to study the physical processes of the earth. However, the estimated coherence is often biased due to the radar signal non-stationarity and the bias in the estimators used. Great efforts have been made over the past two decades to mitigate the errors in coherence estimation. Radar signal non-stationarity has been dealt with either by compensating for the systematic interferometric phase in the estimation window or by selecting and using the homogeneous pixels to avoid the texture effect in SAR images. The bias of the estimators has been corrected by the probability model deduced under Gaussian scene.

Although the existing studies have improved the accuracy of coherence estimation with different levels of success, some key problems still remain. For example, it is difficult to avoid the overestimation of the coherence over noise only areas due to the overcorrection of the fringe pattern if no fringe pattern exists. It is also unclear how to mitigate the bias of the sample coherence when the sample size is small. In addition to the technical limitations, the assumptions behind these methods, such as the Gaussian property and the independence between the neighboring sample coherence, are often too rigorous to hold over many natural scenes, leading to mis-estimation of the coherence in the real world. The purpose of this thesis is to gain a better understanding of the sources of errors in InSAR coherence estimation, and to develop self-adaptive algorithms with fewer assumptions to solve the problems aforementioned.

We begin by briefly reviewing the existing techniques for coherence estimation. Three principal errors (i.e., errors due to biased estimators, appearances of image textures and fringe rates in estimate windows) are quantitatively analyzed

by means of mathematic descriptions.

Under the framework of multi-temporal InSAR (MT-InSAR) with moderate to large stack size, we propose a hybrid processing chain to mitigate three types of errors. To avoid overestimation of coherence induced by image texture, an adaptive two-sample distribution-free test is developed to compare the statistical homogeneity between two spatial pixels by using their temporal samples. To avoid underestimation or overestimation of coherence induced by local fringe rates, we suggest using the phase standard deviation map to guide the Fourier kernel adaptively. A newly developed estimator of bias correction, namely double bootstrapping, is deduced under assumption-free condition. The method is especially effective for small sample problem in which the biased coherence cannot be corrected by the existing estimators.

Based on the foregoing processing chain, further progress has been successfully made for small SAR stacks. Statistically homogeneous neighbors for each central pixel are selected by using their spatio-temporal samples, rather than temporal samples only. Furthermore, considering the computational complexity of double bootstrapping, a Jackknife-based method is proposed for bias mitigation in coherence estimation. We present experimental results with both simulated and real data sets, and compare the performance of the proposed approaches against some of the existing ones. The results demonstrate that the new approaches can suppress the errors more effectively under various circumstances.

Finally, by associating a decorrelation model with the new processing chain, we decompose coherence observations and extract the temporal components of decorrelation from a texture-significant area in Macau, and find that the time series of coherence are less noisy and biased than those obtained from conventional methods in almost all land covers. The results confirm that the methods presented in the thesis can improve the accuracy of InSAR coherence-based applications to earth observations.

# Acknowledgements

Although only the author's name is on the cover of this thesis, there are many people contributing to it as well. I would like to thank all those who helped and provided me with the possibility of completing this thesis, which made my PhD study a wonderful experience.

First and foremost, I would like to express my deepest gratitude to my supervisor, Prof. Xiaoli Ding, a devoted scientist and a gentleman. I had the good fortune to have a supervisor who provided me with an opportunity to pursue my dream at The Hong Kong Polytechnic University (PolyU), and gave me free rein to explore my research. His patience and constant guidance helped me go through many important stages, and in the end finalize the thesis. I hope one day I will become as good a supervisor as Prof. Ding.

I would also like to express my greatest thanks to Prof. Zhiwei Li, my former supervisor at Central South University, for inspiring my interest in the field of InSAR six years ago. His stimulating suggestions and persistent encouragement spice up my research life. I am also grateful to the radar group of Central South University. My time with the group played a crucial role in what I have achieved to date.

I owe my thanks to all colleagues of the radar group in Delft University of Technology (TU-Delft), the Netherlands. I would like to particularly thank Prof. Ramon Hanssen for being my supervisor in TU-Delft and sharing his vast knowledge, expertise and experience during my stay as a guest PhD student. I also appreciate the guidance by Dr. Andy Hooper, who helped me gain valuable knowledge of InSAR. Other colleagues who made my time at TU-Delft enjoyable are Ling Chang, Yu Morishita, Freek van Leijen, Sami Samiei Esfahany, Anneleen Oyen and Joana Esteves Martins.

My special gratitude goes to Prof. Fabio Rocca and Dr. Teng Wang at Politecnico di Milano and Dr. Ridha Touzi at Canada Centre for Remote Sensing for their expert criticisms and continuous comments on the InSAR study throughout my PhD program.

There are so many people at PolyU who I would like to thank individually for their friendship. Guangcai Feng, Linguo Yuan and Lei Zhang provided me with spades of interesting suggestions and offered great help to my study. I sincerely thank my smart and hardworking groupmates, Jianchao Wei, Chisheng Wang, Wu Zhu, Linghong Ke, Bocheng Zhang, Wonjin Lee, Jun Hu, Wentao Yang, Qian Sun, Wenkun Yu, Bing Xu and Jia Li, from whom I learned a lot during my stay in PolyU.

I deeply appreciate the financial support from the Research Student Attachment Programme 2011/12 and the PhD scholarship of PolyU, which made this research possible.

Finally, I dedicate this thesis to my family for their constant love, concern, and endless support.

# Contents

# List of Tables

# List of Figures

Chapter 1

# Introduction

## 1.1 History

Space-borne synthetic aperture radar interferometry (InSAR) has been widely applied in the past three decades to various branches of geoscience [e.g., *Bamler and Hartl*, 1998; *Massonnet and Feigl*, 1998; *Rosen et al.*, 2000]. The technique exploits the phase difference of two or more complex SAR images acquired from satellite orbits with slightly different viewing geometries and repeat periods. The derived information allows the assessment of many geophysical events, such as earthquakes [*Feng et al.*, 2010; *Fialko et al.*, 2005], volcano eruptions [*Hooper*, 2012], land subsidence [*Ding et al.*, 2004; *Ferretti et al.*, 2001; *Zhang et al.*, 2012], and glaciers dynamics [*Joughin et al.*, 2004].

Though tremendous success in previous studies has shown how interferometric phase observation leads to a greater understanding of geophysical monitoring of natural hazards, InSAR phase measurement, however, is still limited to illuminated areas with high deformation gradients and/or fast decorrelation [*Jiang et al.*, 2009; 2011; *Massonnet and Feigl*, 1998; *Tian and Liao*, 2013]. The limitations have been highlighted with a number of large subduction earthquakes and vegetated terrains [*Feng et al.*, 2012; *Fielding et al.*, 2005; *Wei and Sandwell*, 2010; *Yun et al.*, 2007]. Furthermore, some surface characteristics, such as geometric structure, roughness, and dielectric properties, are not likely to be interpreted using the interferometric phase since it only carries information about topography, deformation as well as other phase signal delays induced by the atmosphere [*Hanssen*, 2001; *Jung et al*, 2013; *Li et al.*, 2012; *Pepe et al.*, 2011]. It therefore remains unclear whether InSAR systems can provide additional information about a certain studied area when the returned phase is infeasible.

There is another InSAR observable, namely interferometric coherence. The coherence, or correlation of an interferogram, measures the degree to which the complex phase signals of the two SAR images is coherent in the same position [*Touzi et al.*, 1999]. Since coherence is determined by phases and two image intensities related to radar backscattering (see the definition of coherence in Chapter 2.1.1), it is sensitive to imaging geometry (e.g. incidence angle, perpendicular baseline), surface properties (e.g. correlation length of surface, extent of scatterers) and the changes in the scattering medium between two image acquisitions [*Oveisgharan and Zebker*, 2007; *Zebker and Villasenor*, 1992]. According to the decorrelation model in which the total coherence is the product of individual decorrelation [*Hoen*, 2002; *Oveisgharan and Zebker*, 2007; *Zebker and Villasenor*, 1992], we can infer physical parameters under the assumption that the source of decorrelation related to these parameters dominates the loss of total coherence and other components can be thoroughly removed. This becomes the basic rationale of InSAR coherence based application. In addition to its applications to Earth observation, the coherence is a measure of relative contribution of phase noise to the total interferometric phase. The coherence has been used historically to evaluate the accuracy of phase estimates [*Bamler and Hartl*, 1998; *Hoen*, 2002].

The following paragraphs reviewing the application of coherence can be categorized as follows: (i) coherence as an indicator for InSAR data processes and (ii) application to Earth observation.

### 1.1.1 Coherence in InSAR Data Processing

*1. Phase filtering*

As stated in Eq. (41) [*Bamler and Hartl*, 1998], coherence can be recognized as a direct measure of interferometric phase noise. Therefore, it can be used to guide data processing adaptively to avoid error propagations. Modified Goldstein

filtering firstly confirms the usefulness of the assistance of coherence [*Baran et al.*, 2003]. By substituting empirical filter parameters with coherence values, the modified algorithm adapts the Goldstein filter by preventing areas of high coherence (less noise) being over-filtered, and in the meanwhile allows stronger filtering in areas where there is low coherence (strong noise). Further improvement has been made to the filter by [*Li et al.*, 2008a], where coherence and the number of looks are considered since the phase noise is a function of both of the parameters.

*2. Phase unwrapping*

Due to phase discontinuities induced by interferometric noise, mis-estimation of phase difference between two neighboring data points is deemed likely, leading to errors in unambiguous phase values [*Hooper and Zebker*, 2007]. Coherence is therefore suggested for masking the position of phase discontinuities and avoiding error propagations of integration of phase difference. Coherence has been widely applied to many unwrapping algorithms, including branch-cut, Minimum Cost Flow and three dimensional (3D) unwrapping algorithms [*Chen and Zebker*, 2002; *Goldstein et al.*, 1988; *Hooper and Zebker*, 2007].

*3. Time series analysis*

Another successful application of coherence is to select coherent pixels for time series analysis, such as Persistent Scatterers (PS) InSAR and Small Baseline Subset (SBAS) InSAR. Coherence is no longer an indicator but a criterion for identifying stable points that are highly correlated temporally. *Berardino et al.* [2002] suggested using mean coherence maps of data stacks to select PS candidates. The method has been used in some other many multi-temporal InSAR techniques [*Goel and Adam*, 2012; *Mora et al.*, 2003; *Perissin and Wang*, 2012]. Considering that the temporal coherence mean is not sensitive to partially incoherent pixels, an alternative is to select points from those presenting a good

coherence level in all coherence maps [*Zhang et al.*, 2012].

### 1.1.2 Application of InSAR Coherence to Earth Observation

*1. Land cover classification*

Coherence application to land cover classification is based on the following principle: water bodies show very low coherence, forest areas show low coherence, bare land and agricultural fields show moderate to high coherence, and rocks and artificial buildings in urban areas show very high coherence. Since coherence is usually affected by temporal decorrelation, SAR backscatter images are regarded as a complementary observable. *Wegmuller and Werner* used an ERS pair with a three-day repeat period to classify vegetated areas [*Wegmuller and Werner*, 1997; *Wegmuller and Werner*, 1995]. In their method, the color coding scheme combining backscatter information, backscatter variability and coherence was introduced and 91% accuracy was reported for forest/nonforest mapping. Strozzi et al. used several methods for Tandem pairs and achieved classification 75% accuracies for four land covers [*Strozzi et al.*, 2000]. More advanced methods use various temporal characteristics of different land covers. *Dammert et al*. proposed to use a series of coherence maps estimated from data stacks to map complex terrains [*Dammert et al.*, 1999]. The fuzzy C-means method was tested to segment images, and 65% to 75% overall accuracy for five classes and 93% for water/land classification were reported respectively. Likewise, the ISODATA classifier was applied by *Engdahl et al*. and the overall accuracy for six classes was 90% [*Engdahl and Hyyppa*, 2003]. Both methods used principal components transformation to reduce SAR intensity and coherence images.

*2. Change detection*

It is important to note that because complex value in each radar resolution cell

results from the superposition of many individual radar echoes, coherence at each image pixel is sensitive to relative changes in a scale below the resolution of the instrument [*Hoffmann*, 2007], which explains why coherence observations can measure the changes in surface objects between two acquisitions. A typical application involves surface tracing of fault rupture and assessment of damage levels related to earthquakes [*Fielding et al.*, 2005; *Gamba et al.*, 2007]. *Yonezawa and Takeuchi* [2001] firstly used coherence from one-pair data for detecting urban damage in earthquake-stricken areas. A similar work was done by *Mansouri et al*. [2005], where pre- and post-coherence were compared with pre- and pre coherence map, and their dispersion was then used to identify damaged areas. More advanced methods allow precise discrimination among different damage levels by means of integration of coherence, intensity variability, SAR intensity and optical data [*Arciniegas et al.*, 2006; *Bignami et al.*, 2004; *Hoffmann*, 2007]. Note that geometric changes related to an event should dominate temporal decorrelation. Therefore, it is better for interferometric pairs with shorter time intervals to detect events, which can be earthquakes, floods, rain storms and fires [*Geudtner et al.*, 1996; *Tanase et al.*, 2010; *Wiesmann et al.*, 2001].

*3. Surface properties retrieval*

Observations of InSAR coherence in forest areas have shown a promising possibility of retrieving biophysical parameters, such as stem volume, tree height, biomass, and stem diameter [*Askne et al.*, 2003; *Askne et al.*, 1997; *Santoro et al.*, 2002; *Santoro et al.*, 2007b]. The rationale is that increasing the number of forest parameters results in decreasing coherence caused by volume temporal decorrelation. However, over forested terrain, temporal decorrelation due to the wind-induced movement of scatterers (e.g. needles, branches) near tree-tops between two acquisitions may be significant and thus tandem data are a preferred data source. Some researchers have also assessed the structural

information present in temporal decorrelation. *Askne et al*. [1997] assumed that wind-induced decorrelation is related to canopy height, whereas *Castel et al*. [2000] demonstrated the impact of wind on temporal decorrelation was more important in tall, mature forest stands. The main weakness here is that modeling parameters are so complicated that they are not suitable for parameter inversion in practical application. More recent works focus more on simple models (e.g. empirical electromagnetic modeling and semi-empirical interferometric water cloud models) and higher accuracy with 21 $m^3 / ha$ from a single pair and 10 $m^3 / ha$ from a multi-temporal combination for retrieval of stem volume from coherence measurements. In some cases, estimates have been competitive with collected data using standard methods of ground-based inventory [*Askne and Santoro*, 2009; *Santoro et al.*, 2007b].

The other successful application of surface properties inversion involves the understanding of the mass balance of a glacier, which acts as a key indicator of climatic change [*Hoen*, 2002]. Conventional InSAR power observation can provide useful information for constraining both the melt extent and the amount of ice discharge, which are basic information for estimation of a mass balance [*Munk et al.*, 2003; *Rott and Rack*, 1995]. However, what is lacking is the knowledge of the thickness of annual layers in the top few meters of firn [*Oveisgharan and Zebker*, 2007]. Coherence is shown to be a powerful tool to retrieve the vertical extent of scattering and therefore accumulation rates. Most representative works have been implemented by the group of Stanford University. *Hoen and Zebker* [2000] first used coherence observations and a simpler volume scatter model to estimate the penetration depth of Greenland firn. The layer spacing was then derived from a constraining model. Further progress was made by [*Oveisgharan and Zebker*, 2007], where a radar scattering model related to both coherence and power was presented to estimate accumulation rates and tested in a small area in the dry snow zone. They claimed that the retrieved accumulation parameters were more accurate than the existing remote sensing

methods.

## 1.2 Motivation

In the previous sections we have showed how coherence observations from spaceborne radar systems can lead to a greater understanding of the earth surface processes, and how important coherence is to InSAR data processing. What is lacking currently is a more complete description of the impact of the estimated coherence accuracy on these applications, since coherence observations are often biased for various reasons, such as radar signal non-stationarity, biased estimators and so forth. As highlighted by *Zebker and Chen* [2005], the errors from coherence observations must be removed if one is to derive the most accurate information from the coherence (for example, snow accumulation). *Werner et al.* [1996] also recognized the importance of coherence estimation in change detection studies. However in most applications, this problem is rarely considered and simple approaches for coherence estimation are often used.

In this thesis we will show that the constraint conditions in the current coherence estimation methods can be loosened, and more accurate coherence estimation can be achieved. The accuracy of the various InSAR coherence based applications can therefore be improved.

## 1.3 Research Objectives

There are two main objectives for this research. First, we will develop a new processing chain to improve the accuracy of InSAR coherence estimation. Second, we will use our method for the extraction of the temporal coherence components to study the decorrelation mechanisms over different land covers. The key questions addressed in the thesis are as follows:

1. How many sources of error affect InSAR coherence estimation? How do principal errors affect the accuracy of estimation? What is the required accuracy of the existing methods if they are to be used for mitigating the bias effects?

2. What algorithm for neighboring pixels selection can make the best use of the temporal samples? Is there any demonstrable improvement in statistical performance when the temporal samples are small?

3. Is it possible to enhance the performance of fringe rate estimation when fringe patterns are complicated? How to reduce the impact of the mis-estimation of fringe rate on coherence estimation?

4. Presently, the estimators for bias correction require a large number of independent sample coherence and probability model under Gaussian environment. Both conditions however are not likely to be satisfied in the SAR scenes. Is there any solution correcting the bias of coherence without consideration of both conditions? Is it possible to design an estimator that not only improves the accuracy of coherence estimation, but also gives more attention to the computational efficiency?

5. Is there any improvement for actual applications after accurate coherence estimation using processing chain developed in this thesis?

## 1.4 Synopsis

Chapter 2 reviews previous works on coherence estimation. We model the sources of error and analyze the influence of these errors on coherence estimation. The problems of the current methods are also highlighted.

Chapter 3 presents a hybrid approach to coherence estimation under the framework of the MT-InSAR. The method integrates different estimators with

different sources of error and gives more attention to mitigation of assumptions behind estimate procedures.

Chapter 4 develops a spatio-temporal algorithm that allows us to select statistically homogeneous pixels for each central pixel more accurately even for a small stack size. Also in the chapter is a pragmatic method for mitigating the bias in coherence observations.

Chapter 5 demonstrates the application of our methods to TerraSAR-X datasets from an area with rich texture over Macau, and the extraction of time series temporal coherence components over different land covers. The performances of the proposed methods in time series extraction are further investigated and compared with the conventional methods.

Chapter 6 gives conclusions of the thesis and suggestions for future work.

Chapter 2

# Errors in Coherence Estimation

## 2.1 Coherence Estimation

### 2.1.1 Coherence and Coherency Matrix

The coherence of two zero-mean complex Gaussian signals $s_1$ and $s_2$ is defined as [*Touzi et al.*, 1999],

$$\gamma = \frac{E\left(s_1 s_2^*\right)}{\sqrt{E\left(|s_1|^2\right)E\left(|s_2|^2\right)}} \tag{2.1}$$

where $E(\cdot)$ and * are expectation and complex conjugate operations respectively. The coherence magnitude $\rho = |\gamma|$ defines the degree of coherence. In Eq. (2.1), signals $s_1$ and $s_2$ are assumed to be stationary and $s_1 s_2^*$ is jointly stationary. Since the ensemble averages in Eq. (2.1) cannot be obtained in practice, spatial averages are often used when assuming that the signals are ergodic [*Touzi et al.*, 1999; *Zebker and Chen*, 2005]. Considering $L$ samples in an estimation window, the sample estimator $\hat{\gamma}$ of $\gamma$ is,

$$\hat{\gamma} = \frac{\sum_{i=1}^{L} s_1(i) s_2^*(i)}{\sqrt{\sum_{i=1}^{L} |s_1(i)|^2 \sum_{i=1}^{L} |s_2(i)|^2}} \tag{2.2}$$

The maximum likelihood (ML) coherence magnitude estimate is therefore $\hat{\rho} = |\gamma|$ [*Seymour and Cumming*, 1994; *Touzi et al.*, 1999], which is an asymptotically unbiased estimate.

The generalization of coherence is a coherency matrix, which is defined by *N*-variate complex signals $s_1, s_2, \mathrm{K}, s_N$. Under the Gaussian assumption, the sample covariance matrix $\hat{\Sigma}_s$ of multiple complex random variables (RVs) can be

written as follows [*Goodman*, 1963],

$$\hat{\Sigma}_s = \frac{1}{L}\sum_L ss^{*T} = \begin{bmatrix} \langle |s_1|^2 \rangle & \langle s_1 s_2^* \rangle & \mathsf{K} & \langle s_1 s_N^* \rangle \\ \langle s_2 s_1^* \rangle & \langle |s_2|^2 \rangle & \mathsf{K} & \langle s_2 s_N^* \rangle \\ \mathsf{M} & \mathsf{M} & \mathsf{O} & \mathsf{M} \\ \langle s_N s_1^* \rangle & \langle s_N s_2^* \rangle & \mathsf{K} & \langle |s_N|^2 \rangle \end{bmatrix} \tag{2.3}$$

where $s = [s_1(t), s_2(t), \mathsf{K}, s_N(t)]$, $*T$ denotes the conjugate transpose and $\langle \cdot \rangle$ is space average of $L$ samples. If we use Eq. (2.3) to model the MT-InSAR dataset, the diagonal terms of $\hat{\Sigma}_s$ are estimated intensity vector and off-diagonal terms show multi-looked interferograms, like the numerator of Eq. (2.2). The coherency matrix is then defined by normalized $|\hat{\Sigma}_s|$, in which all diagonal elements are one ( $E[|s_i|^2] = 1$ ) and off-diagonal elements are actually an estimate of the coherence magnitude $\hat{\rho}$ for all possible interferograms. Working on a coherency matrix rather than coherence is more important because pixels exhibiting different decorrelation mechanisms can provide additional insight into time series analysis. Please refer to the survey of [*De Zan et al.*, 2005] for a deeper analysis of the properties of a coherency matrix.

We will hereafter refer to $\hat{\rho}$ as coherence estimate unless $\hat{\gamma}$ is explicitly discussed.

### 2.1.2 Modeling and Analyzing Sources of Error in Coherence Estimation

Three principal errors affect accurate coherence estimation. Before the review of the current methods on errors correction, the understanding of the influence of each source of error on the final accuracy of estimation is essential.

*1. Non-stationarity of Signals $s_1$ and $s_2$*

In inhomogeneous SAR scenes, measurements in an estimate window (ESW) may have different distributions. The assumption that $E(\cdot)$ in Eq. (2.1) does not vary

within a window does not apply to such a case, resulting in biased coherence estimation. We discuss this problem in real number fields [*Jiang et al.*, 2013a]. For example, when considering two real number stationary series $s_1$ and $s_2$ having the same variances $\sigma^2$ and means $\mu$ the sizes of series $L$ are approaching infinite (i.e. $L \to \infty$). The Pearson correlation coefficient $\rho_{s_1 s_2}$ between two signals is defined as

$$\rho_{s_1 s_2} = \frac{\sum (s_1 - \overline{s}_1)(s_2 - \overline{s}_2)}{\sqrt{\sum (s_1 - \overline{s}_1)^2 \sum (s_2 - \overline{s}_2)^2}} \tag{2.4}$$

where $\overline{s}_1$ and $\overline{s}_2$ denote the sample mean of the series. When we introduce two non-stationary series $A$ and $B$ as functions of $s_1$ and $s_2$,

$$A = \begin{cases} s_1 + l_1 & s_1 < \dfrac{L}{2} \\ s_1 + l_2 & s_1 \geq \dfrac{L}{2} \end{cases} \qquad B = \begin{cases} s_2 + l_1 & s_2 < \dfrac{L}{2} \\ s_2 + l_2 & s_2 \geq \dfrac{L}{2} \end{cases} \tag{2.5}$$

where $l_1$ and $l_2$ denote the offsets. The correlation between $A$ and $B$ can be deduced as follows:

The mean $\overline{A}$ can be expressed as,

$$\begin{aligned} \overline{A} &= \frac{\sum A}{L} = \frac{1}{2}\left( \frac{2}{L} \sum_{1}^{L/2} A_i + \frac{2}{L} \sum_{L/2+1}^{L} A_i \right) \\ &= \frac{1}{2}\left( \frac{2}{L} \sum_{1}^{L/2} (s_{1i} + l_1) + \frac{2}{L} \sum_{L/2+1}^{L} (s_{1i} + l_2) \right) \\ &= \mu + \frac{l_1 + l_2}{2} \end{aligned} \tag{2.6}$$

Likewise, we get the mean $\overline{B}$ with a similar form. The mixed moment between $A$ and $B$ can be deduced as,

$$\begin{aligned}\frac{\sum AB}{L} &= \frac{1}{2}\left(\frac{2}{L}\sum_{1}^{L/2}(s_{1i}+l_1)(s_{2i}+l_1)+\frac{2}{L}\sum_{L/2+1}^{L}(s_{1i}+l_2)(s_{2i}+l_2)\right)\\ &= \frac{\sum s_1 s_2}{L}+\frac{1}{2}(l_1^2+l_2^2)+(l_1+l_2)\mu\end{aligned} \tag{2.7}$$

The mixed moment between $s_1$ and $s_2$ can be obtained by Eq. (2.4) as well as known conditions.

$$\frac{\sum s_1 s_2}{L} = \rho_{s_1 s_2}\sigma^2+\mu^2 \tag{2.8}$$

In combining Eqs.(2.6)-(2.8), the numerator of $\rho_{AB}$ is,

$$\frac{1}{L}\sum(A-\bar{A})(B-\bar{B}) = \frac{1}{L}\sum AB-\bar{A}\bar{B} = \sigma^2\rho_{s_1 s_2}+\frac{1}{4}(l_1-l_2)^2 \tag{2.9}$$

The second moment of $s_1$ can be written as,

$$\frac{1}{L}\sum {s_1}^2 = \sigma^2+\mu^2 \tag{2.10}$$

The variance of non-stationary $A$ can be deduced as,

$$\frac{1}{L}\sum A^2-(\frac{1}{L}\sum A)^2 = \frac{1}{L}\sum {s_1}^2+(l_1+l_2)\mu+\frac{1}{2}(l_1^2+l_2^2)-(\frac{1}{L}\sum s_1)^2 = \sigma^2+\frac{1}{4}(l_1-l_2)^2 \tag{2.11}$$

Likewise, we can get the variance of non-stationary $B$. Finally, associating Eq.(2.9) with the variances of $A$ and $B$, we have the correlation coefficient $\rho_{AB}$,

$$\rho_{AB} = 1+\frac{\rho_{s_1 s_2}-1}{1+k} \text{ with } k = \frac{(l_1-l_2)^2}{4\sigma^2} \tag{2.12}$$

From Eq. (2.12), it is clear that $\rho_{AB} > \rho_{s_1 s_2}$ unless $l_1 = l_2$. The bias increases with the decrease in $\rho_{s_1 s_2}$. The difference between $l_1$ and $l_2$ can be actually regarded as the difference in textures in a SAR scene, or two kinds of pixel in a window (e.g. grasses and water), which explains why the commonly used boxcar kernels are likely to indiscriminately average neighboring pixels, causing overestimation of coherence.

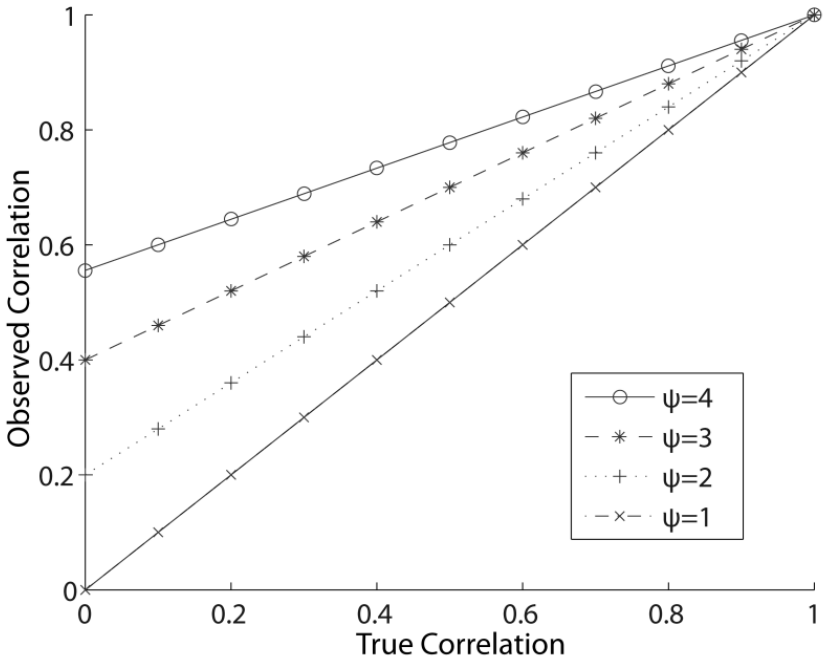


Fig. 2. 1. Overestimation of correlation when there are $\psi$ inhomogeneous distributions in ESW.

Eq. (2.12) can be further generalized by considering several offsets $l_i$, just like increased land covers in an ESW. Suppose there are $\psi$ signals with offsets $l_1, l_2, \mathrm{K}, l_\psi$, the bounds of the integral change from $[0, L/2]$ and $[L/2, L]$ to $[0, L/\psi], [L/\psi, 2L/\psi], \mathrm{K}, [(\psi-1)L/\psi, L], L \to \infty$. Then the generalization can be deduced after some simple transformations [*Jiang et al.*, 2013a],

$$\begin{aligned} \rho_{AB} &= 1 + \frac{\rho_{s_1 s_2} - 1}{1 + k} \\ k &= \frac{(\psi - 1)\sum_{i=1}^{\psi} l_i^2 - 2\sum_{i<j} l_i l_j}{\psi^2 \sigma^2} \end{aligned} \tag{2.13}$$

The bias in coherence estimation can be easily understood by its analogy to the bias problem in the correlation in Eq.(2.13) and the plot in Fig. 2.1.

*2. Non-stationarity of Signal* $s_1 s_2^*$

According to *Zebker et al.* [1992], an arbitrary image pair $s_1$ and $s_2$ can be modeled by a common part $c$, an interferometric phase $\phi$ and noise parts $n_1$ and $n_2$,

$$\begin{aligned} s_1 &= c_1 + n_1 = c + n_1 \\ s_2 &= c_2 + n_2 = c \cdot e^{-j\phi} + n_2 \end{aligned} \tag{2.14}$$

If there are several systematic phase contributions in an ESW between acquisitions, such as deformation $\phi_{defo}$, topography $\phi_{topo}$, atmosphere $\phi_{atm}$, orbit $\phi_{orb}$, the total phase can be expressed approximately as follows [*Hanssen*, 2001],

$$\phi = \phi_{defo} + \phi_{topo} + \phi_{atm} + \phi_{orb} \tag{2.15}$$

Substituting $s_1$ and $s_2$ in the numerator of Eq. (2.2) with Eq. (2.14), we have,

$$\left|\sum_{i=1}^{L} s_1(i)s_2^*(i)\right| = \left|\sum_{i=1}^{L} [c_1(i)c_2^*(i) + c_1(i)n_2^*(i) + c_2^*(i)n_1(i) + n_1(i)n_2^*(i)]\right| \tag{2.16}$$

Assume that $L \to \infty$ and the last three terms of strict independence between noise and signals are zero, Eq. (2.16) term can be deduced as,

$$\left|\sum_{i=1}^{L} s_1(i)s_2^*(i)\right| = \left|\sum_{i=1}^{L} c(i)c^*(i)e^{-j(\phi_{defo}+\phi_{topo}+\phi_{atm}+\phi_{orb})}\right| \tag{2.17}$$

It can be seen that even the topography term $\phi_{topo}$ can be compensated by an external DEM, with other components contributing to Eq. (2.17). Considering a sine wave model with frequency $f$, Eq. (2.17) can be expressed as,

$$\left|\sum_{i=1}^{L} s_1(i)s_2^*(i)\right| = \left|\sum_{i=1}^{L} c(i)c^*(i)e^{-j2\pi fi}\right| \tag{2.18}$$

According to Eq. (2.18), coherence $\hat{\rho}$ changes significantly except for $f = 0$, meaning no systematic phase in the ESW. The results of the experimental studies (Fig. 2.2) show the influence of $f$ on coherence estimation. It can be seen that the appearance of $f$ yields a larger negative effect on high coherence observations while it is insensitive to very small coherence values.

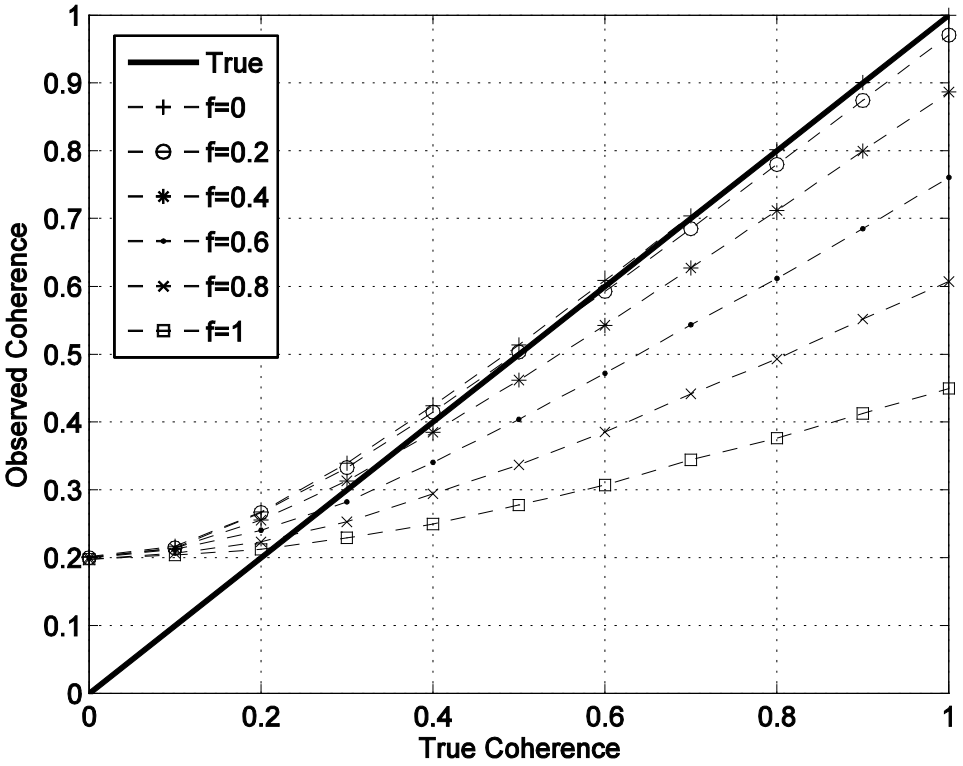


Fig. 2. 2. Underestimation of coherence under different $f$. The number of samples used for each simulation is $L = 20$.

### 3. *Bias of Estimators*

The expectation of estimator $\hat{\rho}$ can be deduced from its probability density function (PDF) [*Touzi et al.*, 1999],

$$E(\hat{\rho}) = \frac{\Gamma(L)\Gamma\left(1+\frac{1}{2}\right)}{\Gamma\left(L+\frac{1}{2}\right)} \cdot {}_3F_2\left(\frac{3}{2}, L, L; L+\frac{1}{2}, 1; \rho^2\right) \cdot \left(1-\rho^2\right)^L \tag{2.19}$$

where $F(\cdot)$ is a generalized hypergeometric function and $\Gamma(\cdot)$ is a gamma function. Due to the limited sample size of $L$, there is bias between the expectation $E(\hat{\rho})$ and the true value $\rho$. The bias is more significant for low $\rho$ and small $L$. For example, since $f = 0$, the coherence (Fig. 2.2) is significantly overestimated for $\rho < 0.4$.

### 2.1.3 Previous Works on Coherence Error Correction

The practical techniques of accurate coherence estimation have been developed in the past two decades. We review the related works according to the types of sources of error:

*1. Compensations for non-stationarity of signals* $s_1$ *and* $s_2$

The appearance of image texture in the ESW can be regarded as the main reason for signal non-stationarity. Numerous estimators have been proposed over the past decade and most of them aim to select statistically homogeneous pixel (SHP). *Lee et al*. [2003] firstly proposed to use a series of directional windows centered on a given pixel to detect an optimal window in which the local gradient is minimum, and then coherence is estimated using all the samples in the window. Compared with a boxcar window, this method preserves edge structures and mitigates pixel heterogeneity. However, choosing a suitable size for an ESW is difficult. The small size reduces the sample number and leads to higher bias towards coherence estimator $\hat{\rho}$, while the large size increases the probability of selecting inhomogeneous pixels over the area with rich textures.

The intensity-driven adaptive-neighborhood (IDAN) technique has been proposed to overcome the limitations of Lee's method. This method detects signal local stationarity using speckle statistics and allows an ESW to grow in other directions when spatial features are detected [*Vasile et al., 2004; Vasile et al., 2006; Vasile et al., 2008*]. The principle of IDAN is to construct a conditional interval for each pixel by means of local means and coefficients of variation (normalized variance), and pixels lying in the interval are selected as SHPs. Because the initial mean should be replaced by a median to avoid outliners, point-wise targets are likely to be ruled out from the estimate as long as they do not dominate the window. In addition, the region-growing procedure is easy to stop under a small look number due to strong speckle noise [*Jiang et al.*, 2013a].

Rather than restricting SHPs to a local neighborhood like a boxcar window, directional window or region grown window, the Nonlocal InSAR (NL-InSAR) technique is proposed to combine SHPs, both connected and far apart, with central pixels for coherence estimation [*Deledalle et al.*, 2011]. The method uses the concept of non-local filtering [*Deledalle et al.*, 2009] to iteratively exploit the membership of neighboring pixels according to a patch-based similarity criterion. The drawback of this estimator is the attenuation of details over structural areas.

We should point out that all the methods mentioned above are only workable for an image pair. Considering that the features of each pair may be quite different over the same scene, the SHPs selected are therefore different. This behavior limits the application of MT-InSAR and the estimate of coherency matrices as each element in Eq. (2.3) cannot be equivalently filtered in the same manner. To solve the problem, the most recent approach uses the concept of hypothesis tests based on data stacks [*Ferretti et al.*, 2011]. At each pixel, a neighboring area of variable shapes and sizes is built by comparing the similarity of empirical distribution functions (EDF) of two temporal samples. All pixels are then regarded as SHPs of a central pixel if they are not rejected by hypothesis tests. Different estimators (e.g. Kolmogorov–Smirnov (KS) test, Anderson-Darling (AD) test, and Likelihood Ratio (LR) test) have been proposed [*Goel and Adam*, 2012; *Parizzi and Brcic*, 2011].

*2. Compensations for non-stationarity of signal* $s_1 s_2^*$

The departure of the jointly stationary condition is induced by systematic phase variations mainly due to topography, but also to atmospheric disturbance and deformation gradients [*Jiang et al.*, 2011; *López-Martínez and Pottier*, 2007]. The most conventional method is to compensate for topography by means of the external Digital Elevation Model (DEM) [*Dammert et al.*, 1997]. Nevertheless, since the required accuracy of the DEM increases with the baseline length, the compensation may not be effective for local topographic variations which are

normally reflected well by the DEM.

Two different ways are used to solve the problem. One is the direct estimation of coherence without considering phase information. The most typical method refers to the Siegert estimator [*Guarnieri and Prati*, 1997; *Lee et al.*, 1994; *Rignot and Van Zyl*, 1993]. Compared with traditional estimator Eq. (2.2), the Siegert estimator works fast as no phase information needs compensating. However, the larger bias and variance of such estimator significantly limits its estimate accuracy.

The other solution is to use local frequency techniques to compensate fringe patterns before coherence estimation. *Spagnolini* [1995] studied the accurate estimation of fringe rates on wrapped phases. Recent techniques, such as the two-dimensional (2-D) fast Fourier transform (FFT) estimator, MUSIC estimator and multi-scale fringe rate estimator, achieve this goal by exploring the best local phase ramp in a window [*Trouvé et al.*, 1996; *Trouvé et al.*, 1998; *Vasile et al.*, 2008; *Zebker and Chen*, 2005]. The advantage of the FFT estimator is its high computational efficiency and considerable accuracy for estimating linear phase trends, while the two-step multi-scale estimator is more competent for retrieving complicated fringe patterns appearing in high-resolution scenes. The newly developed multi-resolution iteration algorithm improves the accuracy of fringe rate estimation in strongly noisy areas at the expense of time consuming [*Wang et al.*, 2012].

*3. Bias corrections*

Under the Gaussian assumption, the PDF and the moments of coherence estimator $\hat{\rho}$ have been deduced [*Tough et al.*, 1995; *Touzi et al.*, 1999]. It is shown that $\hat{\rho}$ is a biased estimator and its bias changes both true coherence $\rho$ and the look number $L$. *Touzi et al.* proved that an unbiased estimator, which is a function of sample coherence (see Eq. (2.19)), cannot be found from

the first moment of $\hat{\rho}$. Therefore, a general solution to bias mitigation is to average $H$ independent sample coherence $\hat{\rho}_{Li}$ in an $L$ looks coherence map to approach the expectation ( $\overline{\hat{\rho}} \approx E(\rho)$ ),

$$\overline{\hat{\rho}} = \frac{1}{H}\sum_{i=1}^{H}\rho_{Li} \tag{2.20}$$

Then unbiased $\rho$ can be approximately obtained by inverting Eq. (2.19). A less biased estimate of $\rho$ is based on the second kind statistics [*Abdelfattah and Nicolas*, 2006], namely the exponential of the log-sample coherence $\hat{\rho}_{Li}$.

$$\ln\left(\overline{\hat{\rho}}\right) = \frac{1}{H}\sum_{i=1}^{H}\ln\left(\rho_{Li}\right) \tag{2.21}$$

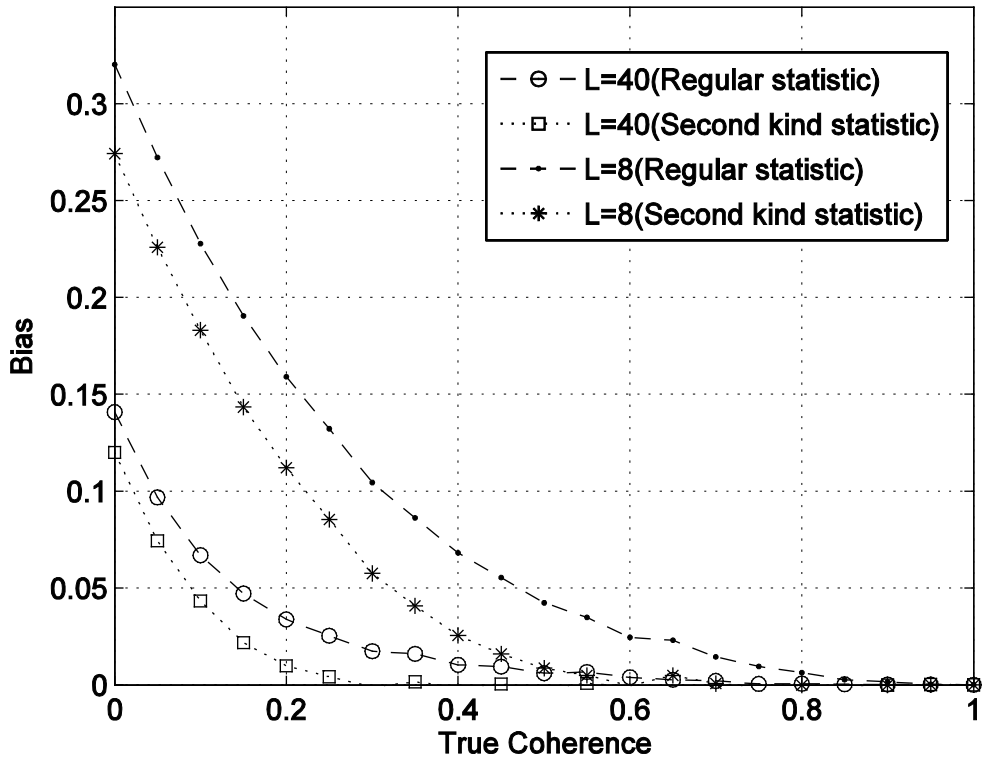


Fig. 2. 3. Coherence bias for different looks computed with regular and log-moments approaches.

It can be seen from Fig. 2.3 that the estimator of log-moment can give less bias and smaller variance than regular estimators. However, because there are no existing analytical expressions for the first and the second log-moment, only a

numerical approach, based on a Maple code, allows a graphic comparison between expectation and true coherence [*Abdelfattah and Nicolas*, 2010; *Abdelfattah and Nicolas*, 2006].

## 2.2 Shortcomings in Existing Methods for Coherence Estimation

1. Due to a lack of prior knowledge of the type of land cover (modeled by offsets in Section 2.1.2) and the number of samples in each class (the bounds of the integral in Eq. (2.13)), the model in Eq. (2.13) cannot be used directly to compensate image texture, and the reliable procedure of sample selection is therefore expected to avoid the texture effect. However, the accuracy of the current methods for SHPs selection is compromised by test power and stack size, especially for non-parametric statistics and small sample problems, which implies that heterogeneous pixels may be included in the window and lead to a loss of spatial resolution and a decrease in accuracy of estimated coherence.

2. Take into consideration both computational efficiency and accuracy, fringe rate estimation based on FFT is more feasible for actual data processing. Unfortunately, the accuracy of such an estimator is limited by the ESW, which should be small enough to ensure constant fringe frequencies and large enough to avoid dominant frequencies from pure noise. The former leads to residuals of fringes and underestimation of coherence values (Fig. 2.2), while the latter yields redundant fringes inversely added to phase terms in Eq. (2.17), resulting in overestimation of coherence values [*Zebker and Chen*, 2005].

3. Bias correction by existing estimators is difficult in practice. It can be seen from Eqs. (2.20)-(2.21),

4. $H$ non-overlapping windows, including $L$ original samples (assuming independent complex values for neighbors), are required to approach the expectation. This condition seems so rigorous that both estimators are merely workable for a very large homogeneous area. In texture significant areas where the sample is insufficient, the estimate dispersion is large and the inversion of Eq. (2.19) cannot be used [*Touzi et al.*, 1999]. In fact, coherence is still biased especially in low coherence conditions.

Moreover, Eq. (2.20) or Eq. (2.21) assumes that $\hat{\rho}_{Li}$ is stationary and ergodic in its mean. The assumption is difficult to satisfy due to the spatial variability of sample coherence induced by environmental changes. As a result, different ensembles are included in averaged pixels and the sample mean deviates from its expectation. Fig. 2.4 shows a homogeneous pasture in Delft, the Netherlands. Ergodicity in the case is untenable due to the spatial change of sample coherence.

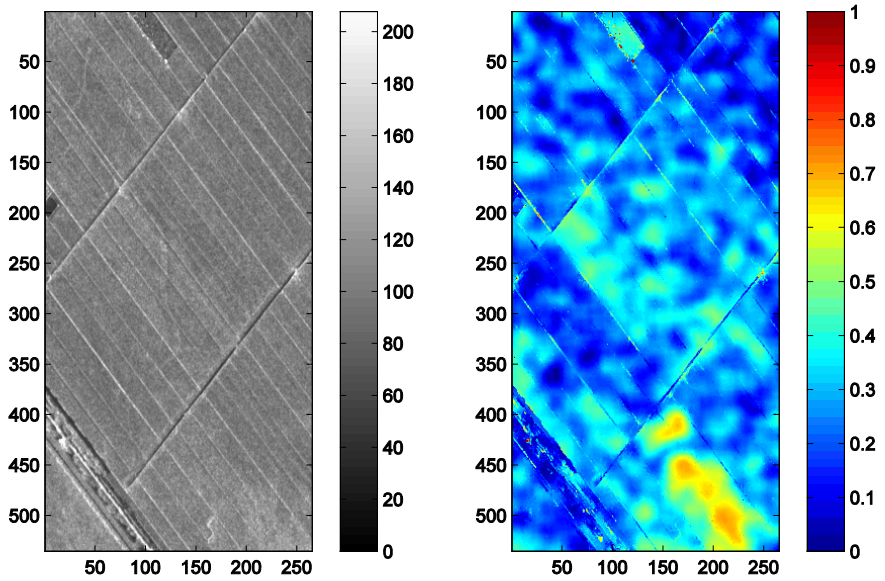


Fig. 2. 4. An incoherent amplitude averaging image over Delft area (left) and corresponding sample coherence (right) for an image pair.

Finally, the probability models designed for the current methods are derived from Gaussian scenes. However, in some circumstances (e.g. urban areas and

seas), distributions may deviate from Gaussian statistics, especially for high-resolution images where the sum of reflected waves approaches $\alpha$ -stable laws according to the generalized central limit theorem [*Kuruoglu and Zerubia*, 2004; *Ma and Nikias*, 1995]. Therefore, in such cases, the use of Eq. (2.19) may lead to undesired bias corrections.

5. Most methods are specially designed to estimate one kind of error, while the global design for mitigating all sources of error is not available. The blind integration of different methods may yield an undesired effect on final coherence values because the assumptions of each method may conflict each other.

The following two chapters are the main thrust of this research, finding out the solution to the above problems.

Chapter 3

# Hybrid Approach for Unbiased Coherence Estimation for MT-InSAR

## 3.1 Introduction

Due to the key problems discussed above, calculated coherence value for a given pixel may be higher or lower, but rarely correctly. In this chapter, we will present a hybrid approach under the framework of the MT-InSAR [*Jiang et al.*, 2013b]. The proposed processing chain integrates different estimators with respect to different error sources, resulting in reliable and self-adaptive data processing. Moreover, the algorithm gives more attentions to mitigating the assumptions and therefore works in both Gaussian and non-Gaussian scenes. Finally, the developed bias correction estimator is effective even for small sample size, and therefore can be applied widely in practice. We address the results produced by ENVISAT ASAR (ASAR) and TerraSAR-X (TSX) datasets to demonstrate the effectiveness of the approach.

## 3.2 Methodology

Let us start our method from a data stack of $N$ SAR images. Our idea, based on *adaptive two-sample hypothesis test* (ADT), is to explore data stack to select a large set of SHPs for a given pixel. To maximize test power, mixed distribution-free tests are constructed for the specified type of distribution and alternative hypothesis[1]. Considering that abnormal values will influence the test operation, the outlier detection is also included in our processing algorithm to

[1] The original discussions on "ADT" methods are shown in [*Hog,* 1974; *Hong et al.*, 1975, *Hog and Lenth*, 1984], more details under different types of alternative hypothesis are widely introduced by O'Gorman [2004]; we refer the reader to the survey of Kössler [2010] for a deeper analysis of maximizing (nonparametric) test power.

increase its robustness[2]. Based on selected SHP for each pixel and estimated phase standard deviation (STD), adaptive window is guided to optimize FFT operator. To mitigate bias pixel by pixel with less assumption, we introduce a bootstrap method[3]. The details of techniques used in the processing chain are introduced respectively in Section 3.2.1-3.2.4, and the data fusion algorithm is then given in Section 3.2.5.

### 3.2.1 Detection of Outliers in SAR Data Series

One of the most frequently used techniques for outlier detection is based on *boxplots* [*Wilcox*, 2012] as it is efficient under the assumption of data normality. However, a limitation of the *boxplot* method is that the more skewed the data are, the more observations may be detected as outliers. This is undesirable for SAR data where the data sampled temporally from a data stack are considered to have a Rayleigh or a $K$ distribution [*Parizzi and Brcic*, 2011]. Therefore, a revised boxplot method that takes into account the *medcouple* ($MC$), a robust measure of skewness for a skewed distribution, will be used [*Hubert and Vandervieren*, 2008]. Given an amplitude vector along timely stack $A_N^i = \{a_1(P_i), a_2(P_i), \mathrm{K}, a_N(P_i)\}$ of a pixel $P_i$ $P_i$, $MC$ is defined as

$$MC = \underset{a_l \le \tilde{a} \le a_j}{median}(h(a_l, a_j))$$

where $\tilde{a}$ is the sample median and $a_l, a_j \in A_N^i$, and the kernel function $h$ is given by

$$h(a_l, a_j) = \frac{(a_j - \tilde{a}) - (\tilde{a} - a_l)}{a_j - a_l}$$

[2] Throughout this Chapter we focus on the outlier detection technique combining the robust measurement of skewness and boxplot due to the fact that the SAR data is skewed. For others considering such as tailweight, please see [*Brys et al.*, 2006, *Hubert and Vandervieren*, 2008] for more details.

[3] The principle of bootstrapping for bias correction is systematically discussed in pp.124-140, Chapter 10 in [*Efron and Tibshirani*, 1993]. Advanced resampling technique for improved calculation can be found in pp. 443-501, Chapter 9 in [*Davison and Hinkley*, 1997].

For the special case that $a_l = a_j = \bar{a}$, function $h$ is defined differently (see [*Brys et al.*, 2004] for more details). Observations that fall outside the interval $[L,U]$ as defined below are considered as outliers,

$$[L,U] = \begin{cases} [Q_1 - 1.5e^{-4MC}(Q_3 - Q_1), Q_3 + 1.5e^{3MC}(Q_3 - Q_1)] & MC \geq 0 \\ [Q_1 - 1.5e^{-3MC}(Q_3 - Q_1), Q_3 + 1.5e^{4MC}(Q_3 - Q_1)] & MC < 0 \end{cases} \quad (3.1)$$

where $Q_1$ and $Q_3$ are respectively the first and the third quartiles of vector $A_N^i$.

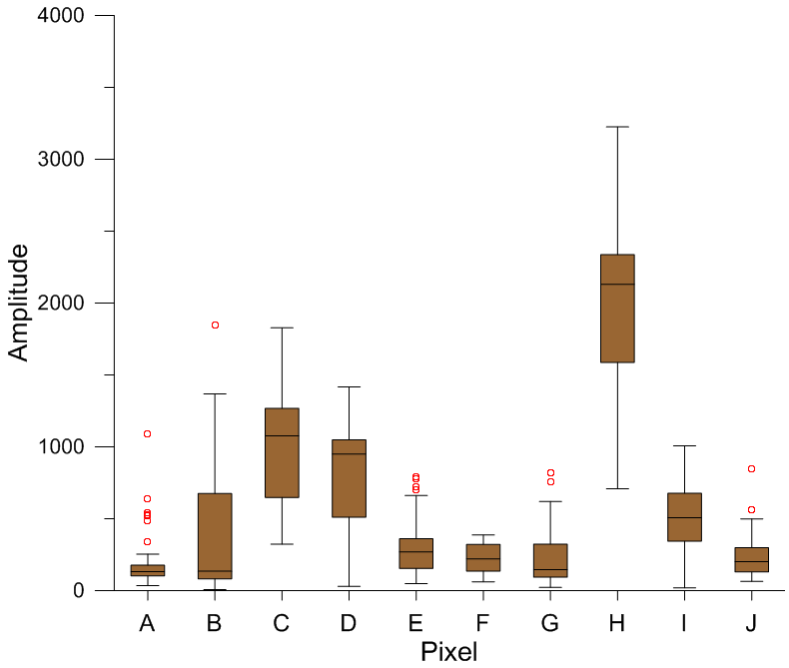


Fig. 3. 1. Adjusted boxplots of ten amplitude vectors. The red dots indicate the outliers.

Fig. 3.1 presents the adjusted boxplots of ten vectors $A_N^1, A_N^2, \mathrm{K}, A_N^{10}$ drawn from a stack of 46 ENVISAT ASAR images ($N = 46$) over Los Angeles area. The red dots are observations identified as outliers. The plots also show that the outliers impact on the distribution of the data sets. For example, pixel "A" is sampled from a light-tailed distribution. It would be dangerous to measure the tailweight without outlier removal as the dataset is heavy-tailed. The mis-estimation of the underlying distribution will strongly affect the selection of ADT later and therefore the selected SHPs. This explains why outlier detection should be carried out as part of the coherence estimation algorithm. There is the other

reason for detecting the outliers as discussed in Section 3.2.4 where some bootstrap samples may contain abnormal values due to sampling from original data with replacement.

The adjusted boxplot method is efficient and adaptive for SAR datasets. It does not need any assumption. When $MC = 0$, the data is symmetric and the adjusted boxplot becomes the standard boxplot.

### 3.2.2 Pixel Clustering: Adaptive Two-Sample Hypothesis Test

*Selector Statistics*

Adaptive two-sample tests have been proposed for increasing the power of the test when the measurements are not normally distributed [*Büning*, 2001; 2002; 2009; *Hogg*, 1974; *Hogg et al.*, 1975; *Hogg and Lenth*, 1984; *Kössler*, 2010; *O'Gorman*, 2004]. For a specific alternative hypothesis, there is no clear winner in test performance among all the non-parametric tests, and the efficiency of all the tests depends on the types of the underlying distributions. For example, for symmetric distributions with the same shape parameters, Lepage-type tests are the best [*Büning*, 2002; *Büning and Thadewald*, 2000], whereas for extremely right-skewed distributions, a modification of the KS test behaves better [*Büning*, 2001; 2002]. Therefore, an "adaptive" procedure should be applied for selecting the most suitable test for a given dataset. Following the concept of Hogg, we classify at first the type of the underlying distribution with respect to two measures, i.e., skewness and tailweight, and then select and carry out a test according to the identified distribution. We choose the skewness and tailweight measures as [*Büning*, 1994; *Büning*, 2001; 2002; *Büning and Thadewald*, 2000],

$$S(F) = \frac{F^{-1}(0.975) - F^{-1}(0.5)}{F^{-1}(0.5) - F^{-1}(0.025)} \quad \text{and} \quad T(F) = \frac{F^{-1}(0.975) - F^{-1}(0.025)}{F^{-1}(0.875) - F^{-1}(0.125)}$$

where $F^{-1}(\cdot)$ is the quantile function. Replacing the quantile function $F^{-1}(\cdot)$ by

the empirical $p$-quantile $\hat{Q}(\cdot)$, we obtain the estimates of skewness and tailweight, $\hat{S}$ and $\hat{T}$ where $\hat{Q}(\cdot)$ is defined as,

$$\hat{Q}(p)=\begin{cases} Z_{(1)} & \text{if } p \le 0.5/N' \\ (1-\varepsilon)Z_{(j)}+\varepsilon Z_{(j+1)} & 0.5/N' < p \le 1-0.5/N' \\ Z_{(N')} & p > 1-0.5/N' \end{cases}$$

where $Z_{(1)},\mathrm{K},Z_{(N')}$ are the order statistics of the combined two samples with size $N'$ and $j=\lfloor N'p+0.5 \rfloor$, $\varepsilon = N'p+0.5-j$. $p$ is cumulative probability value.

When $S>1$, the distribution function $F$ is skewed to the right; if $S=1$, $F$ is symmetric and if $S<1$, $F$ is skewed to the left. The larger the $T$ value is, the heavier the tails are. Both measures are location and scale invariant.

*Construction of ADT for SAR Stacks*

Since the signals in Eq. (2.1) are assumed to be ergodic in terms of their means, the difference in locations, i.e., difference between their expectations, of the underlying distributions should be considered. Moreover, in order to distinguish between the temporally stable points and the others, a scale that is often used to describe the variation of a temporal vector is also considered [*Ferretti et al.*, 2001]. Let $X=X_1,\mathrm{K},X_m$ and $Y=Y_1,\mathrm{K},Y_n$ be two independent samples from populations with absolutely continuous distribution functions $F$ and $G$ respectively, the hypotheses of the test is defined as $H_0: F(z)=G(z)$ for all $z\in\mathbf{R}$ versus $H_1: F(z)=G((z-\mu)/\sigma)$ with $\mu\in\mathbf{R},\sigma>0$. For $\sigma=1$, $H_1$ reduces to a pure location alternative and for $\mu=0$, $H_1$ reduces to a pure scale alternative.

There are many competing $H_1$ in terms of the location and scale alternatives. When assuming a symmetric distribution, we have the Lepage-type tests, e.g., *Wilcoxon and Ansari-Bardley* (WAB) test, *Gastwirh* (GA) test, *Van der Waerden and Klotz* (WK) test, and *Long-tail and Mood* (LM) test. For asymmetric distributions,

*Baumgartner-Weiß-Schindler* (BWS) test [*Baumgartner et al.*, 1998; *Markus Neuhäuser*, 2000], KS and *Cramer-von Mises* (CM) type tests with various weight functions are generally useful (see Appendix). To construct a new test for SAR observations, we compare all the tests mentioned above for various distributions.

For the InSAR stack (ENVISAR ASAR data stack, for example), the PDFs of 66% of the observations are found to be skewed to the right, 23% are symmetric and the remaining 11% is skewed to the left. Most data are classified as heavy- to medium-tailed. Five categories of distributions can be classified based on the results, i.e., $D_1$: right-skewed and heavy-tailed (RH), $D_2$: right-skewed and medium- to light -tailed (RML), $D_3$: symmetric and heavy-tailed (SH), $D_4$: symmetric and medium- to light -tailed (SML) and $D_5$: left-skewed (L). Furthermore, we select in total ten PDFs and use two of them for each category of the distributions (see Table 3.1). The parameters of the PDFs are adjusted to obtain the expected skewness and tailweight. The values of $S$ and $T$ thus obtained are also presented in Table 3.1.

Table 3. 1: Parameters of selected distributions and the PDFs tested

| Symmetric distributions | | | | Asymmetric distributions | | | |
|---|---|---|---|---|---|---|---|
| Density | $S$ | $T$ | Category | Density | $S$ | $T$ | Category |
| DoubleExp | 1 | 2.161 | $D3$ | Log-normal | 7.099 | 2.448 | $D1$ |
| CN* | 1 | 2.606 | | Weibull | 5.549 | 1.977 | |
| Normal | 1 | 1.704 | $D4$ | Rayleigh | 1.616 | 1.636 | $D2$ |
| Uniform | 1 | 1.267 | | Chi-square | 2.711 | 1.778 | |
| | | | | Skew-t1 | 0.146 | 2.353 | $D5$ |
| | | | | Skew-t2 | 0.345 | 1.720 | |

CN* denotes contaminated normal $0.9N(0,1)+0.1N(0,5^2)$

The appropriate statistical test for each category of the distributions is investigated using Monte Carlo simulations. The percentages of rejections of all the tests are compared and the winner is recorded. The number of simulations depends on the shift parameters, i.e., mean and variance $\mu$ and $\sigma$. Considering

that the variation of the mean $\mu$ in a sample $Y_j$ may change the variance of $Y_j$ simultaneously, we set $Y_j^* = \mu + \sigma \cdot Y_j - (\sigma - 1) \cdot E[Y_j]$ to keep them independent, where $j = 1, \mathrm{K}, k$ and $k$ is the number of Monte Carlo simulations for each shift parameter; $E[Y_j^*] = \mu + E[Y_j]$ and $D[Y_j^*] = \sigma^2 \cdot D[Y_j]$. Let $t = 0, 0.1, \mathrm{K}, 1$, $\mu(t) = t$ and $\sigma(t) = t + 1$, all possible combinations of $(\mu, \sigma)$, i.e., 121 pairs in total are obtained for each distribution and therefore 242 shift parameters for each category. Very large shift parameter $t$ is unnecessary as the shift can be easily detected in each of the tests. Simulations from small sizes $m = n = 10$ for two samples to moderate ones $m = n = 50$ have been carried out with the significance level $\alpha$ being set to 0.05 for all the tests. The test which takes the maximum of winners is then regarded as an optimal one.

Table 3. 2: Statistics of winners of test, $m = n = 25,\ \alpha = 5\%$

| Category (type) | Number of times considered as winner in power comparison | | | | | | | | | |
|---|---|---|---|---|---|---|---|---|---|---|
| | WAB | GA | WK | LM | CM1 | CM2 | CM | KS1 | KS2 | BWS |
| $D1(RH)$ | 0 | 1 | 0 | 0 | 0 | 13 | 0 | 2 | **221** | 5 |
| $D2(RML)$ | 0 | 0 | 0 | 0 | 0 | 34 | 0 | 16 | 8 | **184** |
| $D3(SH)$ | 0 | 0 | 0 | **165** | 0 | 0 | 4 | 42 | 0 | 31 |
| $D4(SML)$ | 0 | 25 | **135** | 1 | 0 | 0 | 0 | 27 | 0 | 54 |
| $D5(L)$ | 31 | **176** | 1 | 0 | 0 | 0 | 0 | 34 | 0 | 0 |

As an example, Table 3.2 shows the number of times that each of the tests considered as winner when the sample sizes $m = n = 25$. For example, it is clear that test KS2 is the best for distributions skewed to the right with heavy tails while BWS is a clear winner for medium- to light-tailed distributions. The superiorities of KS2 and BWS for the respective distributions are understandable as KS2 is constructed for distributions skewed to the right and with heavy tails and BWS is more powerful than the other tests in general. For symmetric and left-skewed distributions, Lepage-type tests are dominantly better. The results are in good agreement with other performance studies [*Büning and Thadewald*, 2000; *O'Gorman*, 2004]. Similar conclusions can be obtained for all the other

sample sizes.

Let $O=(\hat{S},\hat{T})$, the test results suggest the following ADT for SAR data stacks,

$$A(O)=\begin{cases} KS2 & \text{if } O\in D_1 := \left\{\hat{S}>1.5,\hat{T}\geq 1.9\right\} \\ BWS & \text{if } O\in D_2 := \left\{\hat{S}>1.5,\hat{T}<1.9\right\} \\ LM & \text{if } O\in D_3 := \left\{0.5<\hat{S}\leq 1.5,\hat{T}\geq 1.9\right\} \\ WK & \text{if } O\in D_4 := \left\{0.5<\hat{S}\leq 1.5,\hat{T}<1.9\right\} \\ GA & \text{if } O\in D_5 := \left\{\hat{S}\leq 0.5\right\} \end{cases} \tag{3.2}$$

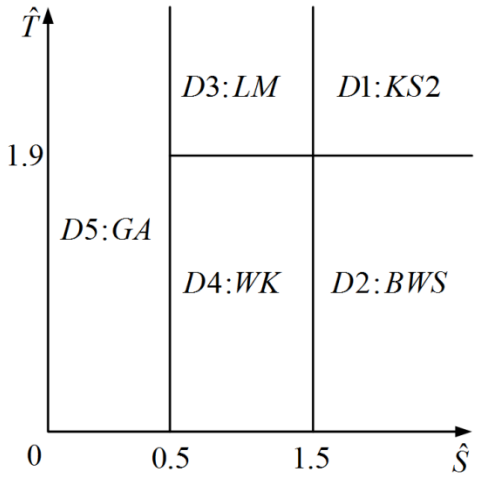


Fig. 3. 2. Schematic of adaptive test selection. The X-axis and Y-axis are the measures of skewness and tailweight respectively. For right-skewed and heavy-tailed distributions (D1), the weighted version of KS (KS2) is used; for right-skewed and medium- to light -tailed distributions (D2), Baumgartner-Weiβ-Schindler (BWS) is used; for symmetric and heavy-tailed distributions (D3), Long-tail and Mood (LM) is used; for symmetric and heavy-tailed distributions (D4), Van der Waerden and Klotz (WK) is used; Gastwirh (GA) is used for left-skewed distributions.

A schematic for test selection is also given in Fig. 3.2. It should be noted that ADT is a distribution-free test since each of the individual tests is distribution-free. When $t=0$, i.e., $\mu=0$ and $\sigma=1$, all the tests work well under significance level $\alpha=0.05$. This guarantees that ADT will have significance level $\alpha=0.05$ for every underlying continuous-type distribution.

The efficiency of the new test is evaluated in Fig. 3.3 against some commonly used tests including KS, AD and *Wilcoxon-Mann-Whitney* (WMW) test, where

gamma, normal, and skew-t distributions are used to represent the right skewed, symmetric and left skewed distributions. The sample size of the data is $m = n = 25$.

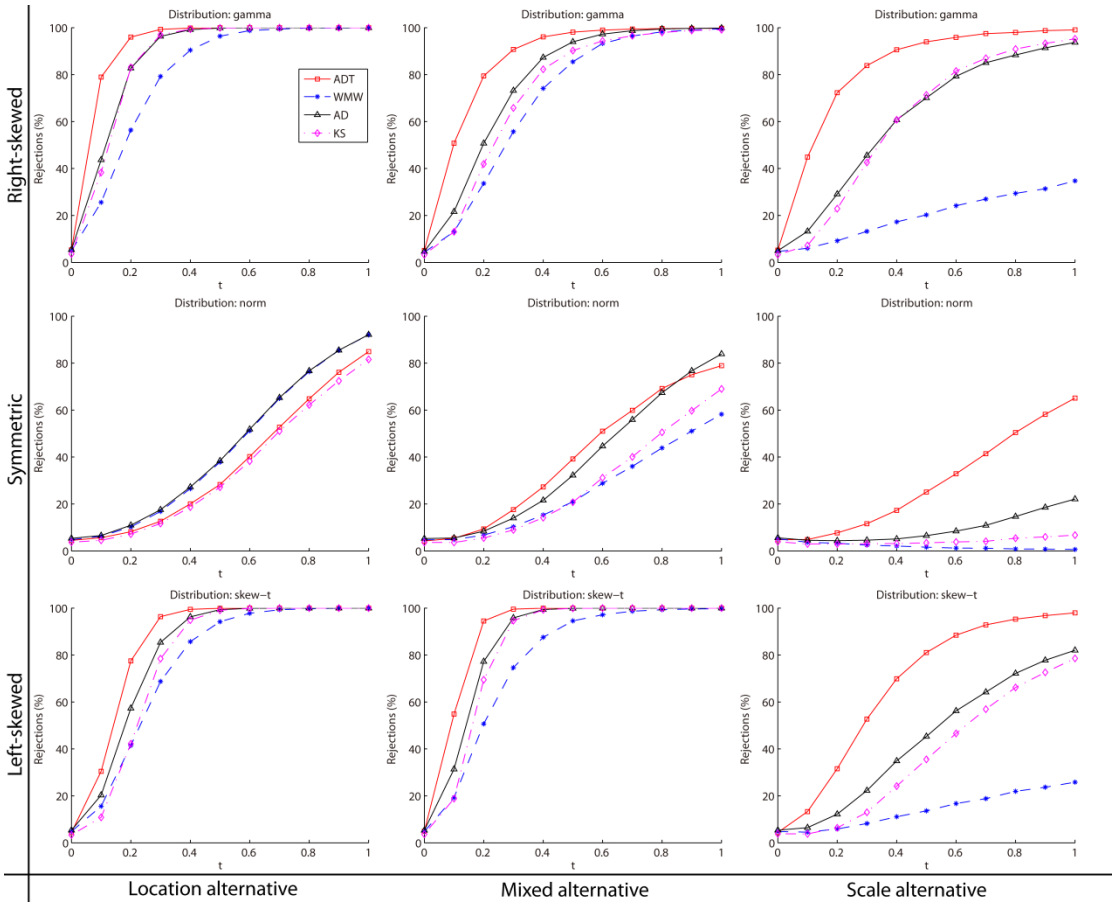


Fig. 3. 3. Power functions of different tests under different distributions determined based on simulation test results. Sample sizes $m = n = 25$, $\alpha = 5\%$.

As expected, ADT performs best except for normal distributions with location alternative where AD test behaves better. Compared with the other tests, the convergence of ADT is relatively faster for all the alternatives, mixed or single. An increase of test power results in a decrease of the level of type *II* error [*Papoulis*, 1991]. This behavior decreases the probability of averaging samples from different populations, and therefore further improves the spatial resolution and accuracy of coherence map.

### 3.2.3 Modification for ML Fringe Rate Estimation

Phase signal $s$ can be locally characterized by a 2D complex sine wave with frequency $(f_x, f_y)$ and additive noise $\phi$,

$$s(k,l) = e^{j(\phi_{\%}(k,l)+\phi(k,l))} = e^{j2\pi k f_x} \cdot e^{j2\pi l f_y} \cdot e^{j\phi(k,l)} \tag{3.3}$$

where $\phi_{\%}$ is the noise-free phase; $(k,l)$ is the pixel coordinates and $(f_x, f_y)$ shows spatial frequency. When assuming constant fringe rates within each estimation window, the local fringe frequencies can be obtained by maximizing a 2-D FFT of the signal. The peak locations in the transform correspond to the estimated fringe rates $\hat{f}_x$ and $\hat{f}_y$. Since the accuracy of the estimation of $f_x$ and $f_y$ is often affected by inconstant phase patterns and strong noise in a window, we make two modifications to reduce both effects.

A small homogeneous region within a high resolution amplitude image should correspond to a ground surface with constant slope [*Vasile et al.*, 2008]. Although this may not be true for low- to medium resolution images, the fringe rates are still likely to be more uniform in such images. Therefore, our first modification is to select an optimal Fourier boxcar for each pixel from SHPs included region. The initial box size $W_k \times W_l$ is defined according to the SHPs number for a given pixel along the range and azimuth direction respectively. Moreover, since incorrectly estimated fringe rates over a noisy area can yield overestimation of coherence values, we further change the size of the boxcar to minimize the effect of the noise with a series of sub-windows. At each pixel $(k,l)$, the mean phase standard deviation (STD) $\bar{\sigma}_{\phi}^{i}(k,l)$ is computed for each of the sub-windows $W_i$ from the phase STD map (see below). Sub-window $W_i$ is determined by defining a minimum window size $M_k, M_l$ ($3\times3$ for example), step width $R_k, R_l$ and maximum window size, i.e., $W_k, W_l$. The total number of sub-windows therefore should be

$$h = i_k \cdot i_l = \left( floor\left((W_k - M_k)/R_k\right)+1\right)\cdot\left( floor\left((W_l - M_l)/R_l\right)+1\right)$$

where $floor(\cdot)$ means rounding down operation. The window that minimizes $\bar{\sigma}_\phi^i(k,l)$ is selected as an optimal FFT boxcar,

$$w = w_i = \arg\min_{i=1,\mathrm{K},h}\left(\bar{\sigma}_\phi^i(k,l)\right)$$

To reduce the errors in the estimated fringe rates in very noisy region, a threshold $\bar{\sigma}_\phi = 1.28$ rad is used following simulations in [*Li et al.*, 2008b]. If the minimum STD $\bar{\sigma}_\phi^i(k,l)$ is larger than 1.28, the estimation procedure will be stopped to avoid overestimation of the fringe pattern. Actually, from Fig. 2.2 we can see that it is unnecessary to remove the fringe pattern for very low coherence area as the accuracy of coherence estimation is not affected significantly by the fringe pattern. To improve the computational efficiency, 2-D FFT can be substituted with repeated 1-D FFT along range and azimuth directions respectively.

The second modification aims to enhance the quality of an interferogram before it is used. Following the concept of adaptive multilooking, we adaptively average $K$ SHPs for a given pixel to improve the Signal-Noise-Ratio (SNR). The operation allows the fringe features in a scene to be followed with little loss of resolution, even in areas of low backscatting. Since the use of statistical model in [*Hanssen*, 2001] is time consuming, a simpler expression of phase STD can be defined as [*Rosen et al.*, 2000],

$$\sigma_\phi(k,l)=\frac{1}{\sqrt{2L(k,l)}}\frac{\sqrt{1-\hat{\rho}_{init}^2(k,l)}}{\hat{\rho}_{init}(k,l)} \qquad L \geq 4 \tag{3.4}$$

where $L(k,l)$ is the number of independent looks for pixel $(k,l)$. Note that the number of actual looks $K$ is greater than the number of independent looks $L$, $L \approx 0.53 \cdot K$ for the ERS1/2 [*Hoen*, 2002]. The main reason to use phase STD $\sigma_\phi$

instead of initial coherence $\hat{\rho}_{init}$ without defringing is due to the fact that SHPs number $K$ for each pixel is different, and $\sigma_{\phi}$ varies with both $\hat{\rho}_{init}$ and $L$. It is unnecessary to use Eq. (3.4) for boxcar multilooking interferograms as $L$ in Eq. (3.4) is fixed for all the pixels and it is sufficient to use $\hat{\rho}$ to quantify the difference in phase STD in each $w_i$. An application of the modified fringe rate estimation algorithm to coherence estimation is presented in Section 3.3.1 and presented in Fig. 3.7.

### 3.2.4 Bias Removal with Double Bootstrapping

Bootstrapping is a powerful technique for assessing the statistical properties of a parameter estimator such as the variance, mean and bias when the conventional techniques are not suitable or difficult to be applied for the purpose [*Davison and Hinkley*, 1997; *Efron and Tibshirani*, 1993; *Kvam and Vidakovic*, 2007; *Zoubir and Boashash*, 1998]. In the case of coherence estimation, each observation consists of a pair of complex values $x_i = (s_{1i}, s_{2i})$, $i = 1,\mathsf{K},K$ and $K$ is SHPs number for a given pixel. The observations $X = (x_1, x_2, \mathsf{K}, x_K)$ are supposed to be independent and identically distributed (i.i.d.) and are taken from an unknown bivariate distribution $F$. A bootstrap sample $X^* = (x_1^*, x_2^*, \mathsf{K}, x_K^*)$ is built by randomly sampling from the original observations $(x_1, x_2, \mathsf{K}, x_K)$ $K$ times with replacement. After obtaining a large number of i.i.d. samples $X_1^*, X_2^*, \mathsf{K}, X_R^*$, bootstrap replications $\hat{\rho}_1^*, \rho_2^*, \mathsf{K}\ \rho_R^*$ are estimated by calculating the value of $\hat{\rho}$ from each bootstrap sample. Recall that the bias of $\hat{\rho}$ as an estimate of $\rho$ is defined by $\beta = E(\hat{\rho} \mid F) - \rho$, the bootstrap estimate of the bias can then be obtained,

$$B = E\left(\hat{\rho}^* \mid F_K\right) - \rho \tag{3.5}$$

where $F_K$ is the EDF of $F$ and is determined based on the original observations $(x_1, x_2, \mathsf{K}, x_K)$. In other words, the bias $\beta$ is inferred from its simulation analogue $B$ that is obtained from the bootstrap replications

$\hat{\rho}_1^*, \rho_2^*, \ldots \rho_R^*$. Replacing the expectation in Eq. (3.5) with the average, we have

$$B_R = \frac{1}{R}\sum_{i=1}^{R}\hat{\rho}_i^* - \rho \tag{3.6}$$

According to *the law of large numbers*, $B_R$ converges to $B$ as $R \to \infty$. The study on how large $R$ should be to reach a specified accuracy has been done in [*Efron and Tibshirani*, 1993] and $R \geq 500$ is suggested.

Even if $B_R$ is large enough to have $B_R \approx B$, the bias of the original $\hat{\rho}$ may not be eliminated completely unless $B$ itself is unbiased. However, this condition cannot hold in our case. The method should be iterated to further reduce the bias. Considering the computational requirement, only one iteration, namely *Double Bootstrap* is suggested. The bootstrap estimate of the bias of $B$ can be given in terms of $c = E(B \mid F) - \beta$,

$$C = E\left(B^* \mid F_K\right) - B \tag{3.7}$$

The bias-corrected estimator $B'$ is $B' = B - C$, and the approximately unbiased estimator $\hat{\rho}'$ of sample coherence is,

$$\hat{\rho}' = \hat{\rho} - B' = \rho - B + C = \rho - 2B + E\left(B^* \mid F_K\right) \tag{3.8}$$

All terms in Eq. (3.8) are known except $E(B^* \mid F_K)$. It can be obtained by the second order bootstrap. Suppose that we have generated the $i^{th}$ bootstrap sample $X_i^*$ and the corresponding $\hat{\rho}_i^*$, then $M$ second-order bootstrap samples $X_{i1}^{**}, X_{i2}^{**}, \ldots, X_{iM}^{**}$ can be respectively obtained by sampling from $X_i^*$ $K$ times with replacement. The samples can result in estimates $\hat{\rho}_{i1}^{**}, \rho_{i2}^{**}, \ldots, \rho_{iM}^{**}$. Therefore $B_i^* \approx 1/M \sum_{j=1}^{M} \hat{\rho}_{ij}^{**} - \rho_i^*$. A good approximation of Eq. (3.8) can then be deduced as $R \to \infty$ and $M \to \infty$,

$$\begin{aligned} \hat{\rho}_{HB} &\approx \hat{\rho} - 2\cdot\left(\frac{1}{R}\sum_{i=1}^{R}\hat{\rho}_i^* - \rho\right) + \frac{1}{R}\sum_{i=1}^{R}B_i^* \\ &= 3\hat{\rho} - \frac{3}{R}\sum_{i=1}^{R}\rho_i^* + \frac{1}{RM}\sum_{i=1}^{R}\sum_{l=1}^{M}\rho_{ij}^{**} \end{aligned} \tag{3.9}$$

It can be seen from Eq. (3.9) that $\hat{\rho}_{HB}$ is evaluated completely in terms of the original sample $X = (x_1, x_2, \mathrm{K}, x_K)$ of a pixel and its replications. Knowledge on Eq. (2.19) and the distribution of $X$ is not required.

The performance of estimator $\hat{\rho}_{HB}$ against current estimators is investigated with Monte Carlo simulations where the original samples $\hat{\rho}$ are simulated according to the definition in Eq. (2.4). Let $s$, $n_1$ and $n_2$ be independent zero-mean complex Gaussian variables with the same variances. The interferometric pair with specified coherence $\rho$ is modeled by

$$\begin{aligned} s_1 &= s\cdot\sqrt{\rho} + n_1\cdot\sqrt{1-\rho} \\ s_2 &= s\cdot\sqrt{\rho} + n_2\cdot\sqrt{1-\rho} \end{aligned} \tag{3.10}$$

In the simulation study, the true coherence $\rho$ is changed from 0 to 1 and the biases in the estimated coherence are recorded. Fig. 3.4 shows the sample means of current estimators in Eqs. (2.20)-(2.21), as well as bootstrap estimator, i.e., $\overline{\hat{\rho}_{HB}}$, $\overline{\hat{\rho}}$ and $\overline{\underline{\hat{\rho}}}$ under look numbers $L = 8$ and 40 respectively. Clearly, $\overline{\hat{\rho}}$ is highly biased except for large $\rho$ values, $\overline{\underline{\hat{\rho}}}$ reduces the bias to certain degrees. While the $\overline{\hat{\rho}_{HB}}$ is much less biased for $\rho \geq 0.3$ under $L = 8$ and for $\rho \geq 0.1$ under $L = 40$, showing the unbiased estimation of $\hat{\rho}_{HB}$. For very small $\rho$, $\hat{\rho}_{HB}$ offers significant improvements over the other two estimators although it is still biased to certain extent. The remaining biases decrease asymptotically with the increase of the look number $L$. When $L$ is about 40, the biases are nearly zero.

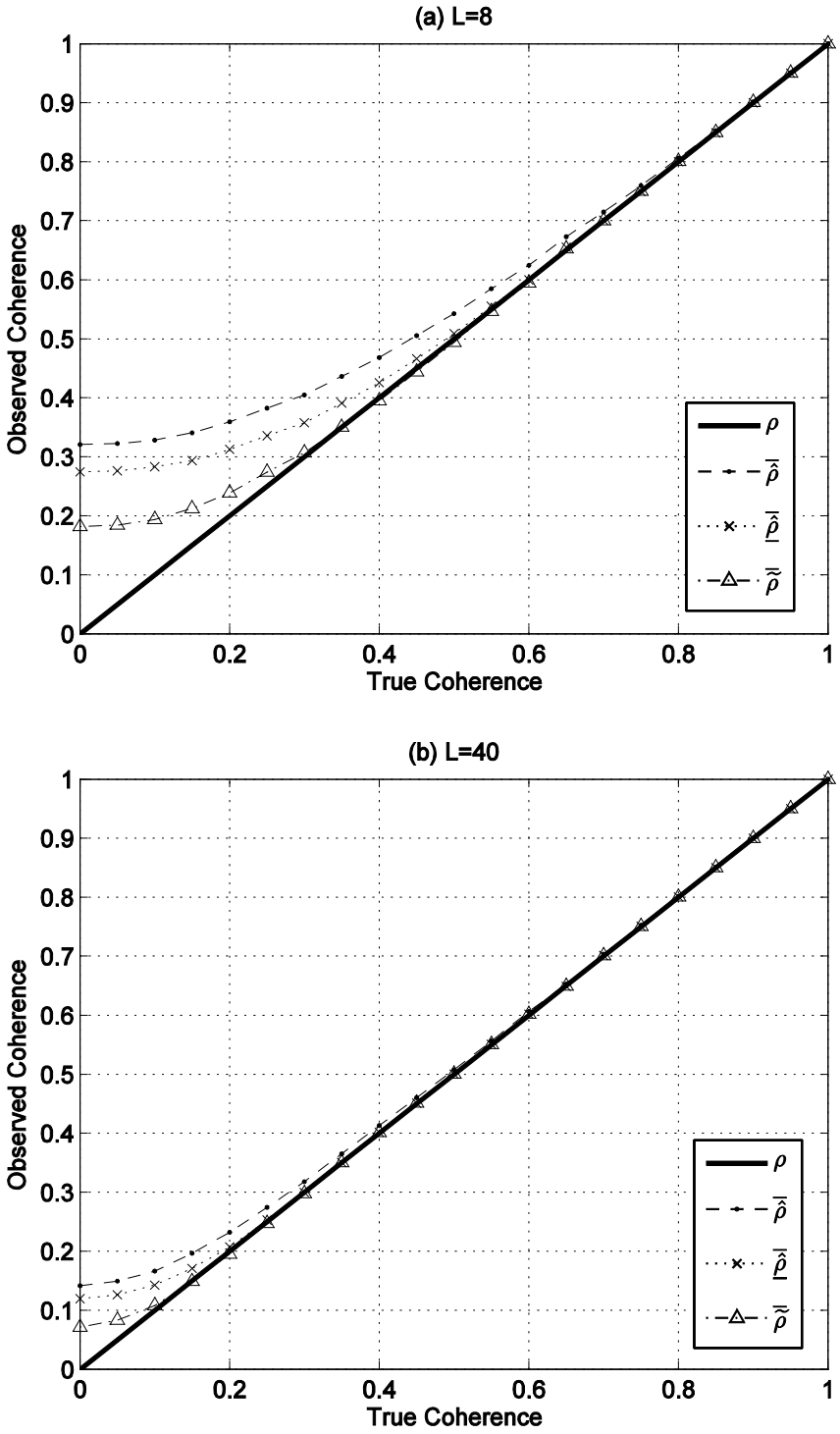


Fig. 3. 4. Coherence biases and their corrections with double bootstrap approach for looks $L=8$ and 40 over a Gaussian scene. $\rho$ denotes the true coherence; $\bar{\hat{\rho}}$ and $\bar{\underline{\hat{\rho}}}$ denote the means of regular sample coherence and its log-sample coherence respectively. $\bar{\bar{\hat{\rho}}}$ denotes the mean of the sample coherence after bootstrapping correction.

The STDs of $\bar{\bar{\hat{\rho}}}$ and $\hat{\rho}$ and the CR lower bound derived in [*Seymour and Cumming*, 1994; *Touzi et al.*, 1999] are investigated for look number $L=8$ and

the results are given in Fig. 3.5. As can be seen, the STD of $\tilde{\rho}$ returns to the upside of CR bound. The higher variability in $\tilde{\rho}$ is not surprising due to the additional variability of bias correction terms $B$ and $C$ in Eq. (3.8).

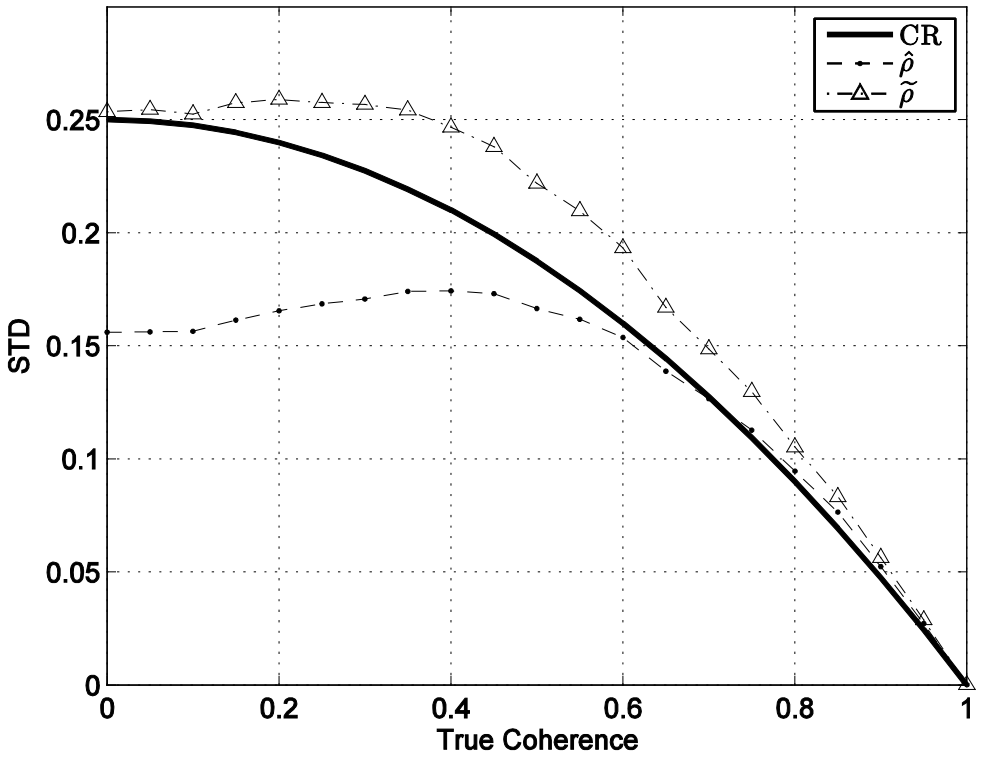


Fig. 3. 5. Standard deviations (STD) of the bootstrapping estimate $\tilde{\rho}$ from Eq. (3.9), regular estimate $\hat{\rho}$ from Eq. (2.2) and the CR lower bound for $L = 8$.

Fig. 3.6 shows results of bias corrections for a non-Gaussian scene with both Eq. (2.19) and the double bootstrap method. Considering that the second-order moment of the $\alpha$-stable distribution does not exist [*Nikias and Shao*, 1995], Eq. (2.2) cannot be applied to the data. A contaminated normal distribution $0.9N(0,1)+0.1N(0,10^2)$ is used to describe the heavy-tailed characteristics of the distribution to simulate the original complex data. We use $L = 20$ and let $\rho$ vary from 0.5 to 1 in which remarkable biases can be observed. Due to the non-Gaussian nature of the distribution, Eq. (2.19) cannot reduce the bias and at times, e.g., when $\rho$ is 0.55 - 0.7, the correction $\hat{\rho}_L^{1st}$ even increases the biases slightly. In contrast, estimate $\tilde{\rho}$ behaves well and the bias removal is mostly

effective. The results demonstrate the validity of the bootstrap based method for non-Gaussian scenes.

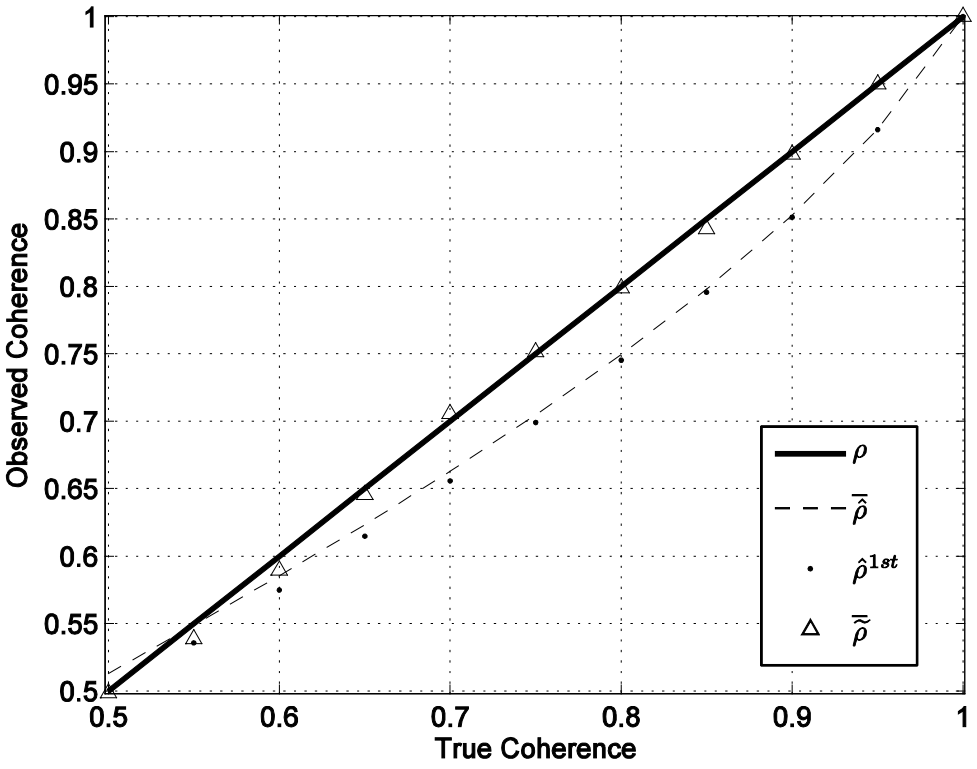


Fig. 3. 6. Comparison between bias corrected coherence $\hat{\rho}^{1st}$ for a non-Gaussian scene with Eq. (2.19) and bootstrapping estimate ‰ for $L = 20$. The true coherence is truncated to the range of [0.5, 1].

Several points should be highlighted for the use of bias corrected estimators. First, the proposed method and current ones use different concept on bias correction, i.e., bootstrapping relies on original observations for a given pixel and directly corrects the bias without the knowledge on neighboring sample coherence and the distribution on the original sample. Bias mitigation can be achieved even for small to moderate sample size included for a given pixel. In contrast, the assumptions constructed in current methods limit the applications of Eqs. (2.19)-(2.21) and bias removal for each pixel is difficult in actual SAR scenes. Second, over non-Gaussian scenes, the bootstrap estimate should be used due to its nonparametric property. Finally, for a homogeneous area under study, coherence estimation from a coherence map after bootstrapping bias mitigation

can be further developed. More precisely, suppose that there is large number $H$ of independent sample coherence $\hat{\rho}_{Li}$,

$$\bar{\hat{\rho}} = \frac{1}{H}\sum_{i=1}^{H}\hat{\rho}_{Li} \tag{3.11}$$

Then unbiased $\rho$ can be obtained by subtracting the bias from estimated $\bar{\hat{\rho}}$. The lookup table of biases under $L=8$ and 40 at Gaussian environments have been established using Monte Carlo simulations and shown in Table 3.3.

Table 3. 3: Lookup table of approximate bias under Looks $L=8$ and $L=40$

| $\rho$ | 0 | 0.05 | 0.1 | 0.15 | 0.2 | 0.25 | 0.3 | 0.35 | 0.4 | 0.45 | 0.5 |
|---|---|---|---|---|---|---|---|---|---|---|---|
| $L=8$ | | | | | | | | | | | |
| $\bar{\hat{\rho}}$ | 0.181 | 0.184 | 0.194 | 0.212 | 0.239 | 0.274 | 0.306 | 0.350 | 0.400 | 0.450 | 0.500 |
| $B$ | 0.181 | 0.134 | 0.094 | 0.062 | 0.039 | 0.024 | 0.006 | 0 | 0 | 0 | 0 |
| $L=40$ | | | | | | | | | | | |
| $\bar{\hat{\rho}}$ | 0.071 | 0.083 | 0.107 | 0.150 | 0.200 | 0.250 | 0.300 | 0.350 | 0.400 | 0.450 | 0.500 |
| $B$ | 0.071 | 0.033 | 0.007 | 0 | 0 | 0 | 0 | 0 | 0 | 0 | 0 |

### 3.2.5 Algorithm

The whole procedure of the developed hybrid method is described as follows.

1. Apply Eq. (3.1) to detect outliers in each timely amplitude data of pixel $P$, and discard them from further processing.

2. Define a window centered on $P$, and compare a neighbor in the window with $P$ by using two timely amplitude data (outliers excluded). During ADT, the estimate $O$ in Eq. (3.2) is first determined by two combined sample, and specified test are then selected. The pixel is regarded as the SHP of the central pixel $P$ if it is not rejected by the test and also connected with $P$. After testing all pixels in the window, the new set including $K$ SHPs can be obtained for $P$. This procedure is repeated until each set is generated for

each spatial pixel.

3. Generate an adaptive multilooking complex coherence map $\hat{\gamma}_{init}$ for a pair of interest $(s_1, s_2)$ based on Eq. (2.2) and corresponding SHPs, and calculate phase STD map $\sigma_\phi$ by Eq. (3.4) and initial $\hat{\hat{\rho}}_{init} = |\gamma_{init}|$. For each pixel $P$, the fringe rate inside optimal window $w$, in which the local phase STD is minimum, is then estimated using Fourier filter. All fringe patterns are then retrieved by Eq. (3.3).

4. Formulate "defringed" observations $X = (x_1, x_2, \mathrm{K}, x_K)$ for each pixel $P$, $x_i = (s_{1i} \cdot e^{-j\hat{\phi}_i}, s_{2i})$, $i = 1, \mathrm{K}, K$ and $e^{j\hat{\phi}_i}$ is compensated phase. By building bootstrap replications from $X$, the bias corrected coherence value $\hat{\rho}$ can be estimated by Eq. (3.9) under the specified first and second order bootstrap sample number $R$ and $M$.

Throughout the hybrid processing chain, the selection of SHPs is the most important step as the results from step 2. can also affect fringe rate estimation and bootstrapping. It is impossible to remove biases in the estimated coherence by using samples from different populations as the bootstrap replications can be contaminated by data from heterogeneous distributions. On the other hand, averaging SHPs can maintain the scattering properties even for low backscattering areas. The operation can therefore enhance the SNR of complex coherence with little loss of spatial resolution.

As stated, using step 4., the bias on each pixel can be mitigated without constraints even for a pixel having only several SHPs, this represents the most relevant differences compared with current methods such as Eq. (2.20) and Eq.(2.21). In fact, since the coherence in the multi-temporal dataset can be estimated more accurately, the coherency matrix for a given pixel can be fully optimized, and its decorrelation mechanism therefore can be explored more thoroughly.

## 3.3 Experimental Results

The validations are implemented over two study areas, one is Los Angeles Basin with $N = 46$ ENVISAT ASAR (ASAR) images, the other is the south of Delft, the Netherlands with $N = 78$ TerraSAR-X (TSX) single polarization stripmap images. All images in a dataset are relatively calibrated and co-registered to the same SAR geometry. These processes are implemented using the GAMMA software. During SHPs selection, a window size of $15 \times 15$ is defined for TSX. Consider that ASAR datasets are merely used to contrast the bias effect over the uniform areas, its window size is defined according to specified looks $L$. The impact of each step of the hybrid algorithm on the estimation accuracy will be evaluated under each error source.

### 3.3.1 Influence of Fringe Rate Estimation on Coherence Estimation

A pair TSX data acquired from Mar. 2011 and Apr. 2011 is selected, in which poor interferometric quality and dense fringe patterns present a challenge for fringe rate estimation. The test site and its original interferometric phase are shown in Fig. 3.7 (a)-(b). For the modified algorithm, the SHPs are collected for each pixel by step 2. and then fringe rate are estimated based on step 3.. For non-adaptive method, the $16 \times 16$ boxcar is used to reduce the influence of strong noise on the mis-estimation of fringe rate. To quantize the effect of fringe patterns on coherence estimation, we calculate coherence values respectively by using interferogram without defringing, defringed interferograms by current method and by its modification. The coherence calculated from defringed interferogram by using SAR geometry and Shuttle Radar Topography Mission (SRTM) DEM are also included as a true. All results are presented in Fig. 3.7 (c)-(f).

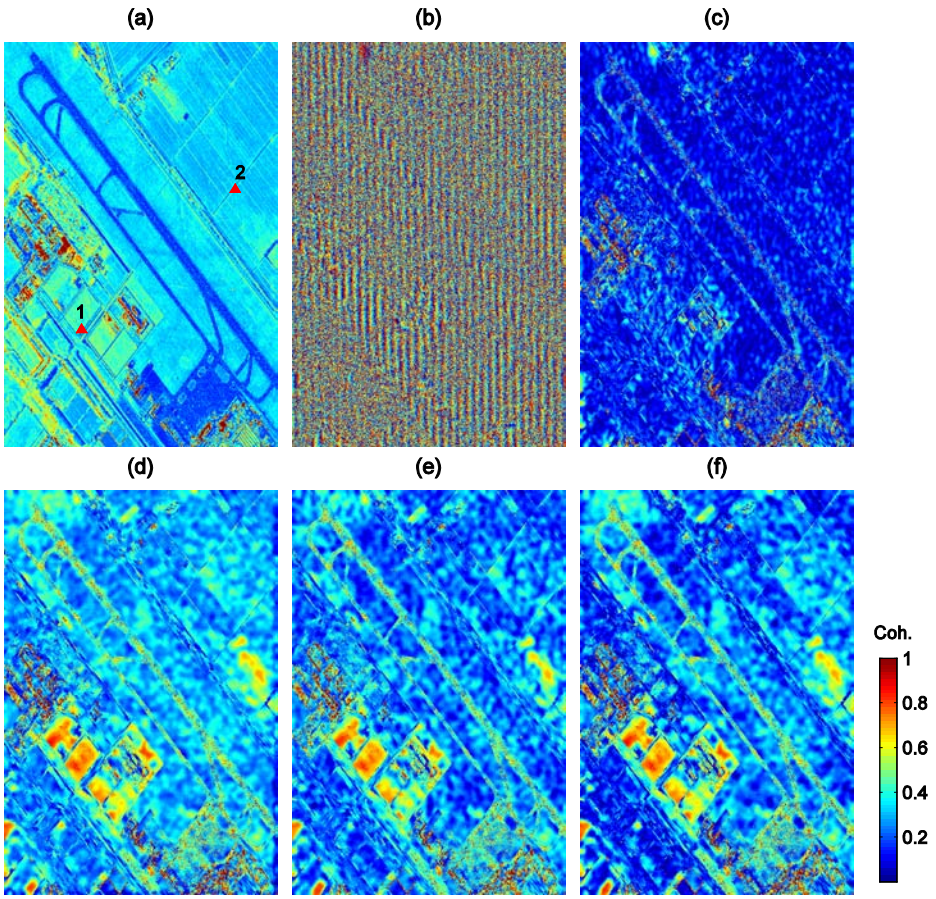


Fig. 3. 7. Coherence estimation using different defringing methods over an area of the south of Delft. (a) incoherent average of $N = 78$ TerraSAR-X amplitude data; (b) original phase of the pair acquired on Mar. 2011 and Apr. 2011; (c) coherence map without defringing (d) coherence map after defringing with non-adaptive fringe rate estimation; (e) coherence map after defringing with the modified fringe rate estimation; (f) coherence map after defringing using SAR geometry and SRTM DEM. Point 1 and Point 2 locate in an texture significant and homogenous area respectively.

It is clear that, compared with (f), the original sample coherence in (c) is strongly underestimated due to the appearance of dense fringe patterns. Removing the phase fringes leads to higher coherence values. However, overestimation of coherence is remarkable for Fig. 3.7 (d) due to the blind use of FFT kernel. This effect has been obviously reduced in the modified method. Note that the coherence in (e) on the bottom left seems to be higher than that in (f). The reason for this is that the coarse DEM from SRTM DEM causes the phase residuals which increase with the perpendicular baseline ( $B_{\perp} \approx 179\mathrm{m}$ ). Thus, the coherence in (f) is actually underestimated in this area.

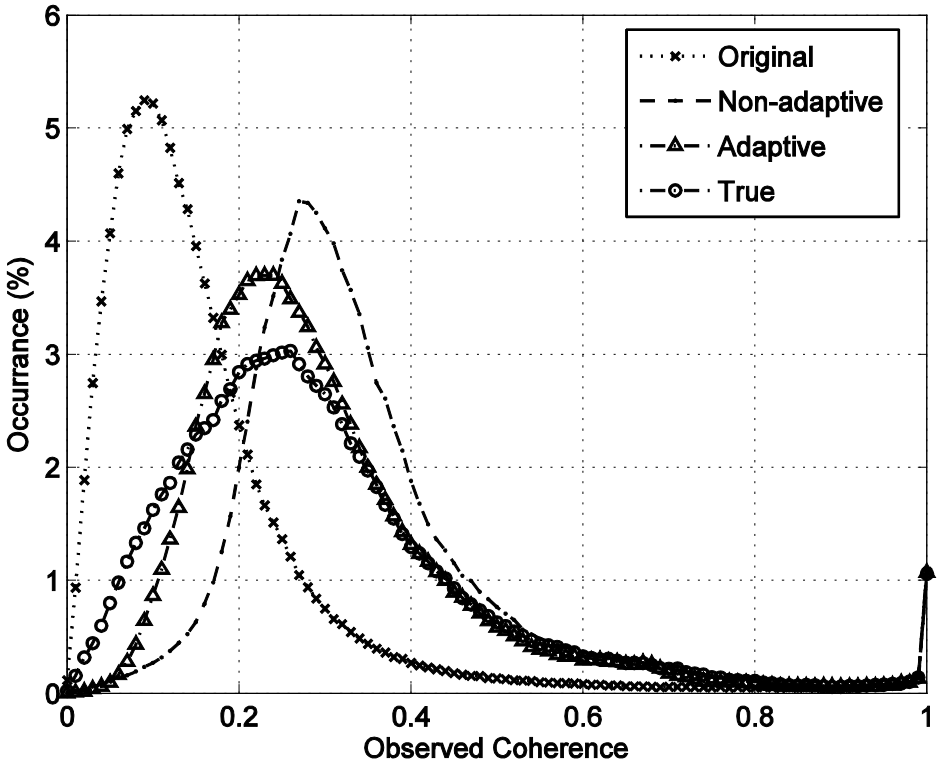


Fig. 3. 8. Histograms of observed coherence of Fig. 3.7(c)-(f).

Fig. 3.8 plots the histogram of the coherence in Fig. 3.7 (c)-(f). It can be seen that the coherence estimated after the modified method is much closed to the "true". Quantitative evaluation in Table 3.4 also supports this improvement, where *root mean squared error* (RMSE) are calculated to measure how close estimated coherence to the true.

$$e_{(\cdot)} = \sqrt{\frac{1}{n}\sum_{i=1}^{n}\left(\hat{\rho}_{(\cdot)} - \rho_{true}\right)^2} \tag{3.12}$$

Where $\hat{\rho}_{(\cdot)}$ denotes estimated coherence without defringing $\hat{\rho}_{Original}$, and with defringing using the non-adaptive $\hat{\rho}_{Non-adaptive}$ and modified method $\hat{\rho}_{Adaptive}$. $\hat{\rho}_{True}$ denotes the coherence estimated from SAR geometry and DEM. $e_{(\cdot)}$ denotes corresponding error and $n$ denotes the image size. Minimum values can be observed from the modified method.

### 3.3.2 Influence of SHP Selection on Coherence Estimation

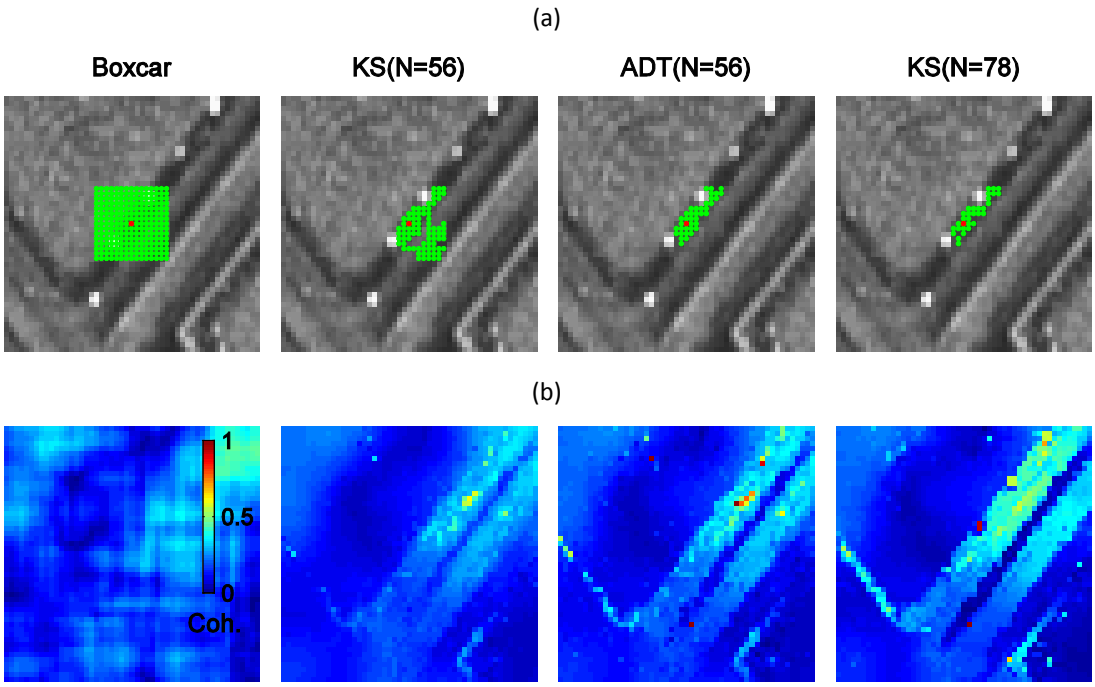


Fig. 3. 9. (a) SHPs selection with different methods. The green pixels are selected samples of the red target pixel (point 1 in Fig. 3.7 (a)); (b) corresponding coherence maps over this area.

The improvements of ADT on SHPs selection against DeSpecKS developed in SqueeSAR [*Ferretti et al.*, 2011], are investigated with $N = 56$ TSX dataset and shown in Figs. 3.9-3.11. The test area is near the red triangle (point 1) marked in Fig. 3.7 (a). As an example, the SHPs (green) of point 1 (red) are shown in Fig. 3.9 (a). This point locates on the road between two structures. For comparison purpose, SHPs selected by boxcar and DeSpecKS under stack size $N = 78$ are also given respectively. Visually, boxcar includes all heterogeneous samples from both the road and structure, while the adaptive methods reduce the inhomogeneity to different degrees. Due to the low power of DeSpecKS with $N = 56$, many heterogeneous pixels cannot be rejected by the test, leading to selected samples grows over boundaries. In contrast, ADT is capable of accurately identifying these different pixels, owing to the improved power of the test. In this case, we use the result from DeSpecKS when $N = 78$ as a true since the power of any test evidently improved with the increase of the sample size.

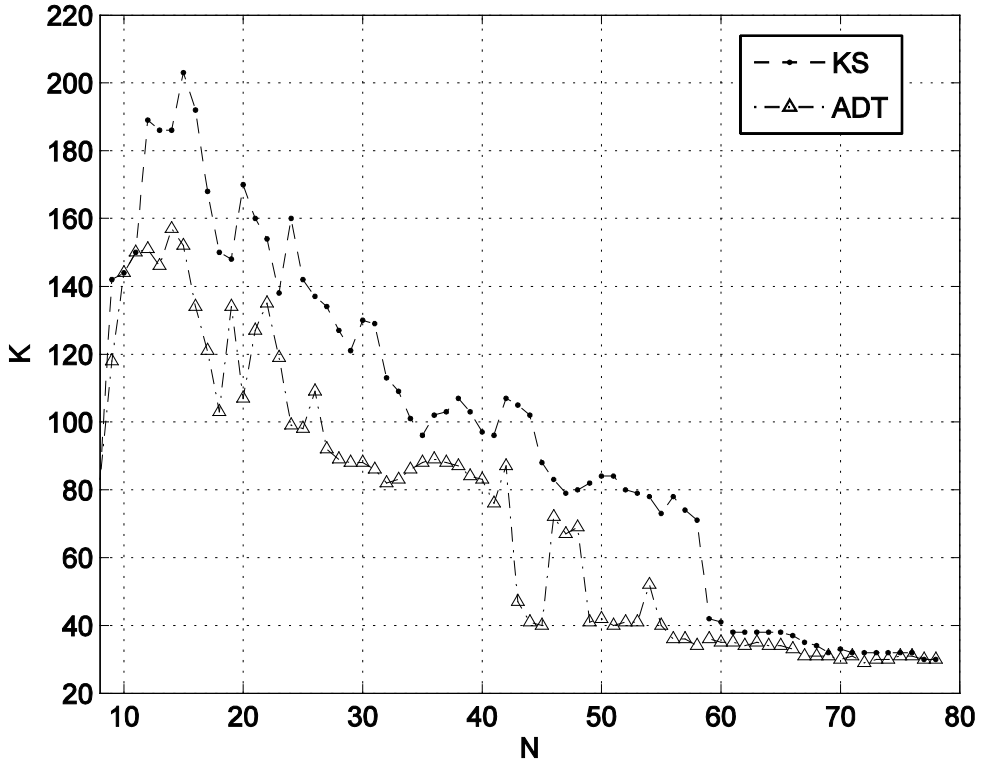


Fig. 3. 10. Selected SHPs number $K$ of point 1 in Fig. 3.7 (a) as a function of stack size $N$ under different statistical tests; the decrease of SHPs number indicates the increase of the power of the test.

The principle behind the SHPs selection is illustrated in Fig. 3.10, where the SHPs number $K$ of point 1 is plotted as a function of stack size $N$. The $K$ decrease significantly with the increase of $N$, showing that the heterogeneous pixels are reducing. When $N$ is large enough, both tests flatten out gradually. However, the convergence of ADT is faster and its sample size is lower than that of the KS. This result is in accordance with the discussion in Section 3.2.2 and explains the reason that why ADT is superior to DeSpecKS.

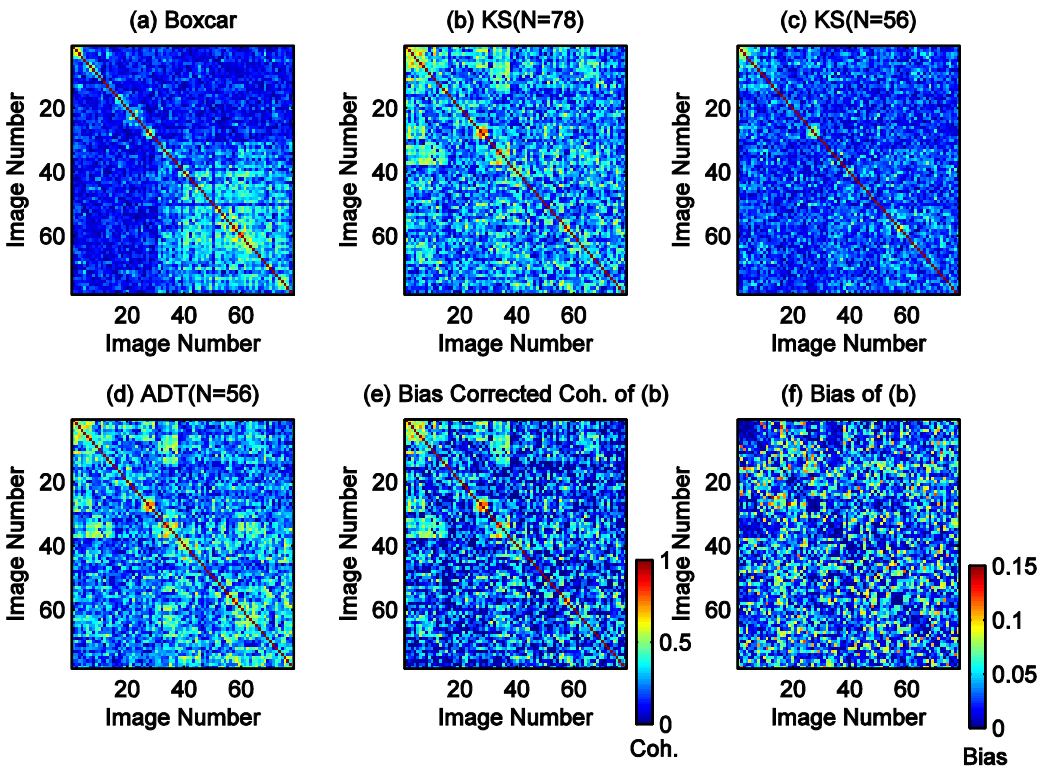


Fig. 3. 11. Estimated coherency matrix from point 1 in Fig. 3.7 (a) using different SHPs selection methods; (a) conventional boxcar; (b) KS with $N = 78$ stack size; (c) KS with $N = 56$ stack size; (d) ADT with $N = 56$; (e) bias corrected coherency matrix of (b) using bootstrap method; (f) estimated bias of (b).

The impact of this step on coherence estimation has been discussed in Fig. 3.9 (b) and Fig. 3.11. To generalize the conclusion above, the coherence map over this area are generated using respective method. As expected, the poorest performance of boxcar can be observed all over the image due to the indiscriminate averaging of neighboring pixels causing complete loss of resolution. On the contrary, the other three methods mitigate this effect better. Compared with DeSpecKS, the details in the results from ADT are closer to those from true, i.e., DeSpecKS when $N = 78$, showing that ADT are able to better follow a scene and maintain sharper features in the coherence map.

The quantitative results are further evaluated using the coherency matrix of point 1, in which off-diagonal elements denote an estimate of the coherence values for all interferograms of the dataset (see Section 2.1.1 for details). In Fig. 3.11, it can be seen that how the decorrelation mechanism for the same point is

impacted by the SHPs selection. We note that boxcar selects the point-wise targets in Fig. 3.9 (a), and therefore its coherence is higher at the bottom right corner. While DeSpecKS when $N = 56$ removes the targets but introduces many heterogeneous pixels showing lower coherence. Therefore, the coherency matrix is underestimated. Compared with the first two estimates, ADT works well and follows the similar decorrelation mechanism with DeSpecKS when $N = 78$. Using Eq. (3.12), we count the RMSE of respective estimate to the true. In Table 3.4, the error of ADT is twice as small as that of DeSpecKS, indicating the significant improvement for coherence estimation.

Table 3. 4: RMSE of the estimated coherence under different algorithms

| Step 2.: Fringe rate estimation | | |
|---|---|---|
| $e_{Original} = 0.179$ | $e_{Non-adaptive} = 0.083$ | $e_{Adaptive} = 0.062$ |
| **Step 3.: SHPs selection** | | |
| $e_{Boxcar} = 0.187$ | $e_{DespecKS} = 0.158$ | $e_{ADT} = 0.082$ |

### 3.3.3 Influence of Bias Removal on Coherence Estimation

Bias correction is tested using both ASAR and TSX datasets. Several uniform areas such as the shrub, bare land, forest, grass and sea are then extracted, in which sufficiently large number independent samples (around 15000–25000 pixels) are included. Their distributions are examined according to the mean of characteristic exponent $\alpha$ in each pair [*Ma and Nikias*, 1995]. If $\alpha$ is close to 2, we consider that the distribution is Gaussian, and vice versa. It should be stressed that since the improvements focus more on coherence estimation with less assumption such as limited sample size and its distribution, we compare $\hat{\rho}$ with $\hat{\rho}$ and its log-sample estimate to validate the bias mitigation. $\hat{\rho}_L^{1st}$, $\hat{\rho}_L^{2nd}$ and $\hat{\rho}_L^{Bs}$ listed below are used to demonstrate the limitations of the current methods over the non-Gaussian scenes.

The estimation procedure is briefed as follows. For the regular statistic, the bias corrected coherence $\hat{\rho}_L^{1st}$ is deduced by inverting Eq. (2.19), where $E(\hat{\rho})$ is

replaced by the $\bar{\hat{\rho}}$ in Eq. (2.20), i.e., $H$ averaged sample coherence $\hat{\rho}_{Li}$. For the second kind statistic, the bias corrected coherence $\hat{\rho}_L^{2nd}$ is estimated by inverting Eq. (17) in [*Abdelfattah and Nicolas*, 2006], where $\underline{m}_1$ is replaced by the $H$ averaged log-sample coherence $\ln(\hat{\rho}_{Li})$ in Eq. (2.21). For the new method, the bias corrected coherence $\hat{\rho}$ in each window is estimated by Eq. (3.9) and then $\bar{\hat{\rho}}$ is obtained by averaging $H$ sample coherence $\hat{\rho}_{Li}$. Further corrected term $\hat{\rho}_L^{Bs}$ is also estimated using $\bar{\hat{\rho}}B$ (see Eq. (3.11)), where corresponding $B$ are listed in Table 3.3. In Eq. (3.9), bootstrap replications $\hat{\rho}^*$ and $\hat{\rho}^{**}$ are estimated by sampling from observations $K$ times. The number of bootstrap samples $R = M = 500$ is used throughout the trials. Similar with the previous studies, unbiased coherence $\rho$ is estimated using the whole pixels in each homogeneous area.

To accurately quantify the results, we estimate $L$ looks sample coherence $\hat{\rho}_L$ using $K$ data along the range direction in the homogenous area. The reason for this is due to the fact that estimated $L$ is highly affected by the scale factor $s$, i.e., $L = s \cdot K$ and $s \approx (\Delta g \cdot \Delta a)/(\Delta G \cdot \Delta A)$ [*Hoen*, 2002], where $\Delta g$ and $\Delta a$ are the pixel spacing of ground and azimuth range, and $\Delta G$ and $\Delta A$ are the spatial resolution of ground and azimuth range. Using sample along one dimension reduce the errors of estimated $s$, and therefore avoid the influence of the mis-estimation of $L$ on bias correction. For ASAR $\Delta G \approx 25$ m and $\Delta g \approx 20$ m, we have $s = 0.8$. For TSX with viewing angle $23.99^\circ$, $\Delta G \approx 2.89$ m and $\Delta g \approx 2.23$ m, we have $s = 0.77$.

Table 3. 5: Coherence estimates and bias corrections using the regular, second kind, and bootstrapping statistics

| $L=8$ | | | | | | | | | |
|---|---|---|---|---|---|---|---|---|---|
| Satellite | Area | $\alpha$ | $\rho$ | $\overline{\hat{\rho}}$ | $\underline{\overline{\hat{\rho}}}$ | $\overline{\hat{\rho}}_{Bs}$ | $\hat{\rho}_8^{1st}$ | $\hat{\rho}_8^{2nd}$ | $\hat{\rho}_8^{Bs}$ |
| ASAR | sea 1 | 1.937 | **0.004** | 0.324 | 0.276 | **0.213** | 0.049 | 0.027 | 0.162 |
| ASAR | forest | 1.908 | **0.218** | 0.352 | 0.304 | **0.258** | 0.179 | 0.172 | 0.227 |
| ASAR | bare land | 1.901 | **0.637** | 0.687 | 0.646 | **0.666** | 0.668 | 0.643 | 0.666 |
| ASAR | sea 2 | 1.766 | **0.006** | 0.254 | 0.216 | **0.107** | - | - | - |
| ASAR | sea 3 | 1.652 | **0.203** | 0.344 | 0.295 | **0.246** | 0.149 | 0.142 | 0.210 |
| ASAR | lake | 1.506 | **0.031** | 0.294 | 0.251 | **0.177** | - | - | - |
| TSX | grass 1 | 1.910 | **0.104** | 0.368 | 0.316 | **0.286** | 0.218 | 0.207 | 0.269 |
| TSX | grass 2 | 1.849 | **0.035** | 0.294 | 0.251 | **0.181** | - | - | 0 |
| TSX | sea 4 | 1.835 | **0.037** | 0.294 | 0.250 | **0.182** | - | - | 0.017 |
| TSX | agriculture | 1.411 | **0.673** | 0.651 | 0.589 | **0.630** | 0.627 | 0.584 | 0.630 |
| $L=40$ | | | | | | | | | |
| Satellite | Area | $\alpha$ | $\rho$ | $\overline{\hat{\rho}}$ | $\underline{\overline{\hat{\rho}}}$ | $\overline{\hat{\rho}}_{Bs}$ | $\hat{\rho}_{40}^{1st}$ | $\hat{\rho}_{40}^{2nd}$ | $\hat{\rho}_{40}^{Bs}$ |
| ASAR | sea 1 | 1.937 | **0.004** | 0.145 | 0.124 | **0.091** | 0.016 | 0.021 | 0.067 |
| ASAR | forest | 1.908 | **0.218** | 0.252 | 0.229 | **0.229** | 0.222 | 0.222 | 0.217 |
| ASAR | bare land | 1.901 | **0.637** | 0.633 | 0.618 | **0.628** | 0.629 | 0.618 | 0.628 |
| ASAR | sea 2 | 1.766 | **0.006** | 0.114 | 0.093 | **0.045** | - | - | - |
| ASAR | sea 3 | 1.652 | **0.203** | 0.229 | 0.205 | **0.202** | 0.195 | 0.195 | 0.202 |
| ASAR | lake | 1.506 | **0.031** | 0.134 | 0.113 | **0.081** | - | - | 0.042 |
| TSX | grass 1 | 1.910 | **0.104** | 0.195 | 0.161 | **0.154** | 0.143 | 0.128 | 0.154 |
| TSX | grass 2 | 1.849 | **0.035** | 0.136 | 0.116 | **0.080** | - | - | 0.038 |
| TSX | sea 4 | 1.835 | **0.037** | 0.139 | 0.117 | **0.085** | - | - | 0.054 |
| TSX | agriculture | 1.411 | **0.673** | 0.653 | 0.611 | **0.652** | 0.649 | 0.611 | 0.652 |

Table 3.5 presents the estimated coherence and its bias correction under looks $L=8$ and 40. As can be seen, the mean of the bootstrapping estimate $\overline{\hat{\rho}}_{Bs}$ is less biased than the mean of the sample coherence $\overline{\hat{\rho}}$ and its log-sample $\underline{\overline{\hat{\rho}}}$ in all scenes. Moreover, $\overline{\hat{\rho}}_{Bs}$ is much closed to unbiased estimate $\rho$ whatever the $\alpha$ is. Similar with Fig. 3.4, for $L=8$ and low coherence value, $\overline{\hat{\rho}}_{Bs}$ is still biased to certain degrees. For $L=40$, the bias can be almost removed even for very small coherence value. The results confirm the capability of the bootstrap method under the small (8 independent) and moderate (40 independent) sample size conditions. Finally, For Gaussian scenes ($\alpha$ nears 2) where the sample size is

sufficient, the bias corrected estimates $\hat{\rho}_L^{1st}$, $\hat{\rho}_L^{2nd}$ and $\hat{\rho}_L^{Bs}$ work well. However, with the decrease of $\alpha$, the mis-estimation of the bias are evident especially for $\hat{\rho}_L^{1st}$ and $\hat{\rho}_L^{2nd}$ under low coherence conditions. It is not surprising since the biases of the existing estimators are larger than that of bootstrapping estimator. The similar results have been given in [*Abdelfattah and Nicolas*, 2006]. Note that in the area of grass 1 for TSX data under $L=8$, no estimate is in accord with the $\rho$. This area is actually around point 2 in Fig. 3.7 (a), in which homogeneous pixels showing different sample coherence can be observed in Fig. 3.7 (f) or Fig. 2.4, and therefore the assumption of local stationarity and ergodicity in mean of the sample coherence breaks down. This demonstrates the risk of using the coherence map based methods over a large area.

The example of bias removal for a coherency matrix using bootstrap method under moderate sample size is presented in Fig. 3.11 (e) and (f). Consider that only $K=32$ SHPs are identified for point 1, the current methods cannot be used. Obviously, after bias mitigation, the coherence values in (e) are smaller than those of (b). Looking at (f), the coherence magnitude of the diagonal elements is not mitigated because the bias of high coherence nears zero. In contrast, larger bias can be observed for the lower coherence magnitude. After the estimate procedure of the whole processing chain, the result in Fig. 3.11(e) can be regarded as the most accurate coherence.

## 3.4 Computational Efficiency

Different datasets have different features, the comparison of all methods on a common case or a point is difficult. However, the improvement of each step against current ones has implied the total progress of the proposed method. From the computational point of view, the estimate procedure spends a lot of CPU time. In SHPs selection, the computing burden is around 0.009 sec. per pixel for DeSpecKS versus 0.012 sec. per pixel for ADT under stack size $N=78$ and an estimate window $15\times15$. In fringe rate estimation, non-adaptive and adaptive

method spend 0.028 sec. per block ($16\times16$ size) and 0.002 sec. per pixel respectively. Compared with local stationary compensations, bias correction is more time consuming. For double bootstrapping, around 10 min. are required for 20000 pixels under the platform of MATLAB. This becomes the main drawback of the new method. To overcome the limit, the *balanced bootstrap* technique [*Davison and Hinkley*, 1997] can be considered as an alternative. This work is proposed for future investigation in Chapter 6.

## 3.5 Conclusions

In this chapter, a hybrid method for coherence estimation based on multi-temporal SAR data has been proposed. The method consists of four data processing steps respectively for outlier detection, adaptive hypothesis testing, improved fringe rate estimation, and double bootstrap based coherence bias correction. A distinctive advantage of the proposed method is that it is almost completely self-adaptive and no prior knowledge or assumption on the data is required. The approach is especially useful for SAR scenes where the underlying Gaussian assumption often breaks down and the sample is insufficient.

Even though the developed methodology is consistent, two weaknesses within the processing chain may be identified. The first weakness is sample size. When data stack size is small, $N<10$ for example, no test estimator can accurately reject $H_0$ if it is false (see Section 4.3 for more details). ADT also increases the risk of mis-selection of estimators because selector statistics may be unreliable enough for small sample problem. Therefore, the increase of sample size can be regarded as the key for accurate SHP selection. The second weakness involves the computational burden of the procedure of bias correction. Double bootstrapping seems to be so time consuming that it is difficult to be used for large datasets. The improvement of our method, however, needs further investigation.

Chapter 4

# Extended InSAR Coherence Estimation for Small MT-InSAR Datasets

## 4.1 Introduction

In this chapter, we further extend the processing chain proposed in the last chapter to small MT-InSAR datasets, where the SHP selection algorithm is not guaranteed to work due to the limited temporal sample size. A new concept is proposed here identifying and using pixels with the same statistical properties in both the spatial and temporal domains [*Jiang et al.*, 2014a].

We start from the theory of data modeling for both low and high resolution SAR images in Section 4.2. The weaknesses of sample selection tests are then stated in Section 4.3. In Section 4.4, we improve the accuracy of selected SHPs by using spatio-temporal pixels and ADT. The Jackknife method with less computational burden will be then deployed to mitigate the bias in Section 4.5. In Section 4.6, quantitative and qualitative results are assessed by both synthetic and real data, followed by a simple conclusion.

## 4.2 Product Model

SAR intensity $I$, which is used to denote the Radar Cross section (RCS) or reflectance $\sigma$, is a basic measurement made by a SAR system [*Lee and Pottier*, 2009; *Oliver and Quegan*, 2004]. Due to speckle appearing induced by the coherent interference of waves, the speckle noise shows a random behavior and causes a pixel to pixel variation in intensities. To mitigate this influence on image interpretation, it is convenient to describe intensity image according to a product

model [*Greco and Gini*, 2007; *Lee and Pottier*, 2009; *Oliver and Quegan*, 2004].

Let $x(P)$ be a multiplicative speckle contribution and $\sigma(P)$ be an uncorrelated RCS at the $P$ th location of pixel, the corresponding intensity $I(P)$ can be modeled as,

$$I(P) = \sigma(P) \cdot x(P) \tag{4.1}$$

Under some certain assumptions [*Hanssen*, 2001], the PDF of $I(P)$ follows gamma distribution with parameters $\sigma(P)$ and *the looks* $L(P)$ [*Lee and Pottier*, 2009]. For convenience, we drop the $(P)$ index.

$$P(I) = \frac{1}{\Gamma(L)}\left(\frac{L}{\sigma}\right)^{L} I^{L-1} \exp\left(-\frac{LI}{\sigma}\right) \tag{4.2}$$

Note that the expectation of $P$ is $E(I) = \sigma$ and its variance is $Var(I) = \sigma^2 / L$. Therefore, for each pixel $P$ over the spatial image, the coefficient of variation (CV) is constant,

$$CV(I) = \sqrt{Var(I)} / E(I) = 1/\sqrt{L} \tag{4.3}$$

In developing speckle filtering algorithms [*Ciuc et al.*, 2001; *Lee and Pottier*, 2009; *Vasile et al.*, 2006], following approximation is usually suggested over a homogeneous (or featureless) area with sufficient sample size,

$$\frac{\delta}{\mu} \approx \frac{1}{\sqrt{L}} \tag{4.4}$$

where $\mu$ and $\delta$ are the sample mean and STD of the local intensity respectively.

Note that the assumptions made in Eq. (4.2) are only available at low resolution image in which the ground targets are much smaller than the resolution cell. For

higher resolution, the texture effect induced by the RCS fluctuations should be considered for describing heterogeneous backscattering media by SAR, such as discrete objects over an urban area. In such cases, RCS $\sigma$ becomes a Gamma distributed variable as a texture descriptor [*Lee and Pottier*, 2009; *Oliver and Quegan*, 2004]. Combining the speckle PDF Eq. (4.2) and RCS Gamma PDF with parameters $\hat{\sigma}$ (the texture mean) and $v$ (a measure of texture heterogeneity), the observed intensity $I$ follows $K$ distribution,

$$P(I)=\frac{1}{\Gamma(L)\Gamma(v)}\left(\frac{Lv}{\hat{\sigma}}\right)^{(L+v)/2} I^{(L+v-2)/2}K_{v-L}\left(2\sqrt{\frac{vLI}{\sigma}}\right) \tag{4.5}$$

with moments,

$$E\left(I^n\right)=\hat{\sigma}^n\frac{\Gamma(L+n)}{L^n\Gamma(L)}\frac{\Gamma(v+n)}{v^n\Gamma(v)} \tag{4.6}$$

Where $K_{v-L}(\cdot)$ is modified Bessel function with order $v-L$. Then CV can be deduced as,

$$CV(I)=\sqrt{Var(I)}/E(I)=\sqrt{1/L+1/v+1/Lv} \tag{4.7}$$

Compared with Eq. (4.3), Eq. (4.7) gradually approaches Eq. (4.3) with the increase of $v$, showing the area under study tends to be homogeneous. In general, parameter $v$ needs to be estimated by iterated solution [ *Joughin et al.*, 1993; *Roberts and Furui*, 2000].

## 4.3 Problems in Sample Selection Tests

Aside from the selection of hypothesis tests described in the last chapter, there are two main problems when using temporal samples in a statistical test. One is that the temporal samples of a pixel may not be identically distributed especially for a dataset with larger time spacing as the property of the pixel may change

over time. As a result, no homogeneous pixels can be found in set $\Omega$, leading to estimated sample coherence equivalent to one for such pixel in all possible coherence maps. Therefore, a dataset with short time intervals should be considered so that $\sigma_1 = \sigma_2 = \mathrm{K} = \sigma$ can be assumed. This may be easier realized for small dataset than large one.

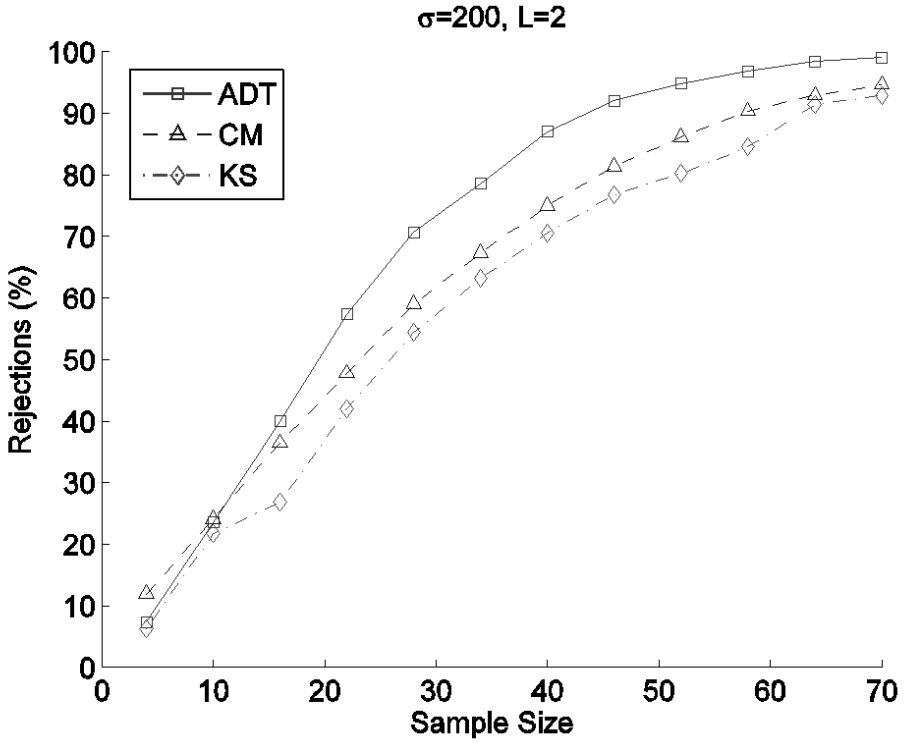


Fig. 4. 1. Simulated power functions for different hypothesis tests using gamma distributed samples with $\sigma$=200, $L = 2$, under level $\alpha = 5\%$. Where $\sigma$ and $L$ are the parameters of Eq. (4.2).

Second, for a given test under the significance level $\alpha$, the power of the test, i.e., the probability of correctly rejecting the null hypothesis $H_0$, is changed with the sample size $N$ and effect size (the difference between the true and value specified in the null hypothesis). The $N$ and effect size toward smaller value, the lower power is, which leads to a wrong decision when $H_0$ is false (the null hypothesis of equal mean has been specified). Fig. 4.1 shows the power of three hypothesis tests as a function of the sample size as calculated through Monte Carlo simulation. The dispersion of the means of two populations from Gamma distribution is set to be $\Delta\sigma \approx 7$. Monotonic increase of the test power can be observed, while for small $N$, the rejection of $H_0$ is more difficult. This will

generate actual problem in the procedure of homogeneous pixels selection especially for small dataset, i.e., set $\Omega$ may include many heterogeneous pixels. A case is illustrated in Fig. 4.2 (b), where the KS test are used to select samples (green) for central pixel (red) under stack size $N=5$. Although less heterogeneous pixels are selected than the boxcar method (Fig. 4.2 (c)), incorrectly selected pixels by KS test can still be easily seen especially over low contrast area. The wrong selection leads to the averaging of pixels with different statistical properties, resulting in significant loss of spatial resolution and mis-estimation of coherence.

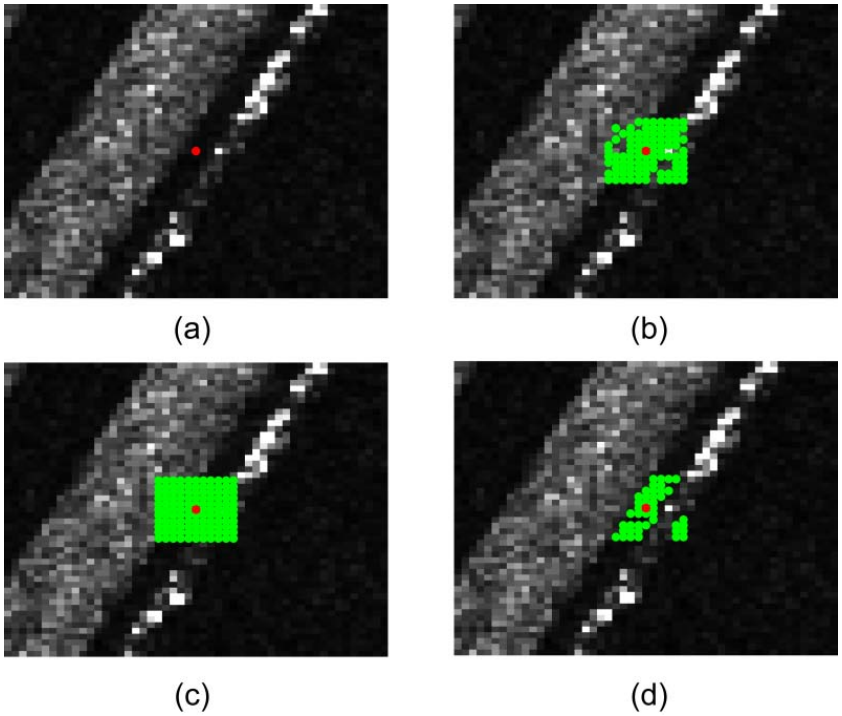


Fig. 4. 2. Test of sample selection for a patch size of $11\times11$. (a) Background intensity image. (b) Results from DeSpecKS. (c) Results from Boxcar. (d) Results from the new method. The red point is the central pixel and the green points are the selected homogeneous samples in set $\Omega$.

## 4.4 Adaptive Algorithm for Sample Selection

A new adaptive algorithm for pixel sample selection is developed based on the following principles:

1. To increase the sample size for the purpose of hypothesis testing, local

samples with uniform scattering mechanisms will be selected first in a small three-dimensional (3D) volume. A statistical model will be used to determine the statistical similarity of the spatio-temporal pixels in the volume. A new data stack will be generated before a hypothesis test is carried out.

2. To preserve features and edge sharpness, the selection of the 3D volume should be adaptive. An edge-aligned window will be used to establish the 3D neighborhood for each central pixel.

3. To find sufficient homogeneous samples in set $\Omega$, an appropriate hypothesis test will be applied in each fixed patch. Different from local filtering, more candidates can be accepted without pixel connection constraint.

The algorithm is implemented in two steps as described below.

### 4.4.1 Local Sample Selection

Suppose there is a small data series $s=[s_1, s_2, \ldots, s_N]$ that is stationary in mean along timely stack, its intensity observation is $I=[|s_1|^2, |s_2|^2, \ldots, |s_N|^2]=[I_1, I_2, \ldots, I_N]$. The first step is to allocate a 3D volume for each spatial coordinate $P$. This can be realized by temporally averaged intensity image,

$$\bar{I}_t = \frac{1}{N}\sum_{l=1}^{N} I_l \tag{4.8}$$

According to [*Lee and Pottier*, 2009], edge-aligned window can be used to determine the most uniform area in which spatial pixels are likely to be more homogeneous. We use this method to image $\bar{I}_t$ for the estimation of 3D volume. It is more advantageous to use $\bar{I}_t$ rather than $I_l$ due to the lower speckle noise variance of $\bar{I}_t$ with a factor of $1/N$, and that the selection of edge-aligned window is more sensitive for texture. In our case, one of the eight directional

sub-windows $w_k$ shown in Fig. 4.3 will be tested in image $\bar{I}_t$ pixel by pixel, and only spatial coordinates in the white region will be preserved. These spatial coordinates together with corresponding temporal samples comprise a 3D volume for pixel at location $P$.

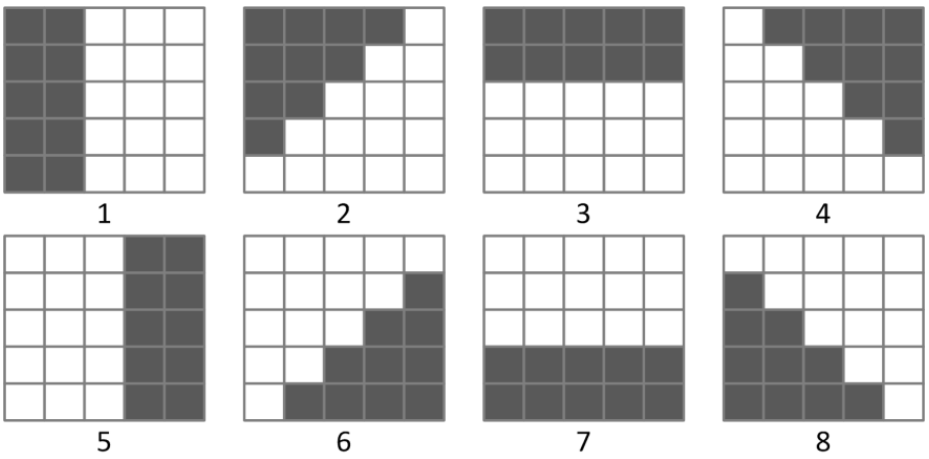


Fig. 4. 3. Example of edge-aligned windows. One of the eight sub-windows (white region) will be used according to the criterion of edge decision Eq. (4.9).

More precisely, a $5\times5$ boxcar window is employed and the local mean $\mu_k(P)$ and STD $\delta_k(P)$ are computed for each $w_k$. The $w_k$ that minimizes the coefficient of variation as defined in Eq. (4.9) is considered as the optimal sub-window,

$$w_k = \arg \min_{k=1,\mathrm{K},8} \left[ \frac{\delta_k(P)}{u_k(P)} \right] \tag{4.9}$$

Since the number of pixels in the white region in Fig. 4.3 is always 15, the total pixels number in each 3D volume should be $15\times N$, and the number of 3D volume equals to the image size of $\bar{I}_t$. It should be noted that for a complicated land cover such as an urban area, the use of edge-aligned window may not work properly. For example, if a tested pixel is a point-wise target with high intensity value surrounded by distributed targets, none of the sub-windows will be considered reasonable. Therefore, suppose that the 3D volume has been prepared for spatial pixel $P$, we further refine the homogeneous pixels in each volume based on the technique of speckle filtering.

As stated in [*Ciuc et al.*, 2001; *Lee and Pottier*, 2009; *Vasile et al.*, 2006], since the most samples in featureless area lie within the confidence interval $[\mu-2\delta,\mu+2\delta]$ where $\mu$ and $\delta$ is defined equally in Eq. (4.4), all elements in the 3D volume can be checked from known $\mu$ and $\delta$ under the assumption of stationary intensity in temporal. The mean $\mu$ can be estimated using the temporal vector $I$, and the STD $\delta \approx \sqrt{Var(I)}$ can be locally estimated as a function of $E(I) \approx \mu$, as given in Eq. (4.3) or Eq. (4.7).

There are two main reasons that Eq. (4.3) should be recommended in actual process. From a technical point of view, RCS fluctuation has a long correlation length in spatial [*Greco and Gini*, 2007], which can be considered as a constant in small window, while Eq. (4.7) is only workable for an area in which the number of sample is large enough [*Oliver and Quegan*, 2004]. On the other hand, parameter $v$ in Eq. (4.7) reduces with the increase of contrast. For texture significant area, we have $v \to 0$ and $CV \to \infty$, this implies $v$ is adjusting for fitting such area. As a result, many heterogeneous pixels showing different statistical properties may be included. From a computational point of view, the estimate of $v$ is very time consuming due to the iterative solution [*Joughin et al.*, 1993; *Roberts and Furui*, 2000]. Therefore, Gamma distributed model is selected and the details of refinement are given as follows:

1. Estimate local mean for each spatial pixel $P$ using timely stack, $\mu(P) = \overline{I}_t(P)$

2. Estimate the local STD $\delta(P)$ using $\mu(P)$ and Eq. (4.4). Drop the index $P$ for convenience, the new confidence interval for refined sample selection is,

$$\left[\mu - \frac{2\mu}{\sqrt{L}} + \varepsilon, \mu + \frac{2\mu}{\sqrt{L}} + \varepsilon\right] \tag{4.10}$$

where $\varepsilon$ is an offset factor used to rectify the biased mean due to the

asymmetric gamma distribution [*Ciuc et al.*, 2001],

$$\varepsilon = \left( \frac{1+e^{(-\frac{4}{\sqrt{L}})}}{1-e^{(-\frac{4}{\sqrt{L}})}} \cdot \frac{2}{\sqrt{L}} - 1 \right) \cdot \mu \tag{4.11}$$

3. Check the membership of all samples in the 3D volume and discard those pixels whose values lie outside the interval Eq. (4.10). A new vector $V(P)$ which includes both temporal and spatial samples is therefore generated at location $P$.

The looks $L$ is prior known, which is constant over the whole 3D images. The steps 1.-3. will be repeated until all 3D volumes have been tested and corresponding vectors $V(P)$ are obtained. It can be seen that after combining both temporal and spatial samples, the maximum number of pixels in each $V(P)$ should be $m = 15 \times N$ i.e., all samples in a 3D volume have been retained, and minimum number however may be less than $N$ due to the truncated tails. We keep the minimum number $m = N$ if $m < N$, i.e., keeping all temporal vector $I(P)$ at location $P$.

### 4.4.2 Nonlocal Sample Selection

Given a moving window with fixed spatial size, all spatial coordinates in the window will be tested with the central coordinate $P$, using individual spatio-temporal vector $V$. Suppose that we are interesting in two vectors $V(P^{'})$ and $V(P)$, the pixel $P^{'}$ can be regarded as a homogeneous pixel of $P$ if it is not rejected by the hypothesis test. After the same procedure for all pixels in the window, the coordinates of all accepted pixels are identified in a set $\Omega(P)$, both pixels being spatial connected and far from $P$. This is different with Step 3. described in Section 3.2.5 where only connected pixels are considered for further calculation. The other difference relates to the alternative hypothesis. As stated earlier, the temporal sample $I(P)$ is assumed to be stationary in mean, and the

vector $V(P)$ is constructed by the mean of $I(P)$ and its expectation $E(V)=\sigma$ reflects the RCS. We therefore focus on the two-sample location problem, i.e., the statistical difference of the means [*Büning*, 1994; *Hogg et al.*, 1975].

Assuming that $V_l(P)\sim F(z)$, $l=1,2,\mathsf{K}\ ,m$, and $V_j(P')\sim F(z-\theta)$, $j=1,2,\mathsf{K}\ ,n$, the shift parameter $\theta\in ¡$, with continuous distribution function $F$, we wish to test,

$$H_0:\ \theta=0 \quad \text{against} \quad H_1:\ \theta\neq 0$$

The most suitable tests for distributions under the location problem have been studied in [*Büning*, 1994; *Kössler*, 2010]. For the case that the two populations have different sample sizes due to the truncation, linear rank tests with various scores are proven to be more powerful than their classical competitors [*Büning*, 1994; *Kössler*, 2010; *M. Neuhäuser et al.*, 2004]. These include $GA$ in Eq. (3.2) and *Wilcoxon test* $WI$ for symmetric distributions with short and mid-long tails respectively. For right skewed distributions, $BWS$ in Eq. (3.2) is used.

Let $O=(\hat{S},\hat{T})$, where $\hat{S}$ and $\hat{T}$ are defined in Section 3.2.2. We define the ADT by its test statistic $A(O)$,

$$A(O)=\begin{cases} GA & \text{if } O\in D_1 := \left\{0.5<\hat{S}\le 1.5, \hat{T}<1.5\right\} \\ WI & \text{if } O\in D_2 := \left\{0.5<\hat{S}\le 1.5, \hat{T}\ge 1.5\right\} \\ BWS & \text{if } O\in D_3 := \left\{\hat{S}>1.5\right\} \end{cases} \tag{4.12}$$

This means that we classify the distributions $F$ into three categories. If $O$ falls in categories $D_1$ or $D_2$, $GA$ or $WI$ will be used. This is suitable for multi-looked intensity series with large look number. For single look series or images with small look number ($L\le 10$), $O$ has a large probability to fall in $D_3$, and $BWS$ is automatically used to test the right skewed distributions. After nonlocal sample selection, the spatio-temporal vector $V$ will be discarded and new set $\Omega_{ADT}$ (we add a subscript "ADT" to distinguish it from $\Omega_{KS}$ estimated

by DeSpecKS) at each coordinate $P$ is formed.

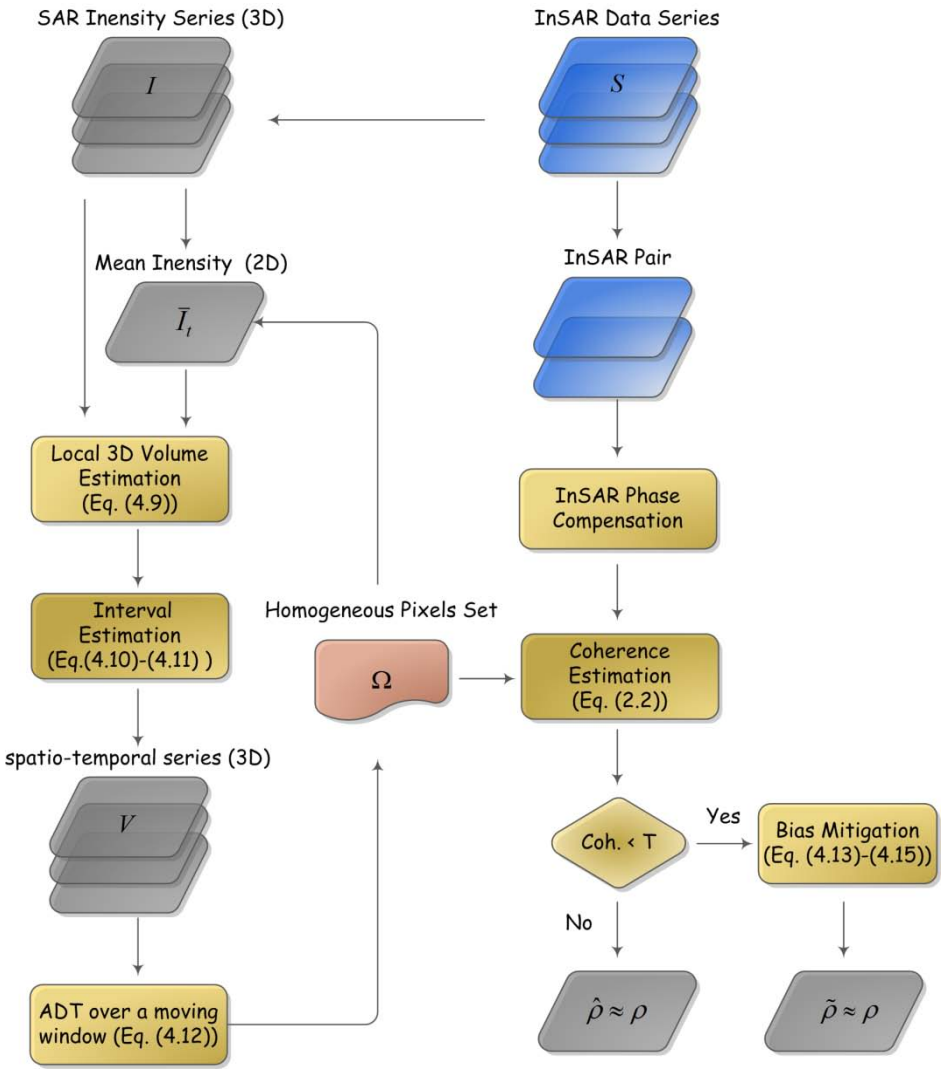


Fig. 4. 4. Flowchart of homogeneous sample selection and coherence estimation; where $V$ is a spatio-temporal vector at each spatial location; $T$ is coherence threshold, and all coherence whose values are less than $T$ will be corrected by Jackknife.

As an alternative, iterative step for both local and nonlocal sample selection are recommended. In Eq. (4.10), only several temporal pixels are initially averaged to determine $\mu$, the variability of $\mu$ ( $Var(\mu) = \sigma / (LN)$ ) may increase the differences between the truncated distributions. Therefore, the ADT may reject two pixels having the same $\sigma$. Averaging $K$ samples (assume that $K$ pixel coordinates at each location $P$ are included in set $\Omega_{ADT}$ ) in temporally averaged intensity images $\bar{I}_t$ improves the estimation. The updated $\mu$ tends to

distribute normally about $\sigma$ with variance $\sigma/(KNL)$. The updated set $\Omega_{ADT}$ that includes more homogenous pixels can then be obtained after applying Eq. (4.10)-(4.12). The flowchart has been shown in Fig. 4.4.

### 4.4.3 Comparison of Test Powers

The efficiency of the ADT is evaluated against two commonly used tests, KS and its weighted alternative *Cramer-von Mises test* (CM) and the results are given in Fig. 4.1. Under significance level $\alpha$=5%, it can be observed that the ADT has higher test power and it also converges faster for almost all the different sample sizes.

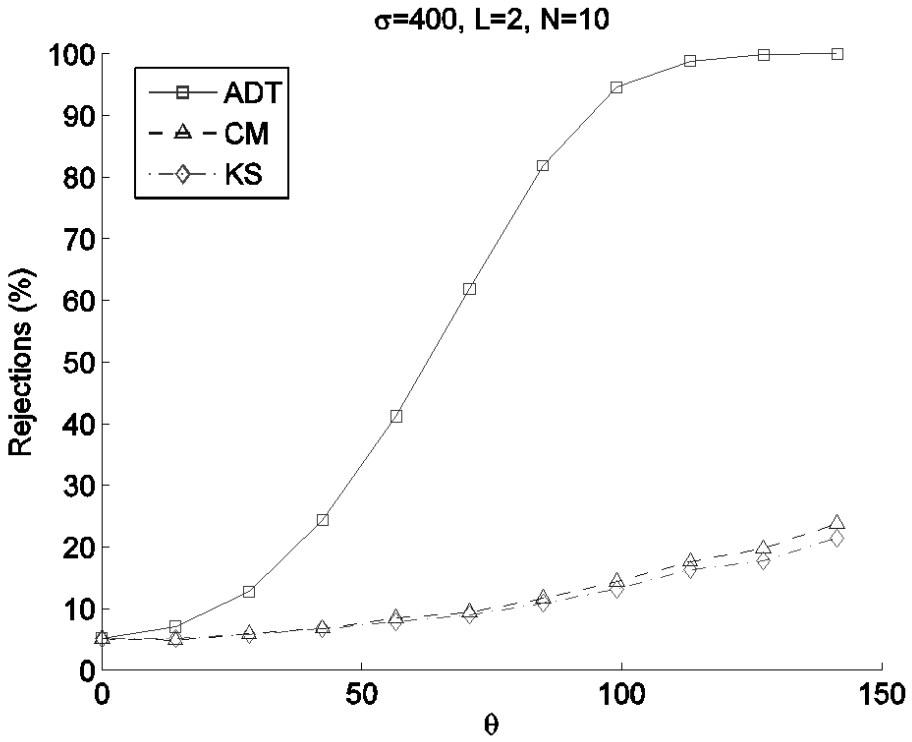


Fig. 4. 5. Power functions of different tests simulated using gamma distributed samples. Samples with a stack size $N=10$, $\sigma$=400 and $L=2$ are tested under different location parameters $\theta$ at significance level $\alpha=5\%$.

The full performances of developed method (spatio-temporal sample selection plus ADT), DeSpecKS (temporal sample selection plus KS test) and CM method (temporal sample selection plus CM test) on comparison of test powers are given in Fig. 4.5, based on Monte Carlo simulations. The shift parameter is determined

by $\theta=k\delta_F$ and $k = 0, 0.05, 0.1, \mathsf{K}, 0.5$ where $\delta_F$ is the STD of distribution $F$. The best test power from the new method can be observed. An increase in the test power results in a decrease of the level of type II error, and therefore further reduces the heterogeneous pixels in set $\Omega$. The difference in the sets resulted from boxcar, DeSpecKS and the new method is shown in Fig. 4.2 where pixels showing low contrast to the central pixel can also be identified by the new method. A quantitative study will be given in the following sections.

## 4.5 Bias Mitigation with Jackknife Technique

After compensation of fringe rates by using an external DEM or 2D local frequency estimation described in Section 3.2.3, the biased coherence can be mitigated by the bootstrapping estimator Eq. (3.9). However, this estimator is so time consuming that bias mitigation for large datasets is deemed unlikely.

To solve the limitation, a computer-intensive method, *Jackknife* is proposed. The technique estimates the bias and the standard error of an estimator when the statistics and/or the distribution are complicated. The advantage of the Jackknife technique is in that it is nonparametric and easy to compute and works in most situations (except for unsmooth statistics [*Efron and Tibshirani*, 1993]). The reduction of the biases in many estimators such as the mean, variance and sample correlation coefficient has been studied [*Efron*, 1981; *Efron and Tibshirani*, 1993; *Miller*, 1974]. Here we use a similar idea to mitigate the bias in Eq. (2.2).

Given a random sample $X = (X_1, X_2, \ldots, X_K)$ where any element $X = (X_1, X_2, \ldots, X_K)$ $X_k = (s_{1k}, s_{2k})$ and $X$ follows an unknown bivariate distribution $F$. Let $\hat{\tilde{\rho}} = \rho(X)$ be an estimator of true coherence $\rho(F)$. The leave-one-out estimator of $\rho(F)$ can be defined by the $k$ th Jackknife sample $X_{(k)} = (X_1, \ldots, X_{k-1}, X_{k+1}, \ldots, X_K)$, $k = 1, 2, \mathsf{K}, K$,

$$\hat{\rho}_{(k)} = \rho\left(X_{(k)}\right) \tag{4.13}$$

The Jackknife estimator of the bias of $\hat{\rho}$ can be evaluated according to Jackknife estimator of the mean $\hat{\rho}_{(\cdot)}$,

$$\hat{B}_{jack} = (K-1)\left(\hat{\rho}_{(\cdot)} - \rho\right) \tag{4.14}$$

where $\hat{\rho}_{(\cdot)} = \sum_{k=1}^{K} \rho_{(k)} / K$. Considering that $\hat{B}_{jack}$ is an approximation of the bias $\hat{B} = E(\hat{\rho}) - \rho$, we can obtain a bias-corrected estimator for $\rho(F)$,

$$\hat{\rho} = \hat{\rho} - \hat{B}_{jack} \tag{4.15}$$

Similar with Eq. (3.9), estimate $\hat{\rho}$ in Eq. (4.15) is dependent completely on the original sample $X = (X_1, X_2, \ldots, X_K)$ and unrelated to the knowledge of the distribution $F$, and therefore workable for both Gaussian and non-Gaussian scenes.

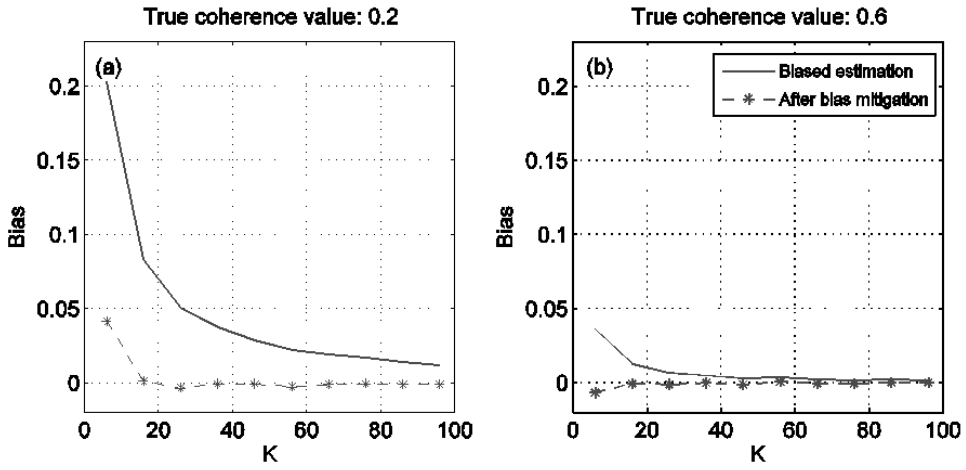


Fig. 4. 6. Coherence biases and mitigation with Jackknife approach under different sample sizes *K* and coherence levels. (a) True coherence = 0.2, and (b) True coherence = 0.6.

A numerical comparison between the bias estimator developed and Eq. (4.15) is given in Fig. 4.6 where the true coherence values are $\rho = 0.2$ and $\rho = 0.6$ respectively. The Y-axis gives the bias between the estimated and the true coherence values, i.e., $\hat{\rho} - \rho$ and $\hat{\rho} - \rho$, and the X-axis represents the sample

size $K$ which is the number of pixels in set $\Omega$. In Fig. 4.6(a), large biases can be observed for $\hat{\rho}$, the biases decrease with the increase of $K$, while the bias-corrected estimates $\tilde{\rho}$ become much less biased and approach 0 when $K$=16. Similar characteristics can also be observed in Fig. 4.6(b) but with lower biases in estimator $\hat{\rho}$ as $\hat{\rho}$ is asymptotically unbiased with the increase of $\rho$. Therefore, bias mitigation for small $\rho$ is more important and this can be implemented by using $\tilde{\rho}$. However, we can see some fluctuations in $\tilde{\rho}$ for small $K$ values, say $K \le 6$. This is not surprising because the information in sample $X$ is limited. 6 observations in $X$ are not enough to describe the characteristics of the data. Therefore, for very small $K$, we still recommend bootstrapping estimator Eq. (3.9).

## 4.6 Experiments and Results

### 4.6.1 Results from Simulated Data

An interferometric pair is simulated from more general form of Eq. (3.10) under Gaussian assumption. The conclusion from the simulation study can also be extended to non-Gaussian scenes due to the nonparametric properties of developed methods

$$\begin{aligned} s_1 &= \sqrt{\frac{\sigma_1}{2}} \cdot \left( s \cdot \sqrt{\rho} + n_1 \cdot \sqrt{1-\rho} \right) \\ s_2 &= \sqrt{\frac{\sigma_2}{2}} \cdot \left( s \cdot e^{-i\phi} \cdot \sqrt{\rho} + n_2 \cdot \sqrt{1-\rho} \right) \end{aligned} \tag{4.16}$$

where $\sigma_1 = \sigma_2 = \sigma$ and $\rho$ is the true coherence. The data stack $I$ with $N = 5$ is simulated from Eq. (4.2), and $L = 2$ is used throughout the simulations. The reason for using a two-look stack is twofold. First, the real data over an area in Macau used later is processed by two-look averaging. The increase of $L$ reduces the auto-covariance between spatial pixels and render the adjacent pixels more independent. Second, the two-look operation improves the estimation of

confidence interval and therefore the selection of pixels in Eq. (4.10).

Two adaptive sample selection methods, the new method and DeSpecKS are used to generate set $\Omega_{ADT}$ and $\Omega_{KS}$ respectively, then coherence maps are obtained by averaging the samples within respective sets. Classical boxcar estimators with $3\times3$ and $7\times7$ window are also included in the comparison. Window size $11\times11$ is set for both adaptive methods. Bias mitigation is also performed for the new method.

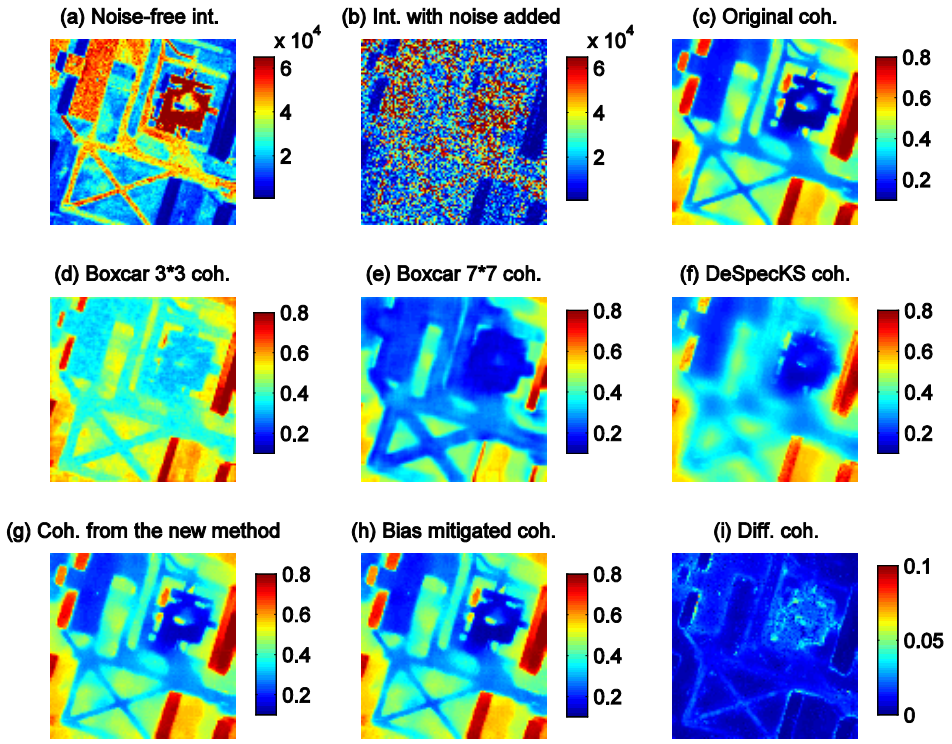


Fig. 4. 7. Simulated SAR images and the estimated coherence. (a) Noise-free intensity image. (b) Intensity image with noise added. (c) Simulated coherence map. (d)-(g) Estimated coherence map by using $3\times3$ boxcar, $7\times7$ boxcar, DeSpecKS and the new method. (h) Bias mitigated coherence map from (g). (i) Difference between (g) and (h).

Fig. 4.7 presents the simulated data and the estimated mean coherence with 130 trials. The noise-free intensity image is challenging for estimating the coherence with adaptive algorithms due to its significant texture. Compared with Fig. 4.7 (c), it is seen that the new method (Fig. 4.7 (g)) works better in preserving the edges and shapes of the features. The boxcar estimators blur the edges of the image. In particular, boxcar with $3\times3$ estimator overestimates the coherence due to the

small sample size, while boxcar with $7\times7$ estimator reduces the bias at the expense of losing the resolution. DeSpecKS (Fig. 4.7 (f)) can preserve the details as long as the spatial contrasts in the original intensity image are enough. Otherwise, mis-estimation can be observed over the image. Finally, the Jackknife estimator (Fig. 4.7 (h)) is used to reduce the bias in the coherence in Fig. 4.7 (g), and their difference is shown in Fig. 4.7 (i). It can be seen that large dispersion occurs in the low coherence area and edges where sample number $K$ in set $\Omega$ is small.

A quantitative assessment of the quality of the estimated coherence has been carried out and the results are given in Fig. 4.8. To make it easier to see the effect of the estimated biases, the estimated coherence from all the methods is truncated to the range of 0-0.4. A robust regression is carried out and the SNR designed for quantifying the estimation quality is calculated (see Eq. (19) in [*Deledalle et al.*, 2011] for more details). It is clear that the boxcar $3\times3$ estimator is significantly biased and has the lowest SNR. The poor performance is considered mainly due to the small $K$ and the loss of the feature structures over the edges. DeSpecKS has less bias and higher SNR but also a large dispersion. This is due to the fact that KS test is based on a small stack size and is feeble to reject the null hypothesis. Thus, the loss of resolution and details reduces the similarity between the original and the estimated coherence. On the contrary, the new method that combines the spatio-temporal pixels and the ADT increases the test power and therefore improves the SNR significantly. The better ability of mitigating the bias is owing to the identification of sufficient samples by using both local and non-local pixels. Finally, estimator Eq. (4.15) further reduces the bias, and the fitted line is much closer to the unbiased results. The highest SNR on Fig 4.8 (d) demonstrates the high accuracy of the method.

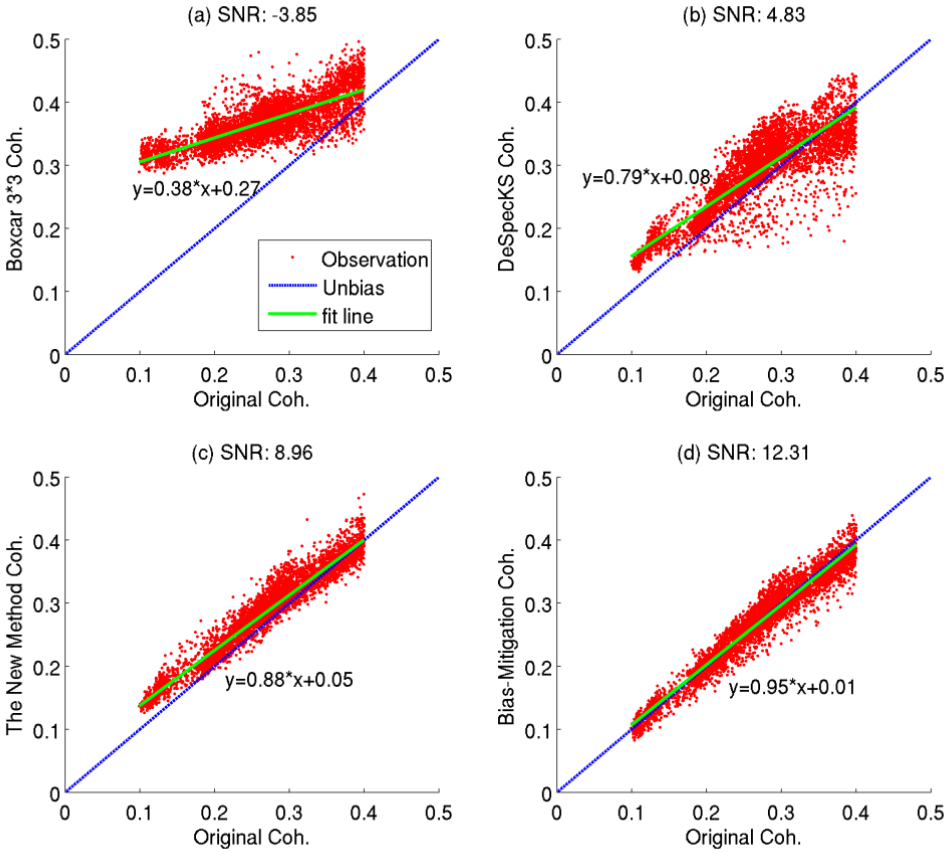


Fig. 4. 8. Quantitative assessment of coherence estimation from different methods. (a) $3\times3$ Boxcar. (b) DeSpecKS. (c) The new method. (d) Bias mitigated based on (c). The larger the SNR is, the smaller the difference between the original coherence and its estimate is.

### 4.6.2 Results from Real Data

We select an area in Macau to assess the effectiveness of the newly proposed algorithm. $N=5$ TerraSAR-X strip-map two-look images (highlighted by red color in the X-axis in Fig. 5.2) acquired from Match 2012 to May 2012 are used for sample selection. The image coverage and their key parameters can be seen in Fig. 5.1 and Fig. 5.2 in the next chapter.

Fig. 4.9 presents the averaged intensity image, the optical image and the estimated coherence. The image pair 20120320 and 20120331 is arbitrarily selected for the experiment. It can be seen from the intensity image and the optical image in Fig. 4.9 (a) and (b) that the spatial features in the area are

complicated and present a great challenge for all algorithms. The proposed method is able to follow the features in the scene and preserve the sharp boundaries. The estimated coherence map is accurate without loss of spatial resolution. However, the results from DeSpecKS seem degraded. The point-wise targets and linear objects are especially blurry. Similar to previous studies [*Lee et al.*, 2003; *Vasile et al.*, 2006], the results from the boxcar estimator are the poorest in quality.

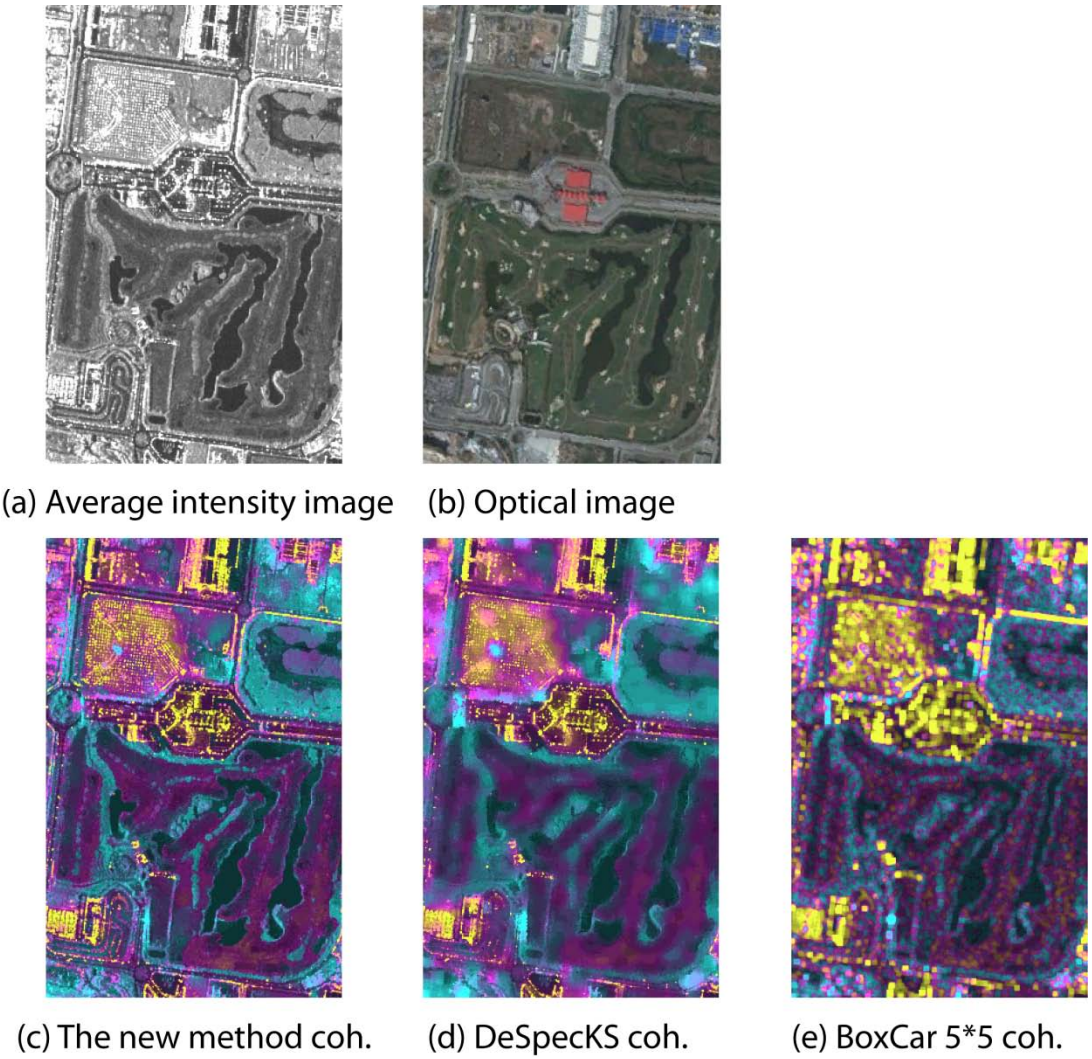


Fig. 4. 9. (a) Incoherent average of intensity images. (b) Corresponding optical image form Google Earth. (c)-(e) Estimated coherence from the proposed method (bias mitigation is included), DeSpecKS and the $5\times5$ boxcar.

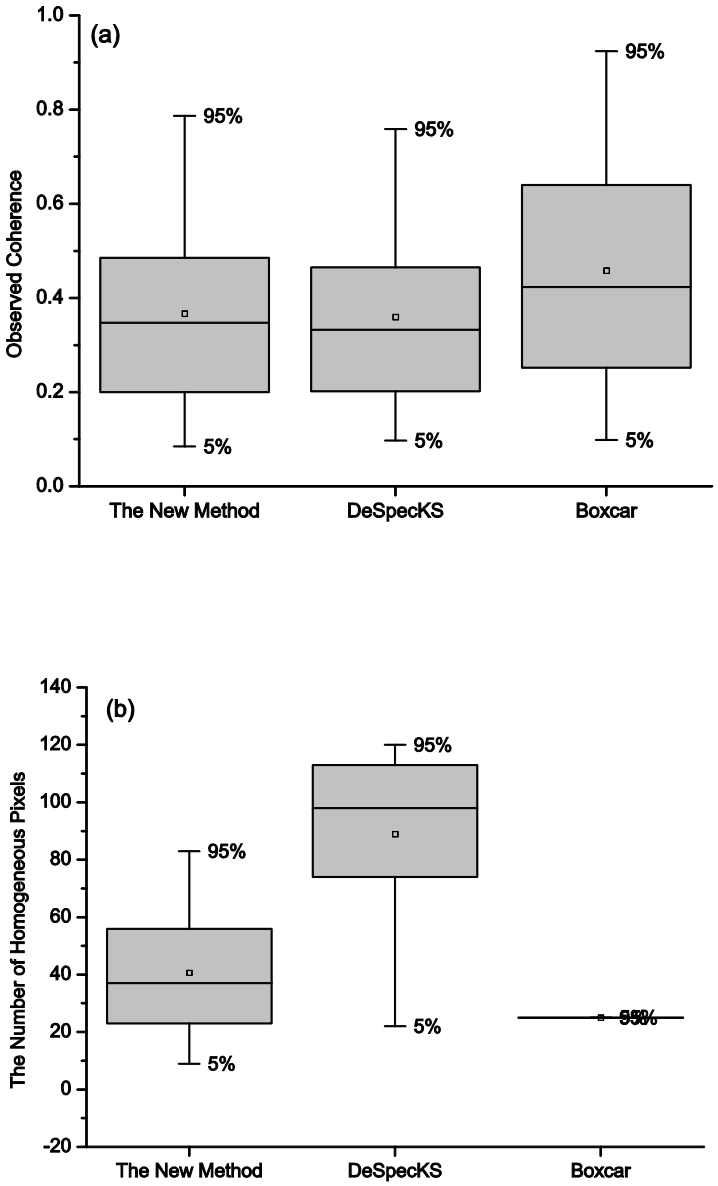


Fig. 4. 10. (a) Boxplots of estimated coherence maps. (b) Boxplots of maps of the number of homogeneous pixels. The 95% and 5% denotes the empirical 95% and 5% quantiles respectively. The square denotes the mean value.

The statistical difference is presented by boxplot in Fig. 4.10. In Fig. 4.10 (a), the boxplot of the spatial coherence based on boxcar estimator is significantly different from the adaptive methods. It seems that the spatial dispersion of the coherence from the new method is slightly larger than that of DeSpecKS. This is possible as the texture of the image is sharp. The boxplots of the number of homogeneous pixels $K$ at sets $\Omega_{ADT}$ and $\Omega_{KS}$ in Fig. 4.10 (b) support this

point. That is, DeSpecKS resembles more pixels to average and therefore makes the coherence map smoother. The average number of similar pixels collected by the DeSpecKS is up to $K = 90$ (total 120 neighbors for each pixel). On the contrary, the average number of neighbors identified by the new method is $K = 42$ only. More specifically, 5% of the pixels have larger than 84 neighbors. These pixels are located in the uniform areas. 5% of the pixels have less than 9 neighbors and correspond to the point-wise targets. The remaining pixels are at the edges with different spatial extension.

## 4.7 Discussions

From a computational point of view, adaptive methods introduce more computational load than the boxcar based methods, while the improvement introduced by the spatio-temporal SHPs selection requires a processing time that approximately doubles than that required by DeSpecKS. However, the computational efficiency of Jackknife for bias mitigation is thirty times faster than that of double bootstrapping developed in Section 3.2.4. This can be considered as an essential progress of the new method. During the actual process, an adaptive procedure can be used to reduce the CPU time, i.e., it is possible to use the initial coherence map to drive the bias correction. Empirically, the bias will be corrected only for $\hat{\rho}$ less than threshold $T$.

We should further point out a common issue in pixel selection when this kind of algorithm is applied. As stated above, under the assumption that the same type of radar targets have similar intensity values, the homogeneity of pixels can be evaluated by means of local statistics [*Chen et al.*, 2012; *Ferretti et al.*, 2011; *Vasile et al.*, 2006; *Vasile et al.*, 2008]. This condition is almost satisfied for flat terrains such as flat vegetation and urban areas. However, over the mountains areas, the dependence of the radar image's brightness (the magnitude of intensity) on the local surface slope complicates the problem. Based on the radar scattering model [*Goering et al.*, 1995], the RCS is a function of local incidence

angle, and the nonlinear relationship may significantly affect the image intensity even if the neighboring pixels belong to the same objects. Moreover, the observed intensity is not directly related to the desired slope when a surface lies in either shadow or layover [*Chen*, 2001]. For example, multiple parts of an illuminated surface contribute to the same range bin, where the front and back faces of a mountain generate different degrees of brightness, leading to image distortions. In order to mitigate such effects in rugged terrains, a smaller window size described in Section 4.4.2 is suggested, in which a constant surface orientation is assumed and strong elevation change along slant range direction is unlikely.

Finally, we pay a special attention for coherence calculation based on Fractional Lower Order Statistics under high resolution scenes [*Bian and Mercer*, 2010]. In that case another estimator is deduced under symmetric $\alpha$-stable distribution,

$$\underline{\hat{\rho}} = \frac{\left| \left\langle s_1 s_2^* \left| s_1 \right|^{\frac{\alpha_1}{2}-1} \left| s_2 \right|^{\frac{\alpha_2}{2}-1} \right\rangle \right|}{\sqrt{\left\langle \left| s_1 \right|^{\alpha_1} \right\rangle \left\langle \left| s_2 \right|^{\alpha_2} \right\rangle}} \tag{4.17}$$

It can be seen that Eq. (2.2) in Section 2.1.1 is a special case of Eq. (4.17) when the characteristic exponents $\alpha_1 = \alpha_2 = 2$. The smaller values of $0 < \alpha_i < 2$ implies the department of Gaussian environment. We should highlight that $\alpha_i$ usually describes the tail of the distribution [*Nikias and Shao*, 1995], and reduces its value over heterogeneous areas. The situation is likely to happen if boxcar is using. However, the pixels in set $\Omega$ estimated by adaptive sample selection algorithms are more homogeneous so that $\alpha_i \approx 2$. Therefore, there is no significant difference found between Eq. (2.2) and Eq. (4.17) even for high resolution scenes. The comparison of two estimators therefore is not performed in this thesis.

## 4.8 Conclusions

An adaptive method has been proposed to improve the accuracy of coherence estimation under small datasets condition. The method combines both spatial and temporal pixels and emphasizes preserving the scattering properties, reducing heterogeneous pixels and not degrading the image quality. In addition, a Jackknife method for mitigating biases is proposed to improve the computational efficiency.

Extensive tests of the proposed method have been carried out using both simulated and real datasets. The results have demonstrated its values, especially over areas with rich textures. More accurate coherence estimation should benefit a wide range of applications such as InSAR parameter extraction. This point will be confirmed in the next chapter.

Chapter 5

# Accurate Extraction of MT-InSAR Temporal Decorrelation

## 5.1 Introduction

The previous chapters have shown how InSAR coherence can be accurately estimated under various conditions.

In this chapter, we perform a more extensive coherence analysis over a variety of surfaces, temporal and spatial baselines to provide a quantitative measure of temporal decorrelation which has been difficult to model or isolate. Our results will provide some new insights into MT-InSAR applications of coherence [*Jiang et al.*, 2014a].

## 5.2 Study Area and Dataset

In order to highlight the influence of coherence estimation on the extraction of temporal decorrelation, we select an area in southern Macau, China (Fig. 5.1). The main advantages of selecting this area include its stable weather and seasonal conditions, and abundant surface types, which ensure that the scattering features of a surface almost dominate the loss of temporal coherence. Furthermore, the area is challenging for coherence estimation due to its rich textures and limited data samples.


Fig. 5. 1. Location of the area for the study.

A total of $N=12$ TerraSAR-X (TSX) single look complex (SLC) images with a strip-map mode covering the time period from 20110904 to 20120627 are used. The TSX X-band sensor collects this VV polarimetric dataset from a nominal altitude of 514 km with a spatial resolution of approximately 3 m and a look angle of $41^{\circ}$. The perpendicular baseline for the possible interferometric pairs varies from 289 m to -359 m. The details of temporal and perpendicular baselines are shown in Fig. 5.2.

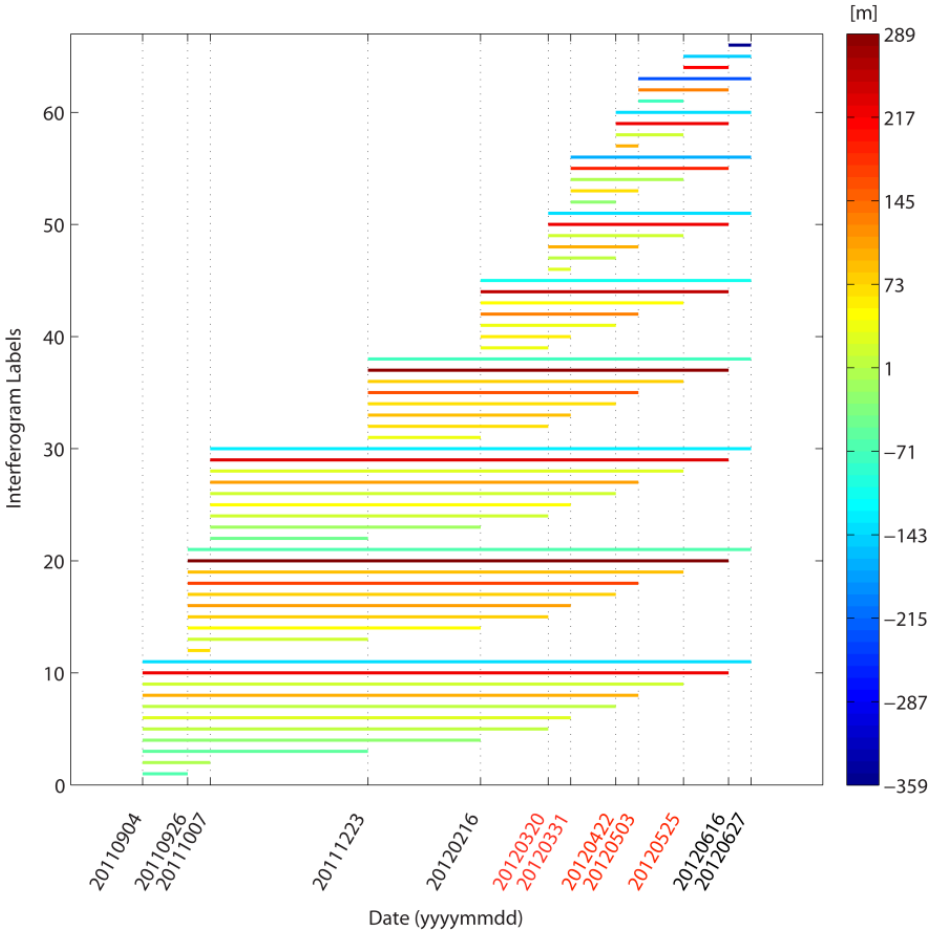


Fig. 5. 2. Perpendicular and temporal baselines of the selected interferometric pairs. The SAR data highlighted in red are used to evaluate the performance of different methods for coherence estimation in Fig. 4.9.

## 5.3 Data Processing

### 5.3.1 Interferometric Processing and Filtering

All the SLCs are registered to the same reference geometry with an accuracy of more than 0.1 pixels. These processes are implemented using the GAMMA software. An area of $4.4\times5.2$ km is selected for interferometric processing. No band-pass filtering is implemented before generating the interferograms. Considering the limited data stack size, we use the spatio-temporal sample selection algorithm developed in Chapter 4 to estimate the off-diagonal elements of the covariance matrix in Eq. (2.3), and 66 interferometric coherence maps are obtained. The parameters used are in accordance with those in Section 4.6.2. In

addition, coherence data series are also estimated by using the conventional boxcar method with a window size of $5\times5$ pixels. The phase components are compensated by a 5 m resolution DEM for both methods.

To evaluate the temporal decorrelation over various types of land cover, a land use map is required. The two-stage classification algorithm developed for multi-temporal SAR data is deployed in this thesis [*Engdahl and Hyyppa*, 2003]. Instead of the $5\times5$ Lee filtering used in [*Engdahl and Hyyppa*, 2003], we use homogenous pixels to adaptively drive the spatial despeckling of the intensity stack before the classification. Comparison of some of the filtered images over a complex scene is shown in Fig. 5.3.

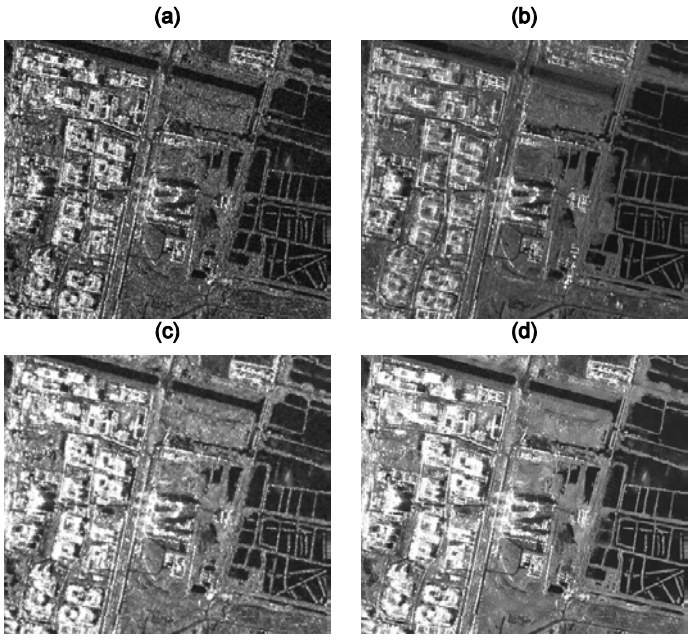


Fig. 5. 3. (a) The original SAR image acquired in 20120216; (b) incoherent average of 12 SAR images; (c) the filtered image with the $5\times5$ lee filter; (d) filtered image with the developed method.

Clearly, the filtered image in Fig. 5.3(d) can follow the features of the scene without loss of the resolution. Contrary to this, the image from the Lee filter in Fig. 5.3(c) is blurry. It is worth noting that such a sample size ($5\times5$) is not enough to diminish the speckle noise, implying a noisy image and therefore inaccurate classification.

### 5.3.2 Land Cover Classification

The classification algorithm is composed mainly of two steps, determination of the information layers and the selection of a classifier. Only observations (coherence and intensity) estimated from the developed method are used for this purpose.

*Information Layers*

The first step aims to select input images from the whole series (66 coherence maps and 12 SAR images). To extract layers showing significant features with different land covers and simultaneously reduce the dimensions of the dataset, the principal component transformation (PCT) method is employed. According to [*Engdahl and Hyyppa*, 2003], we first subtract the incoherent average of the 12 SAR images from each of the (filtered) SAR images before using PCT as this step reduces correlation between the images and highlights changes from the averaged image. Nevertheless, the coherence time series are not centered by subtracting the temporally averaged coherence image due to the fast decorrelation of the X-band images over the study area and the very limited number of the image pairs at the minimum acquisition interval (11 days).

The first principal component (PC) is along the axis of the maximum variance, representing most of the variation in the input dataset. Variation in the open water induced by wind conditions can be highlighted by this layer. In addition to open water, we also observe great variations over the infrastructures in Fig. 5.4. The false color composite image in Fig. 5.5 again emphasizes the frequent activities in the four months over the test site. Therefore, masking out the open water before PCT operation should be performed to reduce the signals from the water surface in the first PC and to highlight stronger signals from areas being developed. The masking of the water is implemented by thresholding the mean of the intensity images and the DEM map shown in Fig. 5.6(a). The training

sample is selected by visual analysis of both of the images.

(a) 20111007 (b) 20120216

Fig. 5. 4. The filtered SAR images acquired in 20111007 (a) and 20120216 (b); some man-made activities can be seen in the center left of the scene.

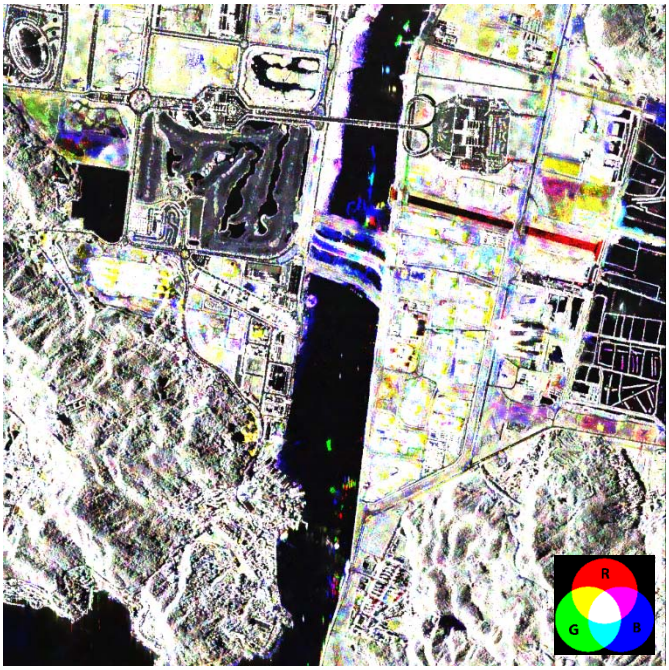


Fig. 5. 5. The false color composite image in SAR coordinate. (Red: 20110926, Green: 20111007, Blue: 20120216); the movements of ships at different acquisitions can be seen on the ocean surface.

A DEM can also assist *Normalized Difference Vegetation Index* (NDVI) to distinguish the forest area in this special case as most of the vegetation locates on the hills (Coloane Island and so forth). The NDVI map in Fig. 5.6(b) is derived from a LANDSAT-5 image with spatial resolution $30\times30$ m at the imaging

period 20090102. Very low values of NDVI (< 0) correspond to barren areas of rock, sand, or snow. Moderate values (0-0.3) represent shrub and grassland, while high values (>0.3) indicate temperate and tropical rainforests [*Weier and Herring,* 1999]. Compared with Fig. 5.4 in which the images were acquired in 2011, the infrastructures in the center left of the image show higher NDVI values in Fig. 5.6(b). This indicates that the man-made activities have accelerated degradations of the vegetation in the area over the two years. We regard the area where the NDVI is higher than 0.2 and the elevation is higher than 10m to be forest area. The residual and grassland in the flat terrain will be classified in the second step.

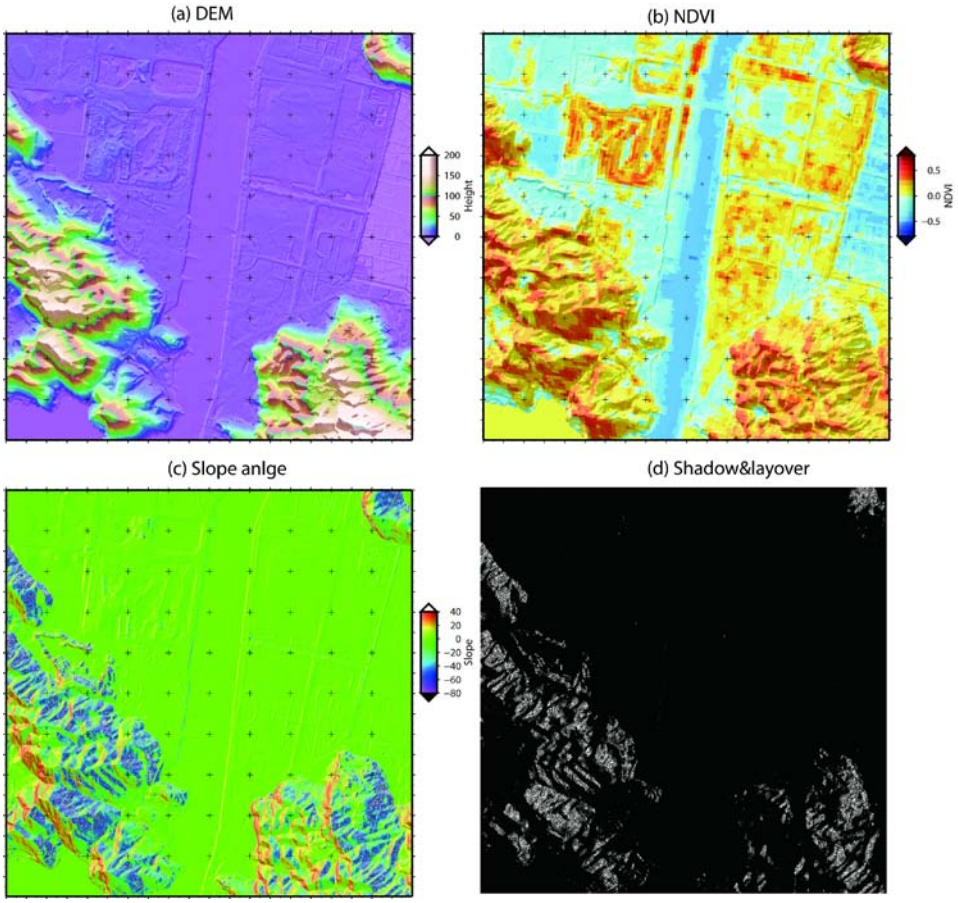


Fig. 5. 6. Auxiliary data in SAR coordinate; (a) DEM; (b) NDVI; (c) local slope angle in degree; (d) shadow and layover. The bright areas indicate shadows and those with layover.

The areas with shadow and layover are determined by means of SAR reference geometry and the local slope angle, and shown in Fig. 5.6(c)-(d). We mask out these areas to reduce the errors for both classification and PCT analysis.

After removing the temporal mean and masking out open water, forest, shadow and layover areas, the PCT is applied to the intensity time-series. The plot of the eigenvalues in Fig. 5.7 shows the percentage of the variability of the individual principal components. The first three PCs accounting for 60% of the total variation can be clearly found.

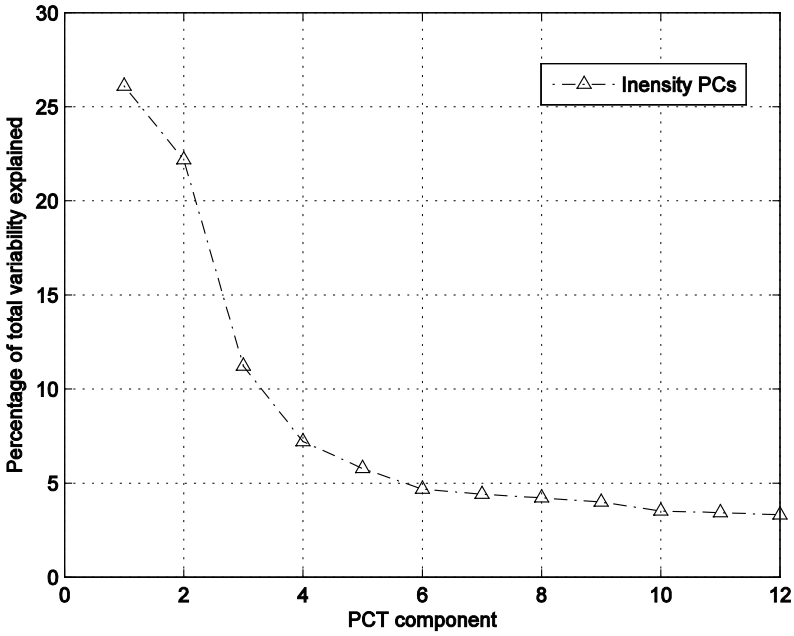


Fig. 5. 7. Percentage of the variability in the masked intensity dataset as a function of the PCT components.

Two coherence images within a certain interval are also selected. As shown in Chapter 1.1.2, the magnitude of coherence depends on SAR geometry and target parameters. The temporal change (i.e., random motion of scatterers and change of the scatterers) dominates the decorrelation. Therefore, the temporal components of coherence maps are first extracted using the coherence decomposition technique (see Section 5.4 for details). The component with short temporal baseline can be used to separate bare land (including wetland), grassland and man-made structures, while the component with long temporal baseline is used to highlight developing areas due to fast decorrelation.

*ISODATA Classification*

The information available from the pre-processing techniques discussed above is used for the classification of land use categories. Six images are chosen as input layers to the ISODATA classifier,

(1) Temporally incoherent average of the intensity time series;
(2) First PC of the intensity time series;
(3) Second PC of the intensity time series;
(4) Temporal average of the temporal components of the coherence maps with minimum temporal baselines (11 days);
(5) Temporal average of the temporal components of the coherence maps with long temporal baselines (66 days);
(6) NDVI map

The third PC of the intensity series is not included due to the limited information that it contains relevant to classification. All images are rescaled to range [0, 255] (8bit) before the classification.

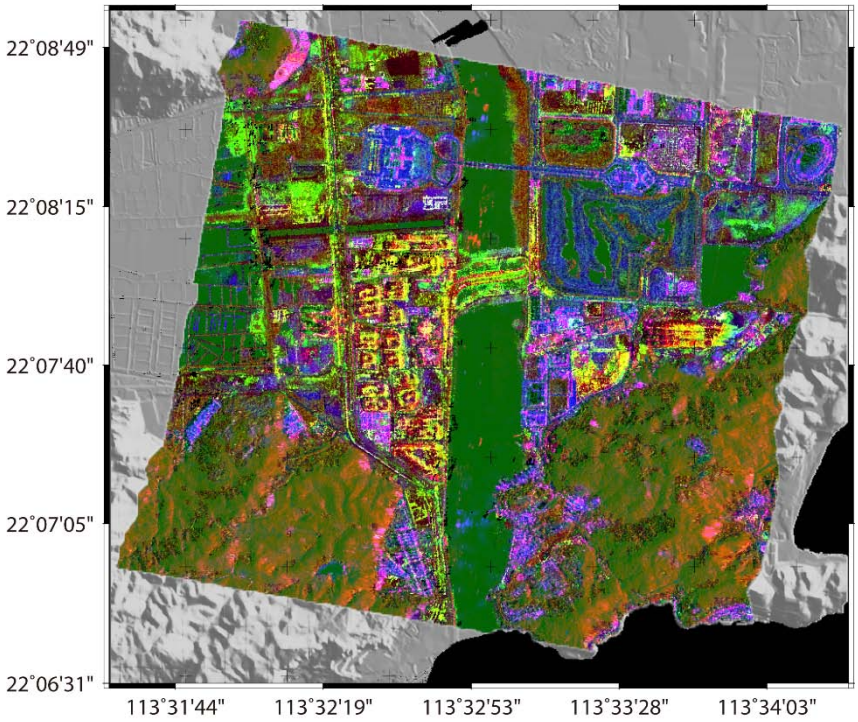


Fig. 5. 8. The false color composite image in geographic coordinate. (Red: (1), Green: (2), Blue: (4)).

The ISODATA unsupervised classification calculates class means in the data space

and then iteratively clusters the pixels using minimum distance techniques. The procedure stops until the sample number in each class changes by less than the change threshold or the maximum number of iterations is reached [*Tou and Gonzalez*, 1974]. In our case, the best results are achieved with 16 clusters using 5% change threshold and 30 iterations. Considering the rich texture, only forest areas are filtered with a $3\times3$ majority filter. Finally, we combine different clusters to six classes, according to the visual interpretation from both Google optical image and RGB image composited by images (1), (2) and (4) (Fig. 5.8). Three of the 16 ISODATA clusters correspond to the "Developed Area", two to "Grassland", seven to "Developing Area", and two to "Bare Land". The "Forest" and "Open Water" correspond to a single ISOCLASS cluster. Fig. 5.9 illustrates the classification results in geographical coordinate for the Macau area.

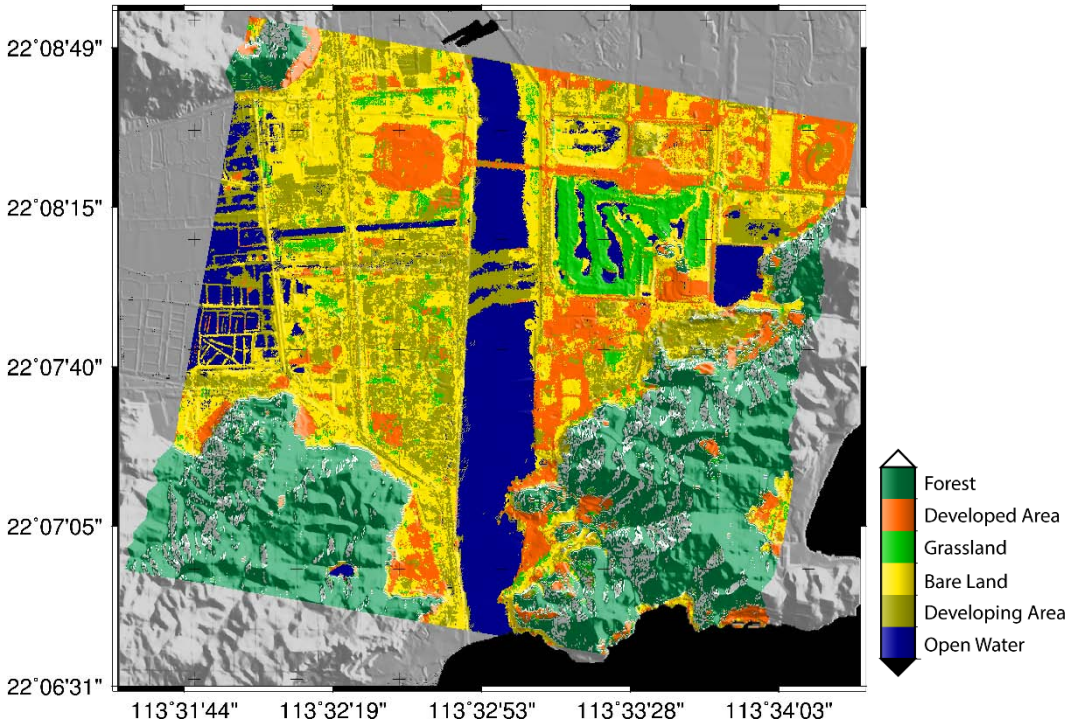


Fig. 5. 9. The land cover classification for the Macau area.

The accuracy of the land cover classification is not assessed due to the lack of the inventory data. The maximum overall accuracy of 90% for six classes has been reported in [*Engdahl and Hyyppa*, 2003]. We believe that the achieved classification accuracy is reduced in this case since the studied scene has a highly

temporal variability. On the other hand, previous studies have reported poor accuracy in classifying urban classes using SAR data [*Wegmuller and Werner*, 1997; *Strozzi et al.*, 2000; *Engdahl and Hyyppa*, 2003]. However, it is enough for us to evaluate the impact of coherence estimation on extraction of the temporal decorrelation as identical classification map is used for both methods in the following analyses.

## 5.4 Coherence Decomposition

The coherence mainly consists of three components,

$$\hat{\rho} = \rho_{thermal} \cdot \rho_{spatial} \cdot \rho_{temporal} \tag{5.1}$$

where $\rho_{thermal}$ depends on SAR sensor system thermal noise and can be generally ignored for modern SAR systems [*Wang et al.*, 2010; *Wei and Sandwell*, 2010]. The temporal decorrelation $\rho_{thermal}$ describes the physical change on the Earth surface between image acquisitions. The spatial component $\rho_{spatial}$ depending on the SAR imaging geometry will be compensated for observation $\hat{\rho}$. There are two components in $\rho_{spatial}$, namely volumetric decorrelation $\rho_{volume}$ and surface decorrelation $\rho_{surface}$. The former is not considered in the case as the test site is not in a high penetration area such as a pine forest and an icy terrain [*Hoen and Zebker*, 2000; *Wei and Sandwell*, 2010]. Thus, we assume $\rho_{volume} = 1$ and estimate $\rho_{surface}$ as follows [*Gatelli et al.*, 1994],

$$\rho_{spatial} = \frac{B_A - |\Delta f_A|}{B_A} \cdot \frac{B_R - |\Delta f_R|}{B_R} \tag{5.2}$$

where $B_A$ and $B_R$ denote the bandwidths in azimuth and range respectively; $\Delta f_A$ denotes the Doppler frequency difference and $\Delta f_R$ is the wavenumber shift. All the terms in Eq. (5.2) are known except for $\Delta f_R$. According to the coherence decomposition technique [*Wang et al.*, 2010], we first estimate the

local incidence angle $\theta - \alpha$ (similar to Fig. 5.6(c)) for each interferometric pair using SAR system parameters and an external DEM, and then infer $\Delta f_R$ by associating models Eq. (5.3) and Eq. (5.4) [*Wang et al.*, 2010],

$$\Delta f_R = -\frac{c}{\lambda} \cdot \frac{B_n}{R \tan(\theta - \alpha)} \tag{5.3}$$

$$\alpha = \arctan\left( \frac{\sin(\theta)}{\Delta R / \Delta h + \cos(\theta)} \right) \tag{5.4}$$

Where $c$ is light velocity, $\lambda$ is the wavelength of SAR signal, $B_n$ is normal baseline, $R$ is sensor-target distance, $\theta$ is incidence angle, $\alpha$ is local terrain slope, $\Delta R$ is the difference between two neighboring slant ranges and $\Delta h$ denotes height difference.

As a result, each estimate of an off-diagonal element in a coherency matrix can be decomposed and 66 temporal coherence components for each method can be obtained.

## 5.5 Results

To look at the relationships between the estimated temporal decorrelation and the surface type, five classes of land cover, i.e., water, forest, bare land, developed area and grassland are chosen. For each class, the mean of temporal decorrelation in the coherence map sequence is plotted as a function of a temporal baseline. On all the scatters maps in Fig. 5.10, exponential degeneration of the coherence can be clearly observed from the results except over open water. The details of the results from the two methods are however quite different and two advantages of the new method are highlighted below.

One advantage is the quality of the time series of temporal coherence. The adaptive approach can avoid selecting heterogeneous pixels that exhibit different

time evolutions. Therefore, it is possible to significantly enhance the SNR and results in a less noisy time series. In this case, the dispersion of time series over almost all the classes is reduced. However, the improvement in the forest area is not significant, probably because the short wavelength radar signals interact mostly with the upper parts of the canopies which can be moved randomly by winds. Furthermore, temporal decorrelation may vary remarkably with seasons and types of the forest [*Koskinen et al.*, 2001]. Finally, the effect of volume decorrelation may be a factor, whose magnitude depends on vegetation thickness, SAR geometry (i.e. baseline and incidence angle) and transmissivity of the vegetation [*Santoro et al.*, 2007a].

The second advantage is the accuracy of the estimated time series. For example, over the open water, we can observe bias in the magnitude of the coherence estimated by the conventional method as the theoretical coherence over water should be close to zero. Moreover, the variation of the estimated coherence time series from the conventional method is much smaller than that from the proposed methods. For example, most of the temporal coherence values are located in the intervals 0.2 to 0.4, leading to difficulties in applications such as classification. On the contrary, this intersection is reduced in the new method. For example, the coherence values are near 0 for water bodies, 0.1 to 0.3 for bare land, 0.2 to 0.4 for grassland, and 0.4 to 0.6 for developed areas. Therefore, the added resolution from the new method can improve the performance of coherence-based applications.

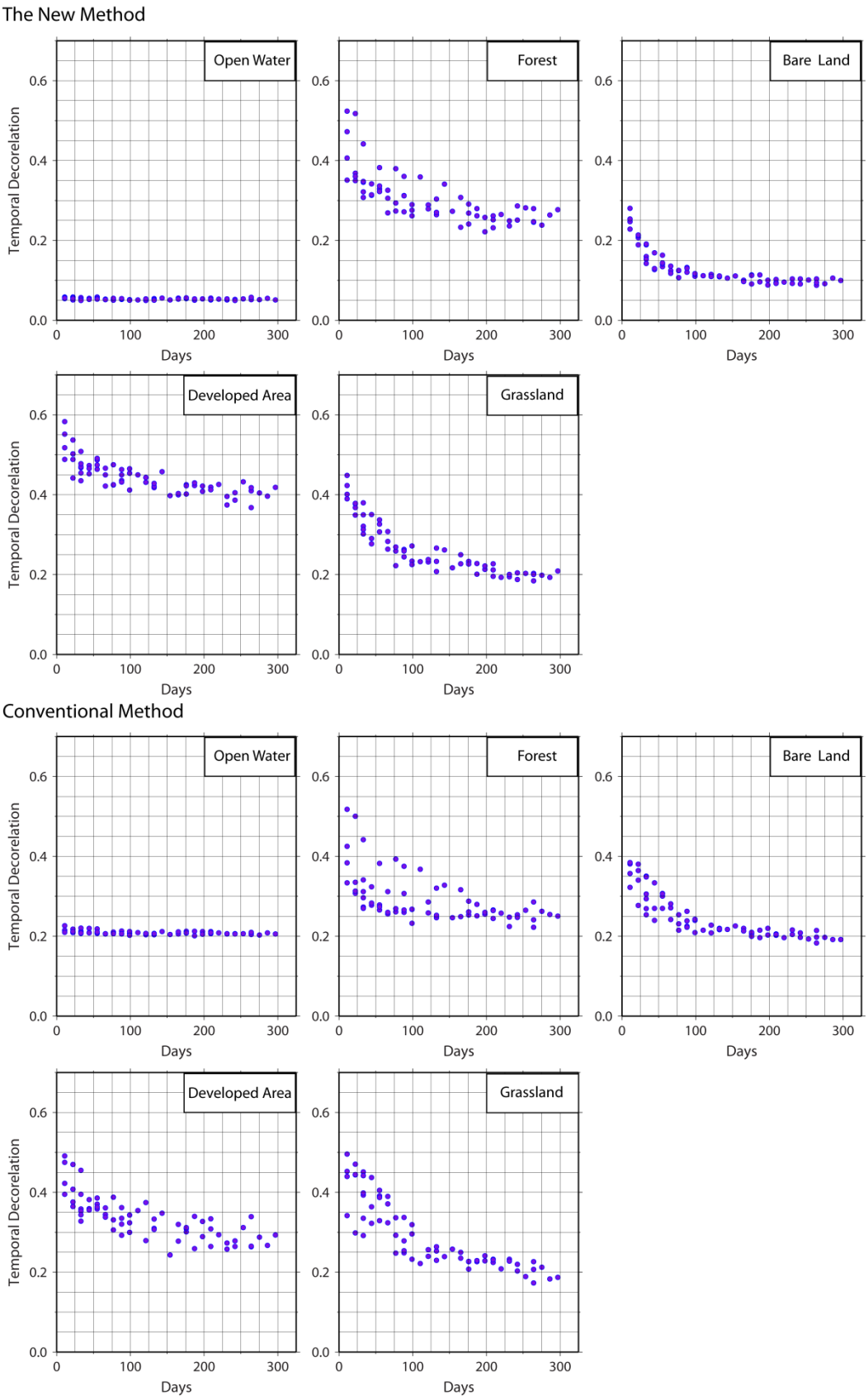


Fig. 5. 10. Comparison of temporal decorrelation time series over five classes of land cover obtained with the new and the conventional methods

## 5.6 Conclusions

The effectiveness of the newly proposed method for extracting temporal decorrelation has been investigated with a TerraSAR-X dataset over an area of Macau. The results from the study have shown that compared with the boxcar estimation, the extracted time series from the new method are less noisy. The improved results have further proved that temporal decorrelation is land-cover type dependent. The phenomenon cannot be easily observed from the results obtained using the existing methods. We believe that, for accurate inversion of geophysical parameters based on coherence, better algorithms, such as the ones proposed in this thesis, should be applied, and the most commonly used boxcar method should be avoided, especially over areas with rich textures.

Chapter 6

# Conclusions and Recommendations

Conventional InSAR phase measurements have been proved very effective for geophysical parameters inversion. However, almost all interferograms suffers from signal decorrelation and no phase measurement is possible. Coherence provides a new route for this technique by exploring the similarity of a series of echoes at the same position. The applications have been successfully applied to various branches of geoscience, such as surface classification, change detection, estimation of snow penetration depths, and extraction of vegetation parameters. However, the accuracy of the final products is usually unsatisfactory due to inaccurate coherence observations. The existing methods for coherence estimation are at a preliminary stage of development and therefore far from optimal. This thesis has mainly focused on systematically characterizing sources of error in coherence estimation, and developing algorithms to mitigate such errors and relax the constraints.

## 6.1 Research Contributions

The contributions of the research presented in this thesis are:

1. The sources of error that affect accurate coherence estimation are modeled and analyzed quantitatively. It has been shown that the appearance of image texture leads to overestimation of sample coherence and the error depends on the surface types and the sample sizes. The appearance of fringe pattern leads to underestimation of sample coherence and the error increases with the local frequency of the fringe pattern. In addition, the use of fringe rate algorithm may inversely overestimate the coherence, especially over noisy areas. Finally, a biased estimator (Eq. (2.2)) overestimates sample coherence

and the error decreases with the increase in both the number of looks and the true coherence.

2. Under the framework of MT-InSAR, a hybrid method for accurate coherence estimation has been developed, which integrates outlier detection, adaptive hypothesis testing, adaptive fringe rate estimation and double bootstrap to mitigate three main sources of error. It has been shown that the algorithm can improve the accuracy of coherence estimation with fewer assumptions and an almost self-adaptive procedure. Therefore, the method is more pragmatic and applicable.

3. An extended coherence estimation algorithm which associates spatio-temporal sample selection with Jackknife estimator has been developed to accurately estimate coherence matrices. Its successful application to TSX data over an area in Macau has answered two important questions: (i) how to preserve scattering properties and reduce heterogeneity when the data stack size is small; and (ii) how to improve computational efficiency of bias correction for a large spatial dataset.

4. The features of temporal decorrelation over various land covers have been analyzed using the newly developed method. It has been observed that the extracted time series over areas with rich textures are less noisy and biased.

## 6.2 Further Work

There are several areas of InSAR coherence work that can further benefit from this research, including:

1. **Phase filtering.** As introduced by *Baran et al.*, [2003], coherence can serve as an indicator for Goldstein interferogram filtering. However, biased sample coherence can mislead Goldstein filtering and result in under-filtered areas of low coherence (high noise). Using the bias-mitigated estimators developed

in Chapter 3 and Chapter 4 can avoid overestimation of the coherence and therefore optimize the filter performance [*Jiang et al.*, 2013c; 2014d].

2. **Fast and robust homogeneous pixels selection.** In Section 4. 7, the sample selection tests have been shown to be very time-consuming as each hypothesis test needs to be implemented M-1 times for each pixel (window size is M). It is a significant weakness for a large temporal and spatial dataset. Under the assumption that a temporal sample can be stationary in its mean, the central limit theorem (CLT) can help to construct a confidence interval for each pixel under approximate Gaussian assumption. In substituting hypothesis tests with confidence intervals, all neighboring pixels located in the intervals can be regarded as SHPs of the central pixels. The CPU time can be immensely reduced without any loss of the accuracy due to simple logical operations and known statistical models [*Jiang et al.*, 2014b].

3. **Distributed Scatterer InSAR technique (DS-InSAR) for time series displacement monitoring.** Persistent Scatterer InSAR (PS-InSAR) is proven successful in deformation monitoring over urban areas, where stable man-made structures produce efficient reflectors that dominate backscattering [*Ferretti et al.*, 2001; *Hooper et al.*, 2007]. However, man-made structures are absent from most of the earth's surface. The Small Baseline (SBAS) technique overcomes the limitation using "stable" pixels in a series of multilooked interferograms with or without man-made structures [*Berardino et al., 2002*]. However, indiscriminant averaging (boxcar multilooking) and excessive filtering degrade image resolution. As shown in Fig. 4.9 (e), averaging many inhomogeneous pixels leads to contamination of scatterers' properties and therefore lowers SNR of the interferometric phase. Following the concept of [*Ferretti et al.*, 2011] in which both PSs and DSs are combined to improve the performance of time series displacements. The methods proposed in this thesis can be used to further refine the estimation accuracy

of the DSs from two aspects, (i) adaptive mutilooking by simply averaging SHPs to improve the quality of the interferometric phase; and (ii) selecting stable DSs by accurate coherence observations[*Jiang et al.*, 2014c].

# Appendix: test statistics

The expressions of weighted versions of KS and CM tests, i.e., KS1, CM1, KS2, and CM2 used in Section 3.2.2 are given below:

Let $X_1,\ldots,X_m$ and $Y_1,\ldots,Y_n$ be two independent samples from populations with EDFs $F_m$ and $G_n$, and $Z_{(1)},\ldots,Z_{(N')}$ be the order statistics of the combined sample $X_1,\ldots,X_m$, $Y_1,\ldots,Y_n$, $N' = m+n$. Furthermore, let $t(x) = \lambda F_m(x) + (1-\lambda)G_n(x)$ with $\lambda = m/N'$. Modifications KS1 and CM1 can be defined by weight function $(t\cdot(1-t))^{-1}$

$$KS1 = \max_i \frac{\sqrt{M'}\left|F_m(Z_{(i)}) - G_n(Z_{(i)})\right|}{\sqrt{t(Z_{(i)})(1-t(Z_{(i)}))}} \tag{A1}$$

$$CM1 = \frac{mn}{N'^2}\sum_{i=1}^{N'} \frac{\left(F_m(Z_{(i)}) - G_n(Z_{(i)})\right)^2}{t(Z_{(i)})(1-t(Z_{(i)}))} \tag{A2}$$

where $M' = mn/N'$. If $t(x) = 0$ or 1, the denominator of KS1 is equal to $\sqrt{N'-1}/N'$ and that of CM1 is $(N'-1)/N'^2$. Compared with standard test statistics KS and CM, the modifications give more attention to the upper and lower parts of the underlying distribution.

Similarly, the second modifications KS2 and CM2 are defined as

$$KS2 = \max_i \frac{\sqrt{M'}\left|F_m(Z_{(i)}) - G_n(Z_{(i)})\right|}{\sqrt{t(Z_{(i)})(2-t(Z_{(i)}))}} \tag{A3}$$

$$CM2 = \frac{mn}{N'^2}\sum_{i=1}^{N'} \frac{\left(F_m(Z_{(i)}) - G_n(Z_{(i)})\right)^2}{t(Z_{(i)})(2-t(Z_{(i)}))} \tag{A4}$$

where weight function $(t\cdot(1-t))^{-1}$ is considered to emphasize the lower part of the distribution. If $t(x) = 0$, the denominators of KS2 and CM2 are the same as those of KS1 and CM1. Critical values of the statistics KS1, CM1, KS2 and CM2 can

be found in [*Büning and Thadewald*, 2000].

# References

Abdelfattah, R., and J. M., Nicolas (2010), Mixture model for the segmentation of the InSAR coherence map, *International Journal of Applied Earth Observation and Geoinformation*, *12, Supplement 1*(0), S138-S144.

Abdelfattah, R., and J. M. Nicolas (2006), Interferometric SAR coherence magnitude estimation using second kind statistics, *Geoscience and Remote Sensing, IEEE Transactions on*, *44*(7), 1942-1953.

Arciniegas, G. A., W. Bijker, N. Kerle, and V. A. Tolpekin (2006), Coherence-and amplitude-based analysis of seismogenic damage in Bam, Iran, using Envisat ASAR data, *Geoscience and Remote Sensing, IEEE Transactions on*, *45*(6), 1571-1581.

Askne, J., M. Santoro, G. Smith, and J. E. S. Fransson (2003), Multitemporal repeat-pass SAR interferometry of boreal forests, *Geoscience and Remote Sensing, IEEE Transactions on*, *41*(7), 1540-1550.

Askne, J. I. H., P. B. G. Dammert, L. M. H. Ulander, and G. Smith (1997), C-band repeat-pass interferometric SAR observations of the forest, *Geoscience and Remote Sensing, IEEE Transactions on*, *35*(1), 25-35.

Askne, J. I. H., and M. Santoro (2009), Automatic Model-Based Estimation of Boreal Forest Stem Volume From Repeat Pass C-band InSAR Coherence, *Geoscience and Remote Sensing, IEEE Transactions on*, *47*(2), 513-516.

Büning, H. (1994), Robust and adaptive tests for the two-sample location problem, *Operations-Research-Spektrum*, *16*(1), 33-39.

Büning, H. (2001), Kolmogorov-Smirnov-and Cramèr-von Mises type two-sample tests with various weight functions, *Communications in Statistics-Simulation and Computation*, *30*(4), 847-865.

Büning, H. (2002), Robustness and power of modified Lepage,

Kolmogorov-Smirnov and Crame´ r-von Mises two-sample tests, *Journal of Applied Statistics*, *29*(6), 907-924.

Büning, H. (2009), Adaptive tests for the c-sample location problem, *Statistical Inference, Econometric Analysis and Matrix Algebra*, 3-17.

Büning, H., and T. Thadewald (2000), An adaptive two-sample location-scale test of Lepage type for symmetric distributions, *Journal of Statistical Computation and Simulation*, *65*(1-4), 287-310.

Bamler, R., and P. Hartl (1998), Synthetic aperture radar interferometry, *Inverse problems*, *14*, R1.

Baran, I., M. P. Stewart, B. M. Kampes, Z. Perski, and P. Lilly (2003), A modification to the Goldstein radar interferogram filter, *Geoscience and Remote Sensing, IEEE Transactions on*, *41*(9), 2114-2118.

Baumgartner, W., P. Weiß, and H. Schindler (1998), A nonparametric test for the general two-sample problem, *Biometrics*, 1129-1135.

Berardino, P., G. Fornaro, R. Lanari, and E. Sansosti (2002), A new algorithm for surface deformation monitoring based on small baseline differential SAR interferograms, *IEEE transactions on geoscience and remote sensing*, *40*(11), 2375-2383.

Bian, Y., and B. Mercer (2010), Interferometric SAR Extended Coherence Calculation Based on Fractional Lower Order Statistics, *Geoscience and Remote Sensing Letters, IEEE*, *7*(4), 841-845.

Bignami, C., M. Chini, N. Pierdicca, and S. Stramondo (2004), Comparing and combining the capability of detecting earthquake damages in urban areas using SAR and optical data, paper presented at Geoscience and Remote Sensing Symposium, 2004. IGARSS '04. Proceedings. 2004 IEEE International, 20-24 Sept. 2004.

Brys, G., M. Hubert, and A. Struyf (2004), A Robust Measure of Skewness, *Journal*

*of Computational and Graphical Statistics*, *13*(4), 996-1017.

Castel, T., J.-M. Martinez, A. Beaudoin, U. Wegmüller, and T. Strozzi (2000), ERS INSAR Data for Remote Sensing Hilly Forested Areas, *Remote Sensing of Environment*, *73*(1), 73-86.

Charles, L. W., S. Hensley, and P. Rosen (1996), Application of the interferometric correlation coefficient for measurement of surface change, in *Proc. 1996 AGU Fall Meeting,* San Francisco, CA.

Chen, C. W. (2001), Statistical-cost network-flow approaches to two-dimensional phase unwrapping for radar interferometry, Stanford University.

Chen, C. W., and H. A. Zebker (2002), Phase unwrapping for large SAR interferograms: statistical segmentation and generalized network models, *Geoscience and Remote Sensing, IEEE Transactions on*, *40*(8), 1709-1719.

Chen, S.-W., X.-S. Wang, and M. Sato (2012), PolInSAR complex coherence estimation based on covariance matrix similarity test.

Ciuc, M., P. Bolon, E. Trouve, V. Buzuloiu, and J. P. Rudant (2001), Adaptive-neighborhood speckle removal in multitemporal synthetic aperture radar images, *Applied Optics*, *40*(32), 5954-5966.

Dammert, P. B. G. (1997), *Accuracy of INSAR measurements in forested areas*, 2 vol.(376 ; 159 p.) pp., European Space Agency, Noordwijk, PAYS-BAS.

Dammert, P. B. G., J. I. H. Askne, and S. Kuhlmann (1999), Unsupervised segmentation of multitemporal interferometric SAR images, *Geoscience and Remote Sensing, IEEE Transactions on*, *37*(5), 2259-2271.

Davison, A. C., and D. V. Hinkley (1997), *Bootstrap methods and their application*, Cambridge Univ Pr.

De Zan, F., F. Rocca, and Ieee (2005), *Coherent processing of long series of SAR images*, 1987-1990 pp., Ieee, New York.

Deledalle, C. A., L. Denis, and F. Tupin (2009), Iterative Weighted Maximum Likelihood Denoising With Probabilistic Patch-Based Weights, *IEEE Trans. Image Process.*, *18*(12), 2661-2672.

Deledalle, C. A., L. Denis, and F. Tupin (2011), Nl-insar: Nonlocal interferogram estimation, *Geoscience and Remote Sensing, IEEE Transactions on*, *49*(4), 1441-1452.

Ding, X., G. Liu, Z. Li, Z. Li, and Y. Chen (2004), Ground subsidence monitoring in Hong Kong with satellite SAR interferometry, *Photogrammetric engineering and remote sensing*, *70*(10), 1151-1156.

Efron, B. (1981), Nonparametric estimates of standard error: the jackknife, the bootstrap and other methods, *Biometrika*, *68*(3), 589-599.

Efron, B., and R. Tibshirani (1993), *An introduction to the bootstrap*, Chapman & Hall/CRC.

Engdahl, M. E., and J. M. Hyyppa (2003), Land-cover classification using multitemporal ERS-1/2 InSAR data, *Geoscience and Remote Sensing, IEEE Transactions on*, *41*(7), 1620-1628.

Feng, G., X. Ding, Z. Li, M. Jiang, L. Zhang, and M. Omura (2012), Calibration of an InSAR-Derived Coseimic Deformation Map Associated With the 2011 Mw-9.0 Tohoku-Oki Earthquake, *Geoscience and Remote Sensing Letters, IEEE*, *9*(2), 302-306.

Feng, G. C., E. A. Hetland, X. L. Ding, Z. W. Li, and L. Zhang (2010), Coseismic fault slip of the 2008 Mw 7.9 Wenchuan earthquake estimated from InSAR and GPS measurements, *Geophysical Research Letters*, *37*(1), L01302.

Ferretti, A., A. Fumagalli, F. Novali, C. Prati, F. Rocca, and A. Rucci (2011), A New Algorithm for Processing Interferometric Data-Stacks: SqueeSAR, *IEEE transactions on geoscience and remote sensing*, *49*(9), 3460-3470.

Ferretti, A., C. Prati, and F. Rocca (2001), Permanent scatterers in SAR

interferometry, *Geoscience and Remote Sensing, IEEE Transactions on*, *39*(1), 8-20.

Fialko, Y., D. Sandwell, M. Simons, and P. Rosen (2005), Three-dimensional deformation caused by the Bam, Iran, earthquake and the origin of shallow slip deficit, *Nature*, *435*(7040), 295-299.

Fielding, E. J., M. Talebian, P. A. Rosen, H. Nazari, J. A. Jackson, M. Ghorashi, and R. Walker (2005), Surface ruptures and building damage of the 2003 Bam, Iran, earthquake mapped by satellite synthetic aperture radar interferometric correlation, *J. Geophys. Res.-Solid Earth*, *110*(B3).

Gamba, P., F. Dell'Acqua, and G. Trianni (2007), Rapid damage detection in the Bam area using multitemporal SAR and exploiting ancillary data, *Geoscience and Remote Sensing, IEEE Transactions on*, *45*(6), 1582-1589.

Gatelli, F., A. M. Guamieri, F. Parizzi, P. Pasquali, C. Prati, and F. Rocca (1994), The wavenumber shift in SAR interferometry, *Geoscience and Remote Sensing, IEEE Transactions on*, *32*(4), 855-865.

Geudtner, D., R. Winter, and P. W. Vachon (1996), Flood monitoring using ERS-1 SAR interferometry coherence maps, paper presented at Geoscience and Remote Sensing Symposium, 1996. IGARSS '96. 'Remote Sensing for a Sustainable Future.', International, 27-31 May 1996.

Goel, K., and N. Adam (2012), An advanced algorithm for deformation estimation in non-urban areas, *ISPRS Journal of Photogrammetry and Remote Sensing*, *73*, 100-110.

Goering, D. J., H. Chen, L. D. Hinzman, and D. L. Kane (1995), Removal of terrain effects from SAR satellite imagery of Arctic tundra, *Geoscience and Remote Sensing, IEEE Transactions on*, *33*(1), 185-194.

Goldstein, R. M., H. A. Zebker, and C. L. Werner (1988), Satellite radar interferometry – two-dimensional phase unwrapping, *Radio Sci.*, *23*(4),

713-720.

Goodman, N. (1963), Statistical analysis based on a certain multivariate complex Gaussian distribution (an introduction), *The Annals of Mathematical Statistics*, *34*(1), 152-177.

Greco, M. S., and F. Gini (2007), Statistical analysis of high-resolution SAR ground clutter data, *Geoscience and Remote Sensing, IEEE Transactions on*, *45*(3), 566-575.

Guarnieri, A. M., and C. Prati (1997), SAR interferometry: A "quick and dirty" coherence estimator for data browsing, *Geoscience and Remote Sensing, IEEE Transactions on*, *35*(3), 660-669.

Hanssen, R. F. (2001), *Radar interferometry: data interpretation and error analysis*, Kluwer Academic Pub.

Hoen, E. W. (2002), *A correlation-based approach to modeling interferometric radar observations of the Greenland ice sheet*. Ph.D. dissertation, Stanford Uiv. Stanford, CA.

Hoffmann, J. (2007), Mapping damage during the Bam (Iran) earthquake using interferometric coherence, *Int. J. Remote Sens.*, *28*(6), 1199-1216.

Hogg, R. V. (1974), Adaptive robust procedures: A partial review and some suggestions for future applications and theory, *Journal of the American Statistical Association*, *69*(348), 909-923.

Hogg, R. V., D. M. Fisher, and R. H. Randles (1975), A two-sample adaptive distribution-free test, *Journal of the American Statistical Association*, 656-661.

Hogg, R. V., and R. V. Lenth (1984), A review of some adaptive statistical techniques, *Communications in Statistics-Theory and Methods*, *13*(13), 1551-1579.

Hooper, A. (2012), Volcanology: A volcano's sharp intake of breath, *Nature Geoscience*.

Hooper, A., P. Segall, and H. Zebker (2007), Persistent scatterer interferometric synthetic aperture radar for crustal deformation analysis, with application to Volcán Alcedo, Galápagos, *Journal of Geophysical Research: Solid Earth*, *112*(B7), B07407.

Hooper, A., and H. A. Zebker (2007), Phase unwrapping in three dimensions with application to InSAR time series, *J. Opt. Soc. Am. A-Opt. Image Sci. Vis.*, *24*(9), 2737-2747.

Hubert, M., and E. Vandervieren (2008), An adjusted boxplot for skewed distributions, *Computational statistics & data analysis*, *52*(12), 5186-5201.

Jiang, M., Z. Li, X. Ding, J. Zhu, G. Feng and H. Yin (2009), A study on the maximum and minimum detectable deformation gradients resolved by InSAR, *Chinese J. Geophys.-Chinese Ed.*, *52*(7), 1715-1724.

Jiang, M., Z. Li, X. Ding, J. Zhu, and G. Feng (2011), Modeling minimum and maximum detectable deformation gradients of interferometric SAR measurements, *International Journal of Applied Earth Observation and Geoinformation*, *13*(5), 766-777.

Jiang, M., X. Ding, Z. Li, C. Wang, W. Zhu, and L. Ke (2013a), InSAR coherence magnitude estimation based on data stack, *Chinese J. Geophys.-Chinese Ed.*, *56*(3), 799-811.

Jiang, M., X. Ding, and Z. Li (2013b), Hybrid approach for unbiased coherence estimation for multitemporal InSAR, *Geoscience and Remote Sensing, IEEE Transactions on*, DOI: 10.1109/TGRS.2013.2261996.

Jiang, M., X. Ding, Z. Li, X. Tian, C. Wang, and W. Zhu (2013c), The improvement for Baran phase filter derived from unbiased InSAR coherence, *Selected Topics in Applied Earth Observations and Remote Sensing, IEEE Journal of*,

DOI: 10.1109/JSTARS.2013.2296322.

Jiang, M., X. Ding, Z. Li, X. Tian, C. Wang, and W. Zhu (2014a), InSAR coherence estimation for small datasets and its impact on temporal decorrelation extraction, *Geoscience and Remote Sensing, IEEE Transactions on*, DOI: 10.1109/TGRS.2014.2298408.

Jiang, M., X. Ding, R. Hanssen, R. Malhotra, and L. Chang (2014b), Fast statistically homogeneous pixel selection for covariance matrix estimation for multitemporal InSAR, *Geoscience and Remote Sensing, IEEE Transactions on*, DOI: 10.1109/TGRS.2014.2336237.

Jiang M., X. Ding, and R. Hanssen (2014c), Deformation monitoring over low coherence area using multisource DS-InSAR technique, *ESA–MOST Dragon Cooperation 2014 Dragon 3 Mid-Term Results Symposium*, May 26th~29th, 2014, Chengdu, China.

Jiang M., X. Ding, X. Tian, R. Malhotra, and W. Kong (2014d), A hybrid method for optimization of the adaptive Goldstein filter, *ISPRS Journal of Photogrammetry and Remote Sensing*, DOI: 10.1016/j.isprsjprs.2014.09.012.

Joughin, I., W. Abdalati, and M. Fahnestock (2004), Large fluctuations in speed on Greenland's Jakobshavn Isbrae glacier, *Nature*, *432*(7017), 608-610.

Joughin, I. R., D. B. Percival, and D. P. Winebrenner (1993), Maximum likelihood estimation of K distribution parameters for SAR data, *Geoscience and Remote Sensing, IEEE Transactions on*, *31*(5), 989-999.

Jung, H.-S., D.-T. Lee, Z. Lu, and J.-S. Won (2013), Ionospheric correction of SAR interferograms by multiple-aperture interferometry, *Geoscience and Remote Sensing, IEEE Transactions on*, *51*(5), 3191-3199..

Kössler, W. (2010), Max-type rank tests, U-tests, and adaptive tests for the two-sample location problem—An asymptotic power study, *Computational statistics & data analysis*, *54*(9), 2053-2065.

Koskinen, J. T., J. Palliainen, J. M. Hyyppa, M. E. Engdahl, and M. T. Hallikainen (2001), The seasonal behavior of interferometric coherence in boreal forest, *Geoscience and Remote Sensing, IEEE Transactions on*, *39*(4), 820-829.

Kuruoglu, E. E., and J. Zerubia (2004), Modeling SAR images with a generalization of the Rayleigh distribution, *Image Processing, IEEE Transactions on*, *13*(4), 527-533.

Kvam, P. H., and B. Vidakovic (2007), *Nonparametric statistics with applications to science and engineering*, John Wiley & Sons.

López-Martínez, C., and E. Pottier (2007), Coherence estimation in synthetic aperture radar data based on speckle noise modeling, *Applied Optics*, *46*(4), 544-558.

Lee, J.-S., and E. Pottier (2009), *Polarimetric radar imaging: from basics to applications*, CRC PressI Llc.

Lee, J. S., S. R. Cloude, K. P. Papathanassiou, M. R. Grunes, and I. H. Woodhouse (2003), Speckle filtering and coherence estimation of polarimetric SAR interferometry data for forest applications, *Geoscience and Remote Sensing, IEEE Transactions on*, *41*(10), 2254-2263.

Lee, L., K. W. Hoppel, S. A. Mango, and A. R. Miller (1994), Intensity and phase statistics of multilook polarimetric and interferometric SAR imagery, *Geoscience and Remote Sensing, IEEE Transactions on*, *32*(5), 1017-1028.

Li, Z., X. Ding, C. Huang, J. Zhu, and Y. Chen (2008a), Improved filtering parameter determination for the Goldstein radar interferogram filter, *ISPRS Journal of Photogrammetry and Remote Sensing*, *63*(6), 621-634.

Li, Z. W., Xu, G. Feng, J. Hu, C. Wang, X. Ding, and J. Zhu (2012), Correcting atmospheric effects on InSAR with MERIS water vapour data and elevation-dependent interpolation model, *Geophysical Journal International*.

Li, Z. W., X. L. Ding, D. W. Zheng, and C. Huang (2008b), Least Squares-Based Filter

for Remote SensingImage Noise Reduction, *Geoscience and Remote Sensing, IEEE Transactions on*, *46*(7), 2044-2049.

Ma, X., and C. L. Nikias (1995), Parameter estimation and blind channel identification in impulsive signal environments, *Signal Processing, IEEE Transactions on*, *43*(12), 2884-2897.

Mansouri, B., M. Shinozuka, C. Huyck, and B. Houshmand (2005), Earthquake-induced change detection in the 2003 Bam, Iran, earthquake by complex analysis using Envisat ASAR data, *Earthquake Spectra*, *21*(S1), 275-284.

Massonnet, D., and K. L. Feigl (1998), Radar interferometry and its application to changes in the Earth's surface, *Reviews of geophysics*, *36*(4), 441-500.

Miller, R. G. (1974), The jackknife-a review, *Biometrika*, *61*(1), 1-15.

Mora, O., J. J. Mallorqui, and A. Broquetas (2003), Linear and nonlinear terrain deformation maps from a reduced set of interferometric SAR images, *IEEE transactions on geoscience and remote sensing*, *41*(10), 2243-2253.

Munk, J., K. C. Jezek, R. R. Forster, and S. P. Gogineni (2003), An accumulation map for the Greenland dry-snow facies derived from spaceborne radar, *Journal of Geophysical Research-Atmospheres*, *108*(D9).

Neuhäuser, M. (2000), An exact two-sample test based on the Baumgartner-Weiß-Schindler statistic and a modification of Lepage's test, *Communications in Statistics-Theory and Methods*, *29*(1), 67-78.

Neuhäuser, M., Büning, and L. Hothorn (2004), Maximum test versus adaptive tests for the two-sample location problem, *Journal of Applied Statistics*, *31*(2), 215-227.

Nikias, C. L., and M. Shao (1995), *Signal processing with alpha-stable distributions and applications*, Wiley-Interscience.

O'Gorman, T. W. (2004), *Applied adaptive statistical methods: tests of significance and confidence intervals*, Society for Industrial Mathematics.

Oliver, C., and S. Quegan (2004), *Understanding synthetic aperture radar images*, SciTech Publishing.

Oveisgharan, S., and H. A. Zebker (2007), Estimating snow accumulation from InSAR correlation observations, *Geoscience and Remote Sensing, IEEE Transactions on*, *45*(1), 10-20.

Papoulis, A. (1991), *Probability, random variables, and stochastic processes 3rd Edition*, McGraw-Hill Book Company, New York.

Parizzi, A., and R. Brcic (2011), Adaptive InSAR Stack Multilooking Exploiting Amplitude Statistics: A Comparison Between Different Techniques and Practical Results, *Geoscience and Remote Sensing Letters, IEEE*(99), 441-445.

Pepe, A., P. Berardino, M. Bonano, L. D. Euillades, R. Lanari, and E. Sansosti (2011), SBAS-based satellite orbit correction for the generation of DInSAR time-series: Application to RADARSAT-1 data, *Geoscience and Remote Sensing, IEEE Transactions on*, *49*(12), 5150-5165.

Perissin, D., and T. Wang (2012), Repeat-Pass SAR Interferometry With Partially Coherent Targets, *IEEE transactions on geoscience and remote sensing*, *50*(1), 271-280.

Rignot, E. J. M., and J. J. Van Zyl (1993), Change detection techniques for ERS-1 SAR data, *Geoscience and Remote Sensing, IEEE Transactions on*, *31*(4), 896-906.

Roberts, W. J., and S. Furui (2000), Maximum likelihood estimation of K-distribution parameters via the expectation-maximization algorithm, *Signal Processing, IEEE Transactions on*, *48*(12), 3303-3306.

Rosen, P. A., S. Hensley, I. R. Joughin, F. K. Li, S. N. Madsen, E. Rodriguez, and R. M. Goldstein (2000), Synthetic aperture radar interferometry, *Proceedings of*

*the IEEE*, *88*(3), 333-382.

Rott, H., and W. Rack (1995), *Characterization of antarctic firn by means of ERS-1 scatterometer measurements*, 2041-2043 pp., Ieee, New York.

Santoro, M., J. Askne, G. Smith, and J. E. S. Fransson (2002), Stem volume retrieval in boreal forests from ERS-1/2 interferometry, *Remote Sensing of Environment*, *81*(1), 19-35.

Santoro, M., J. I. H. Askne, U. Wegmiiller, and C. L. Werner (2007a), Observations, modeling, and applications of ERS-ENVISAT coherence over land surfaces, *Geoscience and Remote Sensing, IEEE Transactions on*, *45*(8), 2600-2611.

Santoro, M., A. Shvidenko, I. McCallum, J. Askne, and C. Schmullius (2007b), Properties of ERS-1/2 coherence in the Siberian boreal forest and implications for stem volume retrieval, *Remote Sensing of Environment*, *106*(2), 154-172.

Seymour, M., and I. Cumming (1994), Maximum likelihood estimation for SAR interferometry, IEEE.

Spagnolini, U. (1995), 2-D phase unwrapping and instantaneous frequency estimation, *Geoscience and Remote Sensing, IEEE Transactions on*, *33*(3), 579-589.

Strozzi, T., P. B. G. Dammert, U. Wegmuller, J. M. Martinez, J. I. H. Askne, A. Beaudoin, and M. T. Hallikainen (2000), Landuse mapping with ERS SAR interferometry, *Geoscience and Remote Sensing, IEEE Transactions on*, *38*(2), 766-775.

Tanase, M. A., M. Santoro, U. Wegmüller, J. de la Riva, and F. Pérez-Cabello (2010), Properties of X-, C- and L-band repeat-pass interferometric SAR coherence in Mediterranean pine forests affected by fires, *Remote Sensing of Environment*, *114*(10), 2182-2194.

Tian, X., and M. S. Liao (2013), The analysis of conditions for InSAR in the field of

deformation monitoring, *Chinese J. Geophys.-Chinese Ed.*, *56*(3), 812-823.

Tou, J., T. and R. C. Gonzalez (1974), *Pattern Recognition Principles*, Addison-Wesley Publishing Company, Reading, Massachusetts.

Tough, R., D. Blacknell, and S. Quegan (1995), A statistical description of polarimetric and interferometric synthetic aperture radar data, *Proceedings of the Royal Society of London. Series A: Mathematical and Physical Sciences*, *449*(1937), 567-589.

Touzi, R., A. Lopes, J. Bruniquel, and P. W. Vachon (1999), Coherence estimation for SAR imagery, *Geoscience and Remote Sensing, IEEE Transactions on*, *37*(1), 135-149.

Trouvé, E., M. Caramma, and H. Maître (1996), Fringe detection in noisy complex interferograms, *Applied Optics*, *35*(20), 3799-3806.

Trouve, E., J. M. Nicolas, and H. Maitre (1998), Improving phase unwrapping techniques by the use of local frequency estimates, *IEEE transactions on geoscience and remote sensing*, *36*(6), 1963-1972.

Vasile, G., E. Trouvé, M. Ciuc, and V. Buzuloiu (2004), General adaptive-neighborhood technique for improving synthetic aperture radar interferometric coherence estimation, *JOSA A*, *21*(8), 1455-1464.

Vasile, G., E. Trouvé, J. S. Lee, and V. Buzuloiu (2006), Intensity-driven adaptive-neighborhood technique for polarimetric and interferometric SAR parameters estimation, *Geoscience and Remote Sensing, IEEE Transactions on*, *44*(6), 1609-1621.

Vasile, G., E. Trouvé, I. Petillot, P. Bolon, J. M. Nicolas, M. Gay, J. Chanussot, T. Landes, P. Grussenmeyer, and V. Buzuloiu (2008), High-resolution SAR interferometry: Estimation of local frequencies in the context of Alpine glaciers, *Geoscience and Remote Sensing, IEEE Transactions on*, *46*(4), 1079-1090.

Wang, T., M. Liao, and D. Perissin (2010), InSAR coherence-decomposition analysis, *Geoscience and Remote Sensing Letters, IEEE*, *7*(1), 156-160.

Wang, Y. Y., X. X. Zhu, and R. Bamler (2012), Retrieval of phase history parameters from distributed scatterers in urban areas using very high resolution SAR data, *ISPRS Journal of Photogrammetry and Remote Sensing*, *73*, 89-99.

Weber Hoen, E., and H. A. Zebker (2000), Penetration depths inferred from interferometric volume decorrelation observed over the Greenland ice sheet, *Geoscience and Remote Sensing, IEEE Transactions on*, *38*(6), 2571-2583.

Wegmuller, U., and C. Werner (1997), Retrieval of vegetation parameters with SAR interferometry, *Geoscience and Remote Sensing, IEEE Transactions on*, *35*(1), 18-24.

Wegmuller, U., and C. L. Werner (1995), SAR interferometric signatures of forest, *Geoscience and Remote Sensing, IEEE Transactions on*, *33*(5), 1153-1161.

Wei, M., and D. T. Sandwell (2010), Decorrelation of L-band and C-band interferometry over vegetated areas in California, *Geoscience and Remote Sensing, IEEE Transactions on*, *48*(7), 2942-2952.

Weier, J., and D. Herring (1999), Measuring Vegetation (NDVI & EVI), Earth Observatory, NASA, USA.

Wiesmann, A., U. Wegmuller, M. Honikel, T. Strozzi, and C. L. Werner (2001), Potential and methodology of satellite based SAR for hazard mapping, paper presented at Geoscience and Remote Sensing Symposium, 2001. IGARSS '01. IEEE 2001 International, 2001.

Wilcox, R. R. (2012), *Introduction to robust estimation and hypothesis testing*, Academic Press.

Yonezawa, C., and S. Takeuchi (2001), Decorrelation of SAR data by urban damages caused by the 1995 Hyogoken-nanbu earthquake, *Int. J. Remote Sens.*, *22*(8), 1585-1600.

Yun, S. H., H. Zebker, P. Segall, Hooper, and M. Poland (2007), Interferogram formation in the presence of complex and large deformation, *Geophysical Research Letters*, *34*(12).

Zebker, H. A., and K. Chen (2005), Accurate estimation of correlation in InSAR observations, *Geoscience and Remote Sensing Letters, IEEE*, *2*(2), 124-127.

Zebker, H. A., and J. Villasenor (1992), Decorrelation in interferometric radar echoes, *Geoscience and Remote Sensing, IEEE Transactions on*, *30*(5), 950-959.

Zhang, L., Z. Lu, X. Ding, H.-s. Jung, G. Feng, and C.-W. Lee (2012), Mapping ground surface deformation using temporarily coherent point SAR interferometry: Application to Los Angeles Basin, *Remote Sensing of Environment*, *117*, 429-439.

Zoubir, A. M., and B. Boashash (1998), The bootstrap and its application in signal processing, *Signal Processing Magazine, IEEE*, *15*(1), 56-76.